

Electronic Supplementary Information

Impact of *N*-heteroaromatic *N*-termini in Cu(II) ATCUN metallopeptides on their biorelevant redox activity

Table of contents

S0 Overview of synthesized peptides and Cu(II) complexes	1
S1 Materials and methods.....	3
S2 Synthesis of <i>N</i> -heteroaromatic compounds.....	5
S3 Peptide synthesis.....	15
S4 Cu(II) complex synthesis and characterization	30
S6 ROS detection by fluorescence spectroscopy	45
S7 DNA interaction studies	48
S8 Cyclic voltammetry	53
S9 Computational details and data	72
S10 References	75

S0 Overview of synthesized peptides and Cu(II) complexes

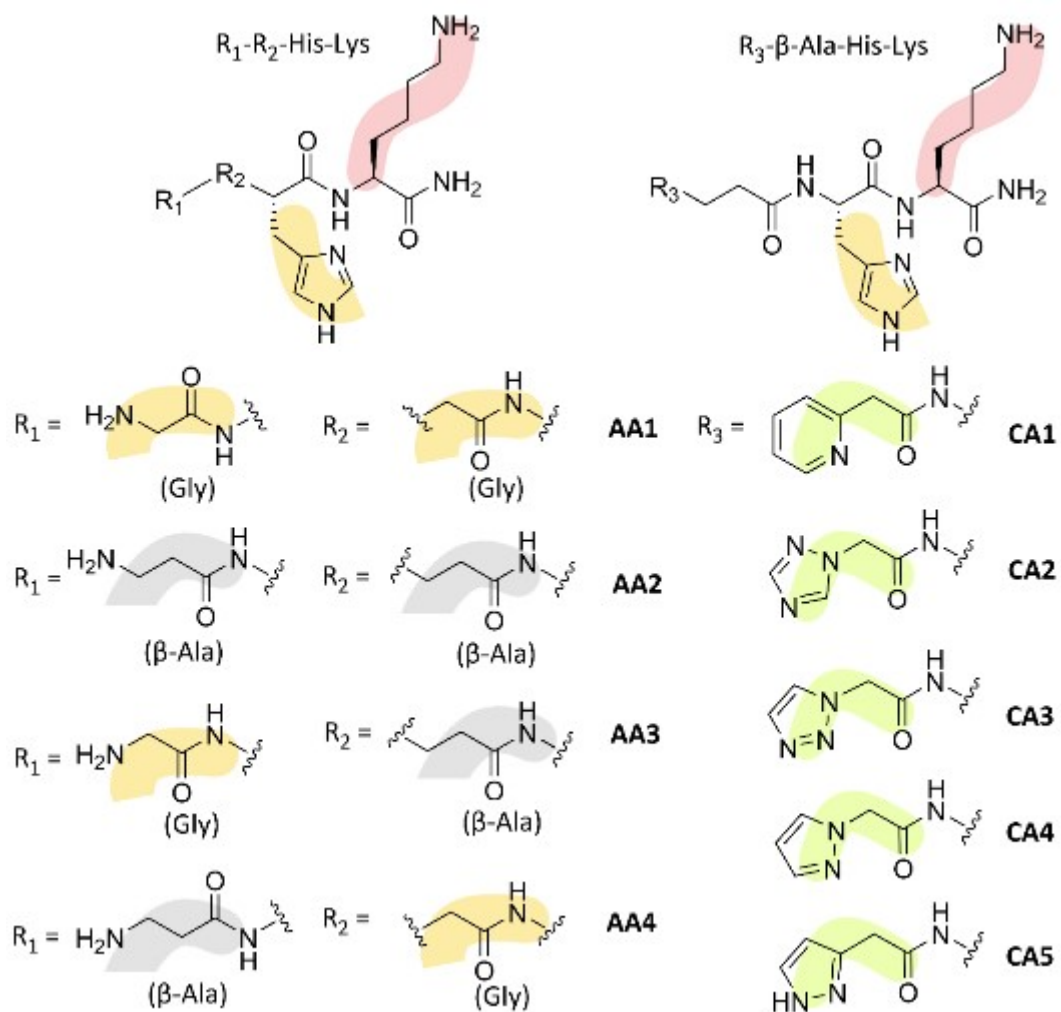


Chart S0.1. Tetrapeptides **AA1–AA4** and **CA1–CA5** incorporating Gly, β -Ala, His, Lys and *N*-heteroaromatics.

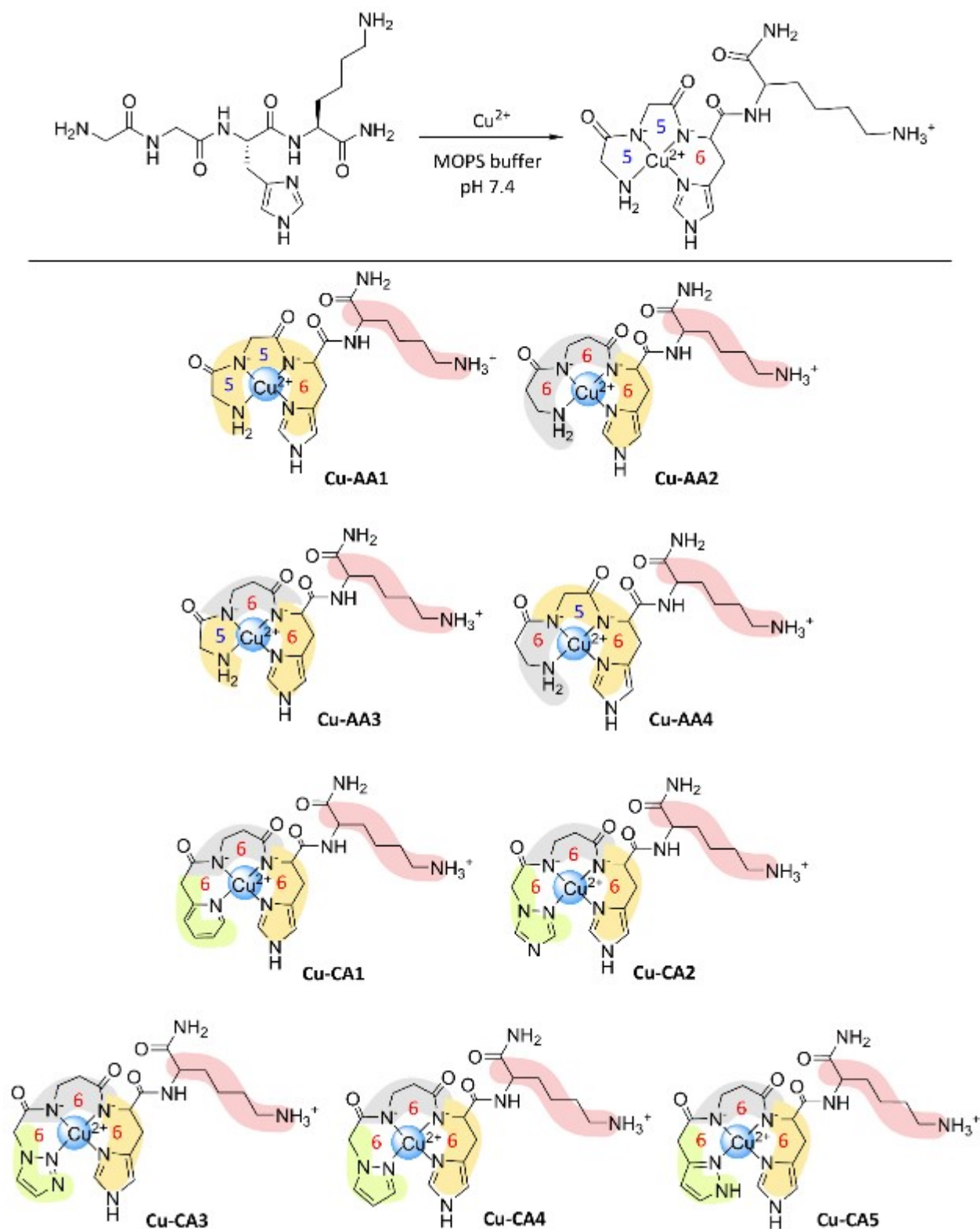


Chart S0.2. Formation of the corresponding Cu(II) complexes **Cu-AA1–Cu-AA4** and **Cu-CA1–Cu-CA5** in MOPS buffer at pH 7.4.

S1 Materials and methods

Materials

Fmoc-protected amino acids glycine, β -alanine, histidine(Trt) and lysine(Boc) were purchased from *Carbolution Chemicals*. All amino acids used were of the L-configuration. Unless stated, all other reagents and solvents were obtained from *Alfa Aesar*, *Carl Roth*, *Fisher Scientific*, *Fluorochem*, *J&K*, *Merck*, *Novabiochem*, *Sigma-Aldrich*, and *VWR* and were used without further purification. Copper(II) chloride was used as the dihydrate. Ascorbate and pyruvate in the incubation solutions were prepared by diluting L-ascorbic acid and pyruvic acid stock solutions. Bioanalytical analyses were conducted using Milli-Q[®] water (18 M Ω · cm).

General methods

¹H (400 MHz) and ¹³C NMR (100 MHz) spectra of heteroaromatic compounds were recorded in D₂O, DMSO-*d*₆, and TFA on a *Jeol ECX 400 FT-NMR* instrument. TMS was used as an external standard.

ESI-MS spectra of *N*-heteroaromatics, tetrapeptides and Cu(II) complexes were obtained on an *Agilent 6210 ESI-ToF*, *Agilent Technologies* using MeOH as the dilution solvent.

Purification of peptides **AA1–AA4** and **CA1–CA5** was carried out by RP-HPLC on a *VWR Hitachi Chromaster 5000*.

UV/VIS spectra were obtained on a *Varian Cary 100 Bio UV/VIS spectrophotometer*.

Fluorescence analyses were conducted on an *Agilent Cary Eclipse spectrophotometer*.

Circular dichroism spectroscopy was performed on a *Jasco J-810* and an *Applied Photophysics Chirascan spectrometer*.

Cyclic voltammetry measurements were carried out on a *Metrohm DropSens μ Stat 400 Bipotentiostat/Galvanostat* and *Metrohm DropSens Screen-Printed Carbon electrode* (ref. 110). The electrochemical cell consists of carbon as working and auxiliary electrodes and silver as reference electrode on a ceramic substrate. For calculating the redox potentials vs. Ag/AgCl (manuscript text and Figure 3 therein, as well as S8 herein), a shift of +0.131 V was considered as suggested by the manufacturer.

For EPR measurements, the complexes with an initial concentration of 1 mM dissolved in 10 mM MOPS buffer were diluted to a final concentration of 0.5 mM in a total sample volume of 200 μ L. All samples contain 20% glycerol (86-88% from *Thermo Fisher Scientific*) of the total volume, as cryoprotectant. Empirically, this should not impose any structural changes, as we know that water structure seems unperturbed by small (20-30 vol%) volume fractions of glycerol.¹ EPR tubes of an

outer diameter of 3 mm were filled with the samples. Then they were vitrified by immersion of the tube in precooled methyl butane and subsequent immersion in liquid nitrogen and were stored at -80 °C for EPR measurements.

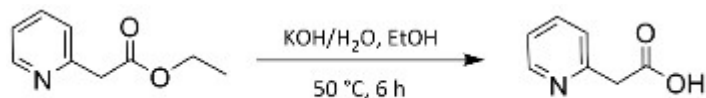
X-Band (9.43 GHz) CW-EPR measurements were performed on a *Magnettech MiniScope MS400* benchtop spectrometer (*Magnettech*, now *Bruker BioSpin*). Spectra were recorded with a microwave power of 3 mW, 100 kHz modulation frequency, modulation amplitude of 0.3 mT and 4096 points. The spectra were measured at liquid nitrogen temperature (77 K) using a finger dewar.

Q-band (33.9 GHz) CW-EPR measurements were conducted on a *Bruker BioSpin EMX-plusQ* spectrometer, using a standard ER5106QT resonator. A closed cycle cryostat (*Sumitomo cryo compressor-F70*) was used for cooling down to 50 K together with an *Oxford Instruments MercuryITC* to control the temperature. Microwave power and modulation frequency were set to 0.1 mW and 100 kHz for all measurements. The modulation amplitude was 0.5 mT.

The *EasySpin software package* (version 5.2.33) was used for spectral simulations of EPR spectra.² The natural abundance of nuclei was considered in all simulations, details to these simulations are given in ref. 3.

S2 Synthesis of *N*-heteroaromatic compounds

Synthesis of 2-pyridylacetic acid



Preparation was performed following the slightly modified procedure described in the literature.⁴ To a solution of ethyl 2-(pyridin-2-yl)acetate (1.0 mL, 6.57 mmol) in ethanol (12 mL), potassium hydroxide (0.398 g, 7.09 mmol) dissolved in water (2.4 mL) was added, and the mixture was then stirred for 6 h at 50 °C. Afterwards, the reaction mixture was stirred overnight at room temperature. The remaining solution was concentrated to one half of the initial volume and the aqueous phase was washed with diethyl ether (3 x 10 mL). The aqueous phase was neutralized with concentrated HCl and the solvent was evaporated under reduced pressure. The solid was then treated with hot isopropanol and the solution was stirred for some minutes. After evaporation of the solvent, the desired compound was isolated as a white solid (0.604 g, 4.41 mmol, 65%). ¹H NMR (DMSO-*d*₆, 400 MHz) δ 8.33 (d, *J* = 4.7 Hz, 1H), 7.58 (t, *J* = 7.6 Hz, 1H), 7.26 (d, *J* = 7.8 Hz, 1H), 7.08 (t, *J* = 6.2 Hz, 1H), 3.40 (s, 2H). ¹³C NMR (DMSO-*d*₆, 100 MHz) δ 173.21, 157.95, 148.32, 136.62, 124.09, 121.10, 48.30. ESI-MS - (*m/z*): 92.0491 (calc. 92.0506) [M – CO₂H]⁻, 136.0393 (calc. 136.0404) [M – H]⁻.

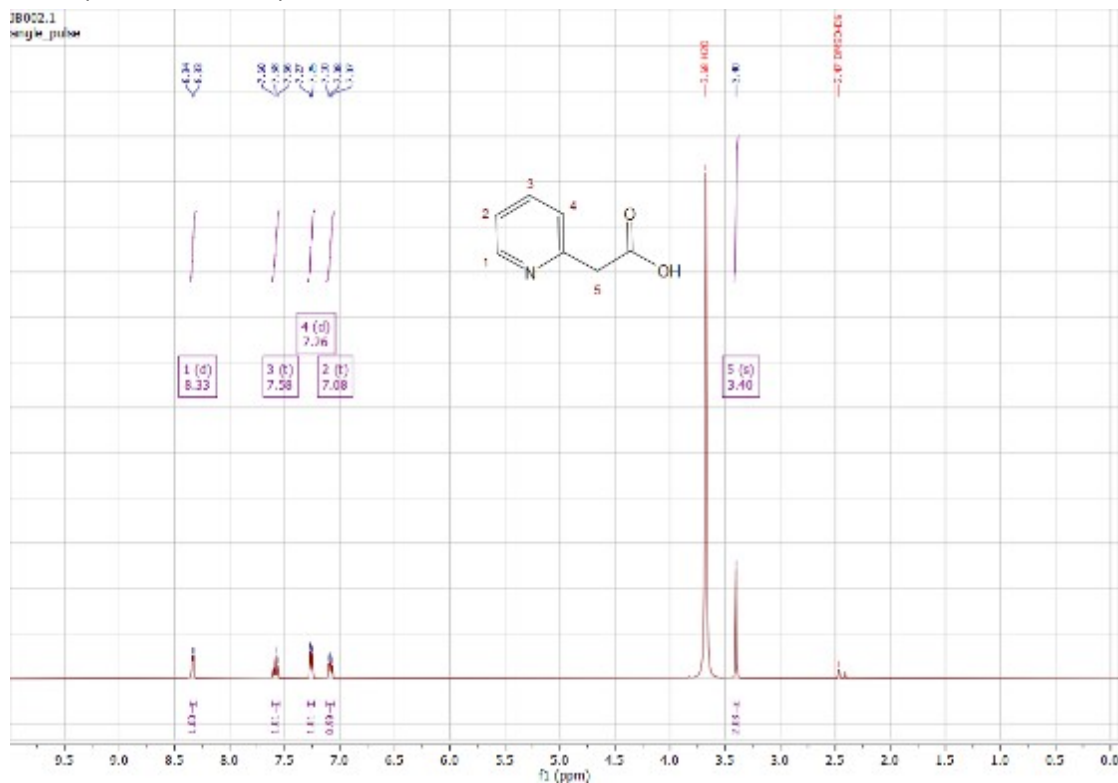


Figure S2.1. ¹H NMR spectrum of 2-pyridylacetic acid in DMSO-*d*₆.

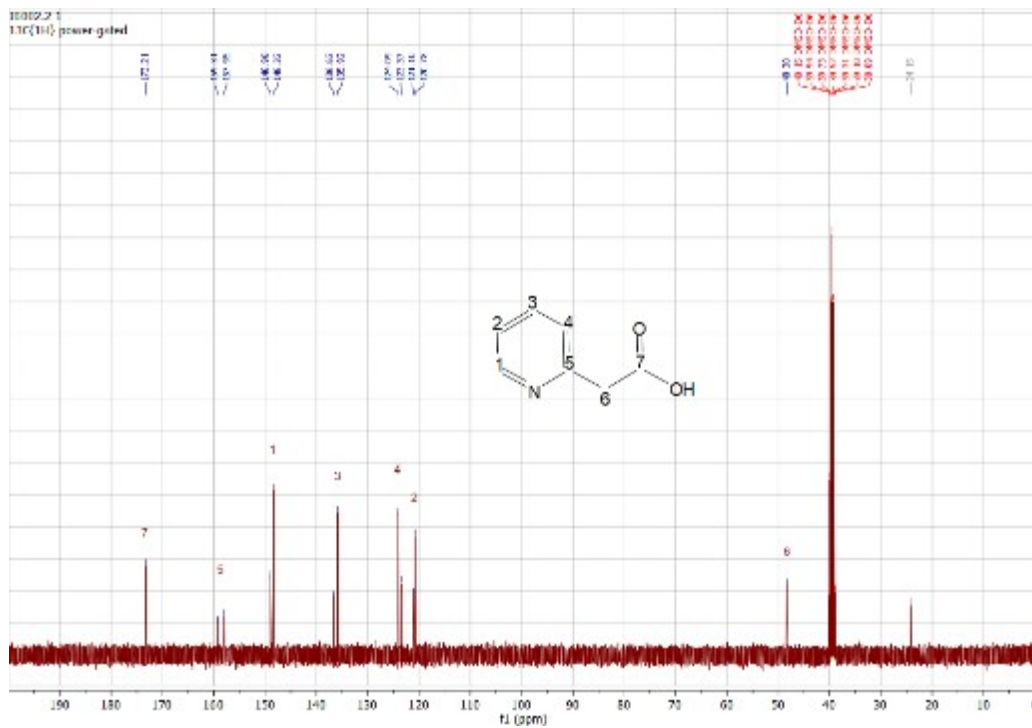


Figure S2.2. ^{13}C NMR spectrum of 2-pyridylacetic acid in $\text{DMSO}-d_6$.

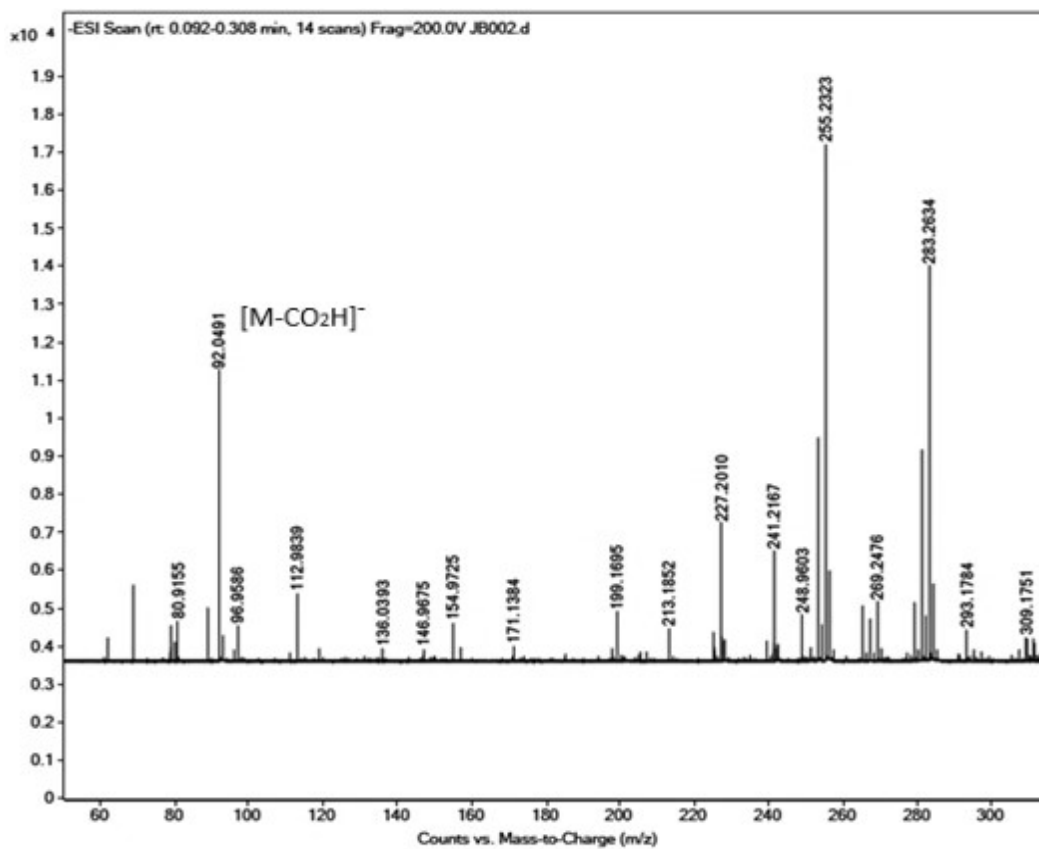
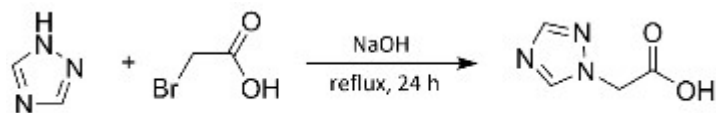


Figure S2.3. Mass spectrum of 2-pyridylacetic acid. Dilution with MeOH.

Synthesis of 2-(1H-1,2,4-triazol-1-yl)acetic acid



The reaction was carried out according to a literature known procedure with slight modifications.⁵ 1H-1,2,4-Triazole (1.090 g, 15.78 mmol) was added to an aqueous solution (18 mL) of sodium hydroxide (1.386 g, 34.66 mmol). Subsequently, bromoacetic acid (2.408 g, 17.33 mmol) was added to this mixture in portions while stirring constantly. The mixture was then heated to reflux for 24 h. During this time, the basic pH was kept constant. After cooling to room temperature, the solution was acidified to pH 1 with 2 M HCl when precipitation of the desired product was observed. The solvent was then evaporated and the white solid was dried under reduced pressure. Hot isopropanol was added to separate the insoluble inorganic salt and the desired compound in solution. The latter was evaporated, and the colorless solid was dried under vacuum. The desired compound was obtained in 39% yield (0.779 g, 6.13 mmol). ¹H NMR (D₂O, 400 MHz) δ 9.44 (s, 1H), 8.63 (s, 1H), 5.31 (s, 2H). ¹³C NMR (D₂O, 100 MHz) δ 169.40, 145.43, 143.41, 51.78. ESI-MS - (m/z): 126.0297 (calc. 126.0309) [M - H]⁻, 275.0513 (calc. 275.0510) [2M + Na - 2H]⁻.



Figure S2.4. ¹H NMR spectrum of 2-(1H-1,2,4-triazol-1-yl)acetic acid in D₂O.

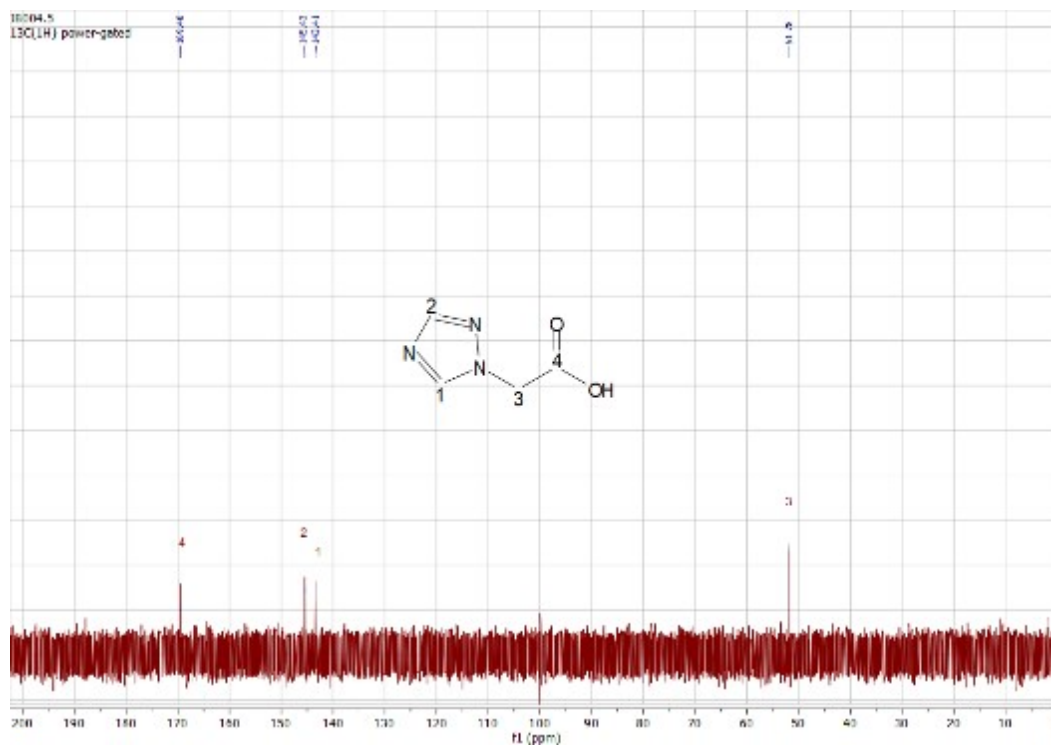


Figure S2.5. ¹³C NMR spectrum of 2-(1H-1,2,4-triazol-1-yl)acetic acid in D₂O.

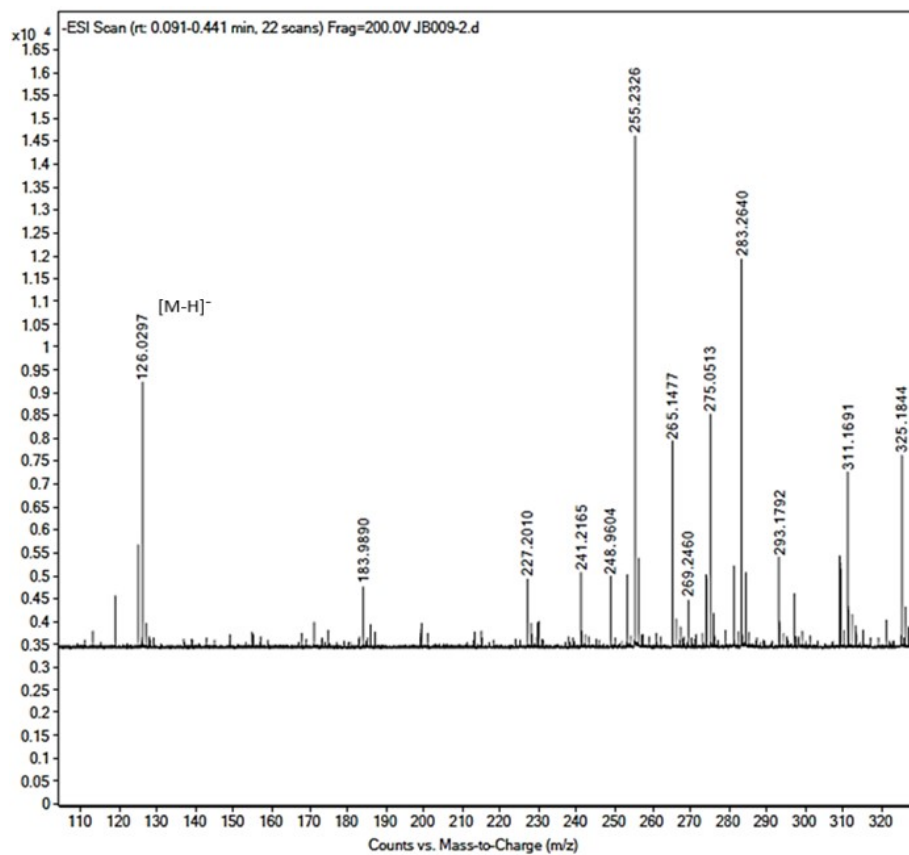
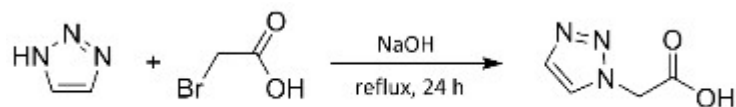


Figure S2.6. Mass spectrum of 2-(1H-1,2,4-triazol-1-yl)acetic acid. Dilution with MeOH.

Synthesis of 2-(1*H*-1,2,3-triazol-1-yl)acetic acid



The reaction was performed according to the procedure described in the literature, increasing the reaction time.⁵ 1*H*-1,2,3-Triazole (0.423 mL, 7.30 mmol) was added to an aqueous solution (8 mL) of sodium hydroxide (0.642 g, 16.05 mmol). Subsequently, bromoacetic acid (1.119 g, 8.05 mmol) was added to this mixture in portions while stirring constantly. The mixture was then heated to reflux for 24 h. During this time, the basic pH was kept constant. After cooling to room temperature, the solution was acidified to pH 3 by adding 2 M HCl dropwise, and the precipitation was immediately observed. The colorless solid was filtered off, dried under vacuum and obtained in 43% yield (0.397 g, 3.13 mmol). ¹H NMR (D₂O, 400 MHz) δ 8.07 (s, 1H), 7.89 (s, 1H), 5.36 (s, 2H). ¹³C NMR (D₂O, 100 MHz) δ 170.21, 133.04, 127.59, 51.10. ESI-MS - (m/z): 126.0323 (calc. 126.0309) [M - H]⁻, 275.0538 (calc. 275.0510) [2M + Na - 2H]⁻.



Figure S2.7. ¹H NMR spectrum of 2-(1*H*-1,2,3-triazol-1-yl)acetic acid in D₂O.

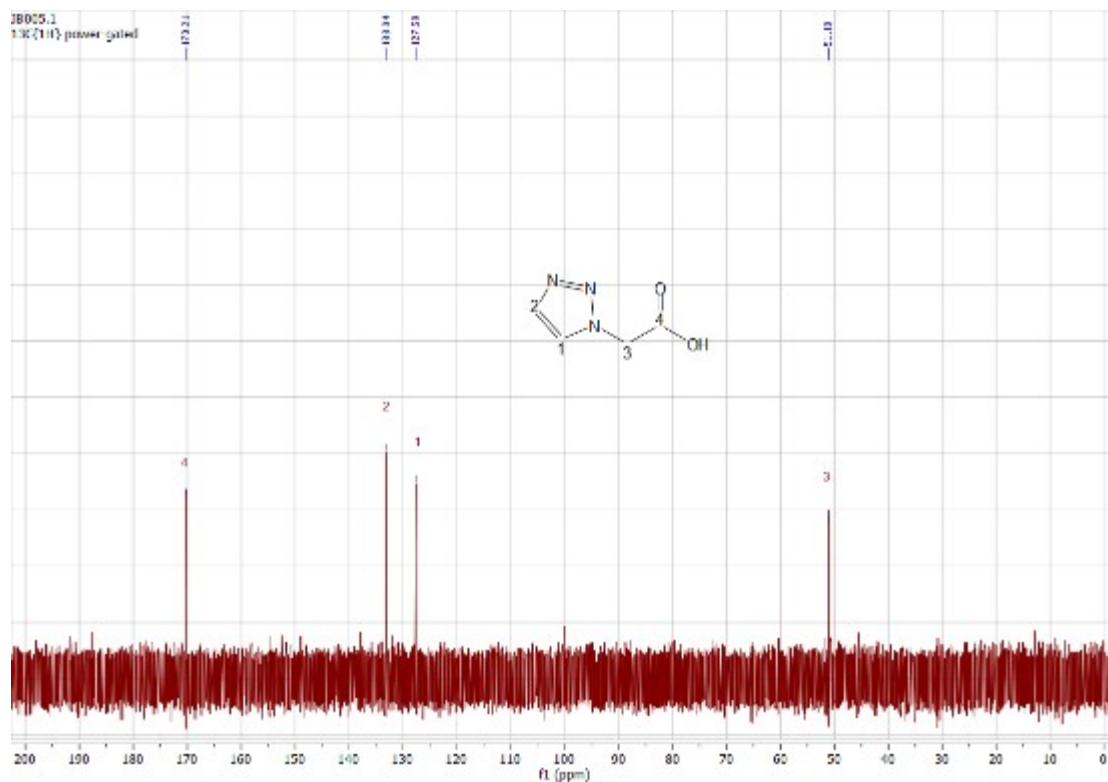


Figure S2.8. ^{13}C NMR spectrum of 2-(1*H*-1,2,3-triazol-1-yl)acetic acid in D_2O .

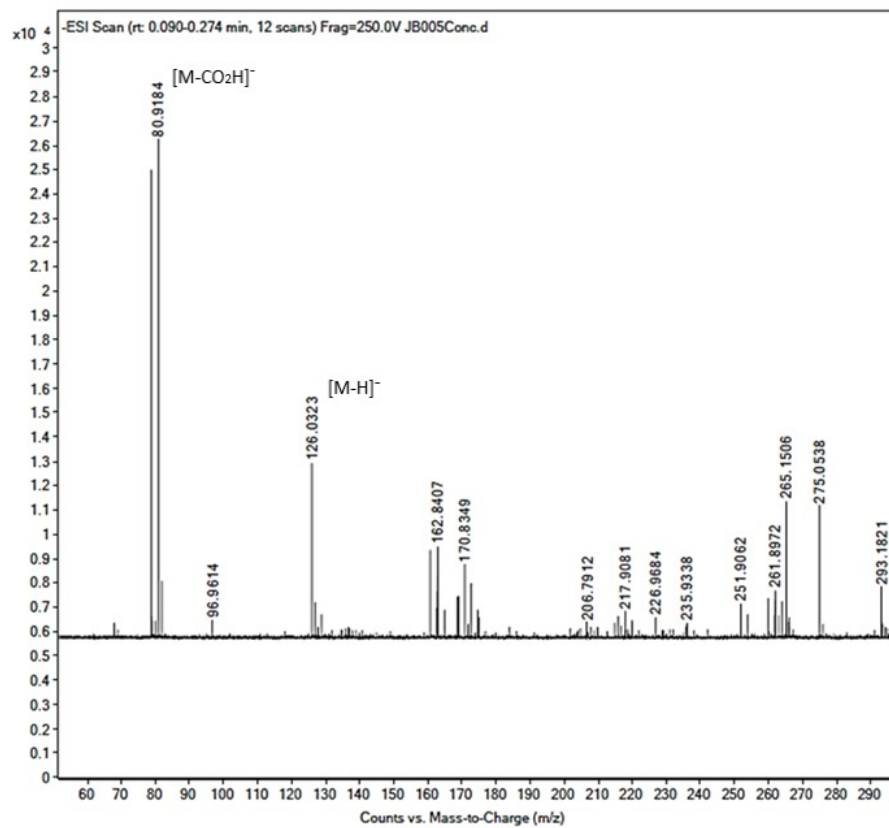
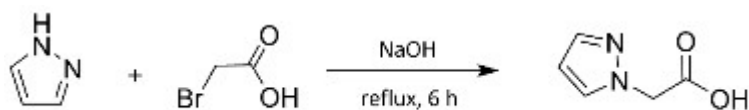


Figure S2.9. Mass spectrum of 2-(1*H*-1,2,3-triazol-1-yl)acetic acid. Dilution with MeOH.

Synthesis of 2-(1*H*-pyrazol-1-yl)acetic acid



The synthesis of 2-(1*H*-pyrazol-1-yl)acetic acid was carried out as described in the literature, increasing the reaction time.⁵ To an aqueous solution (16 mL) of sodium hydroxide (1.322 g, 33.06 mmol), 1*H*-pyrazole (1.022 g, 15.02 mmol) was added. Subsequently, bromoacetic acid (2.298 g, 16.54 mmol) was added to this mixture in portions while stirring constantly. The mixture was then heated to reflux for 6 h. During this time, the basic pH was kept constant. After cooling to room temperature, the solution was acidified to pH 3 by adding 2 M HCl dropwise, and the precipitation was immediately observed. The colorless solid was filtered off, dried under vacuum, and the desired compound was obtained in 42% yield (0.787 g, 6.24 mmol). ¹H NMR (D₂O, 400 MHz) δ 7.75 (s, 1H), 7.72 (s, 1H), 6.46 (s, 1H), 5.07 (s, 2H). ¹³C NMR (D₂O, 100 MHz) δ 171.66, 139.38, 133.49, 106.87, 52.08. ESI-MS - (m/z): 125.0342 (calc. 125.0357) [M - H]⁻, 273.0603 (calc. 273.0605) [2M + Na - 2H]⁻.



Figure S2.10. ¹H NMR spectrum of 2-(1*H*-pyrazol-1-yl)acetic acid in D₂O.

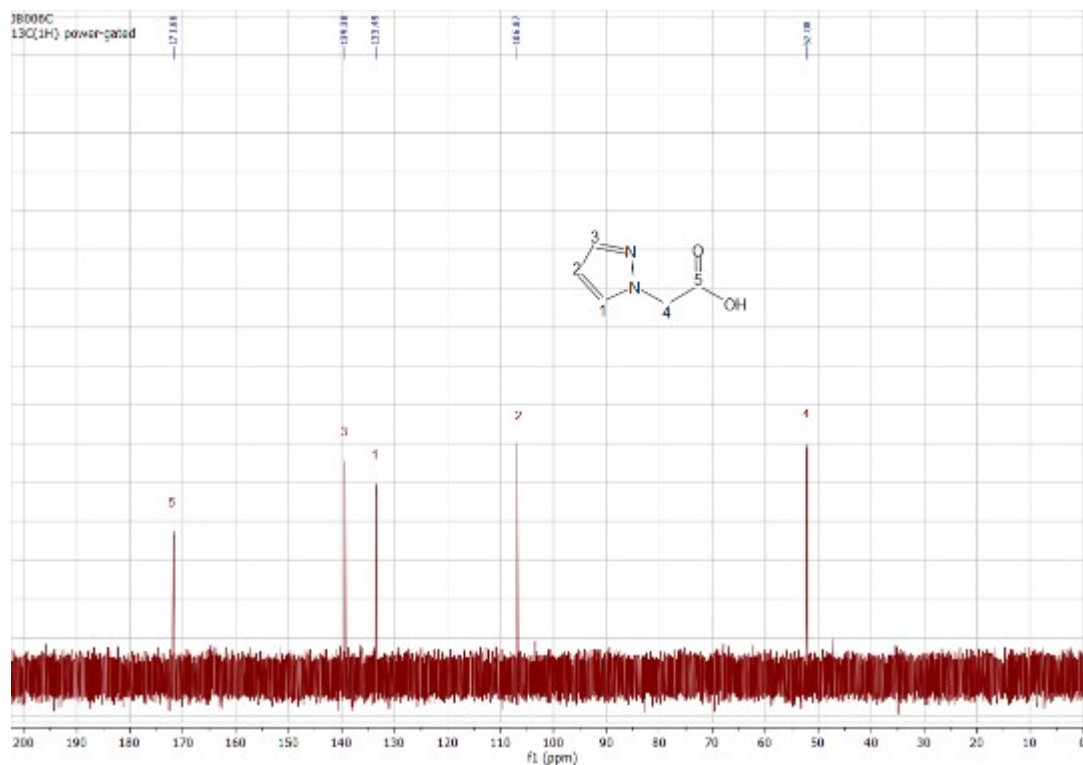


Figure S2.11. ^{13}C NMR spectrum of 2-(1H-pyrazol-1-yl)acetic acid in D_2O .

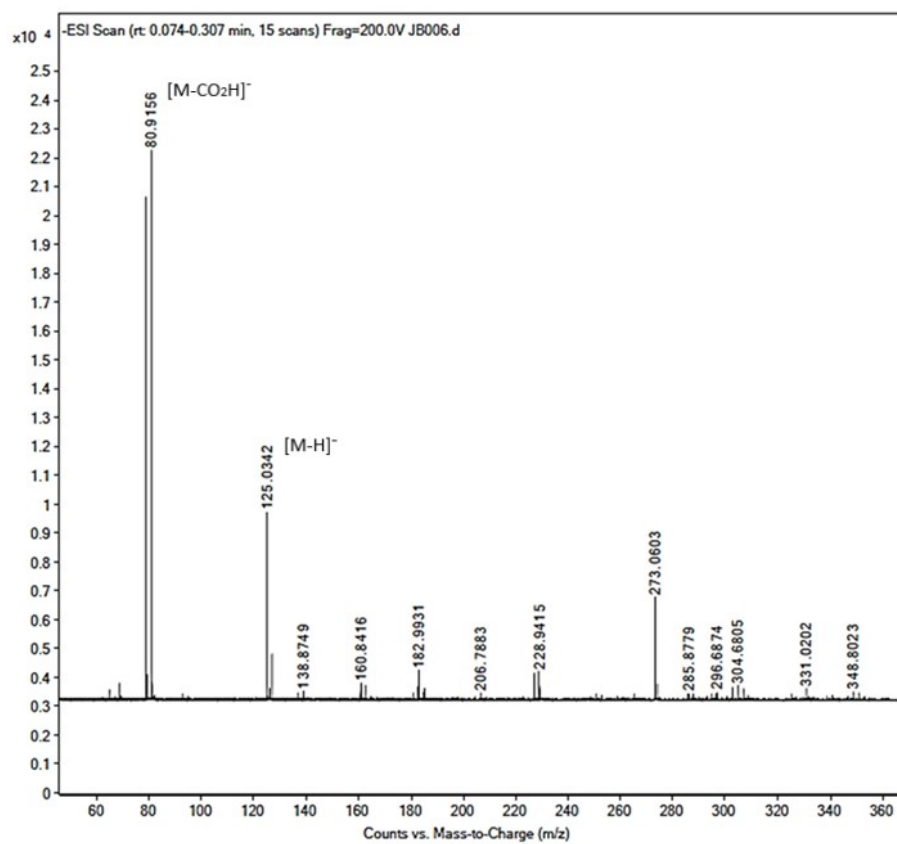
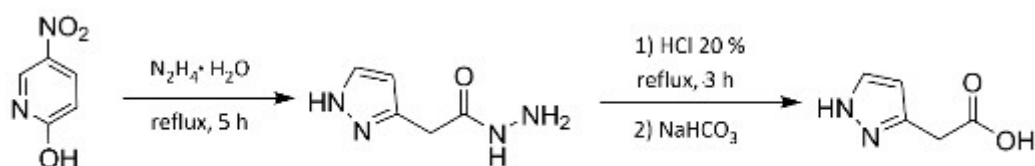


Figure S2.12. Mass spectrum of 2-(1H-pyrazol-1-yl)acetic acid. Dilution with MeOH.

Synthesis of 2-(1*H*-pyrazol-3-yl)acetic acid



2-(1*H*-Pyrazol-3-yl)acetic acid was prepared according to previously described methods with slight modifications.⁶ 2-Hydroxy-5-nitropyridine (3.184 g, 22.73 mmol) was dissolved in an aqueous solution of hydrazine (22 mL) and heated to reflux for 5 h. After completion of the reaction, the solvent was evaporated under reduced pressure and the brown residue was recrystallized in ethanol. 2-(1*H*-Pyrazol-3-yl)acetohydrazide was filtered off and dried under vacuum (1.964 g, 14.01 mmol, 62%). The latter was then dissolved (1.548 g, 11.05 mmol) in 20% HCl (50 mL) and the resulting mixture was heated to reflux for 3 h. After cooling, the solution was neutralized to pH 8. The solvent was then evaporated under reduced pressure and the brown solid was recrystallized with isopropanol. In a further step, the residue was treated with hot isopropanol and the solution was left overnight at -4 °C from which a yellow precipitate was then observed. After evaporation of the solvent, the desired compound was isolated as an orange solid in 58% yield (0.805 g, 6.38 mmol). ¹H NMR (CF_3COOH , 400 MHz) δ 8.03 (s, 1H), 6.74 (s, 1H), 4.11 (s, 2H). ¹³C NMR (CF_3COOH , 100 MHz,) δ 171.54, 144.38, 138.37, 112.59, 33.08. ESI-MS - (*m/z*): 81.0458 (calc. 81.0458) [*M* - CO_2H]⁻, 125.0335 (calc. 125.0357) [*M* - H]⁻, 273.0570 (calc. 273.0605) [*2M* + Na - 2H]⁻.

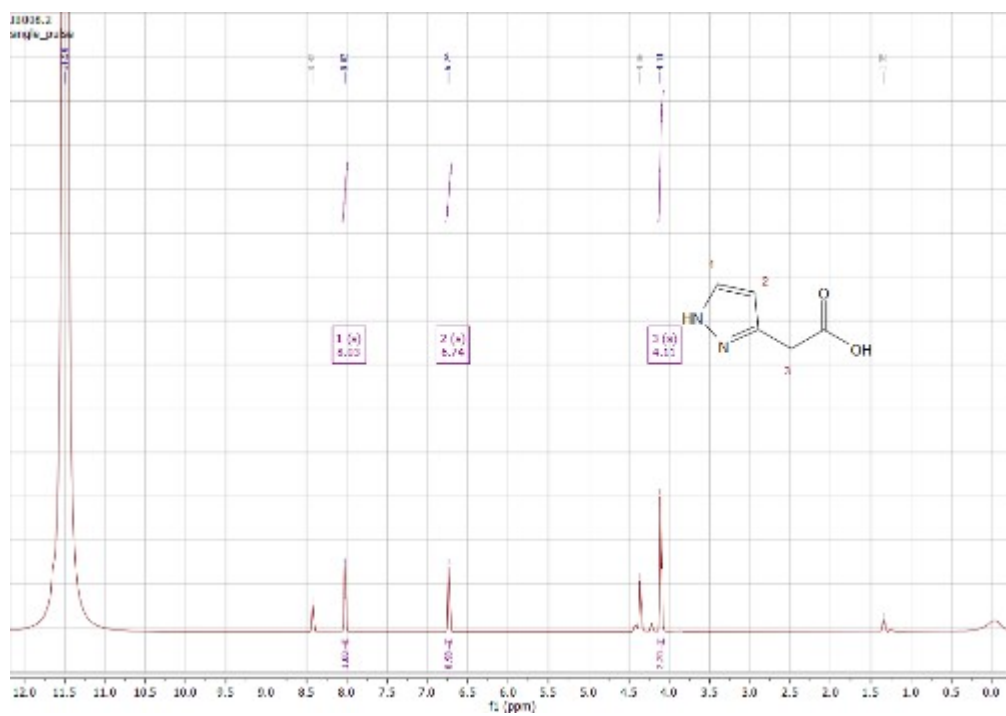


Figure S2.13. ¹H NMR spectrum of 2-(1*H*-pyrazol-3-yl)acetic acid in TFA.

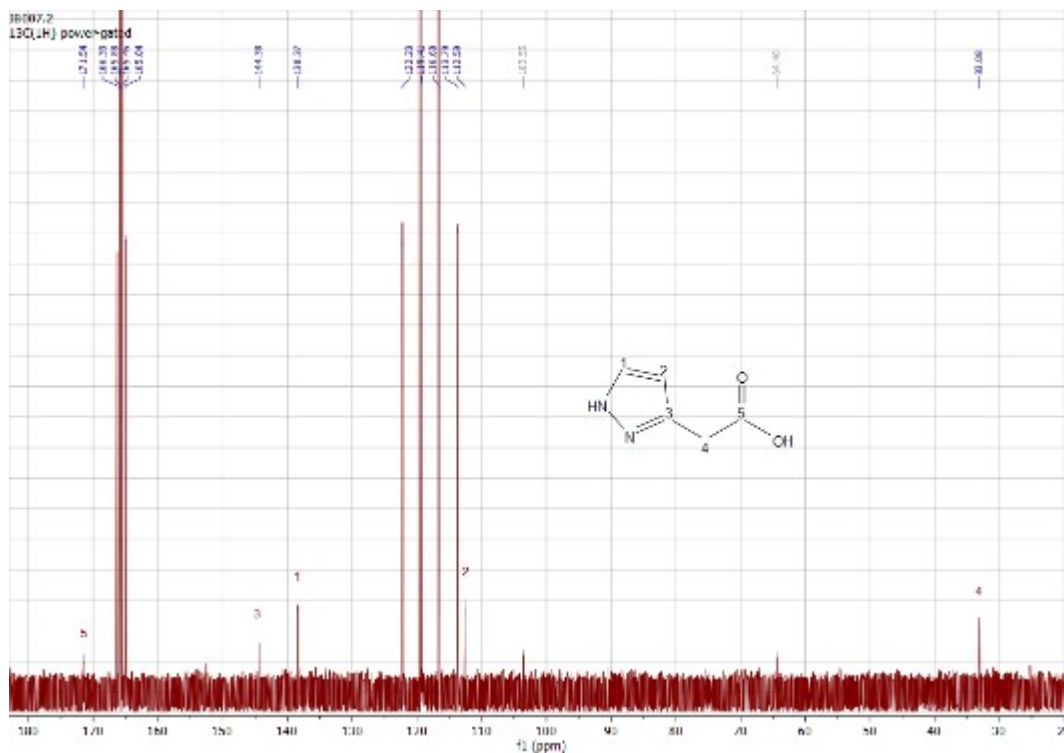


Figure S2.14. ^{13}C NMR spectrum of 2-(1H-pyrazol-3-yl)acetic acid in TFA.

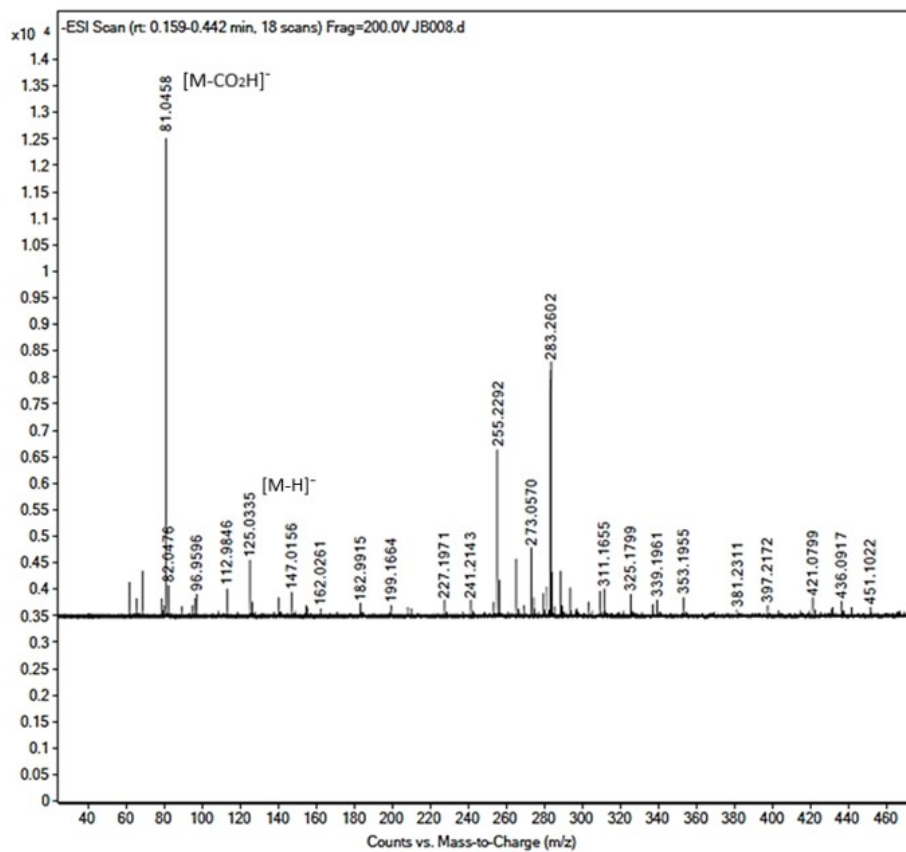


Figure S2.15. Mass spectrum of 2-(1H-pyrazol-3-yl)acetic acid. Dilution with MeOH.

S3 Peptide synthesis

All tetrapeptides were synthesized through standard manual Fmoc solid-phase synthesis protocols by using Rink-amide MBHA resin as the solid support.^{7,8} Amino acids lysine and histidine were Boc- and Trt-protected, respectively.

Synthesis was performed in a syringe reaction vessel (*GPR Rectapur*) using DMF. MBHA resin (200 mg, 0.118 mmol) was allowed swelling during an hour in DMF (3 mL). Fmoc deprotection was performed in 20% piperidine in DMF (3 mL) for 20 min. The resin was washed with DMF (5 x 2 mL) after each deprotection/coupling step. The coupling of the amino acids was carried out in DMF (2 mL) by mixing the corresponding Fmoc-protected amino acid (0.472 mmol, 4 equiv.), PyBOP as the activating agent (246 mg, 0.472 mmol, 4 equiv.) and DIPEA (200 μ L). The mixture was added to the syringes and stirred for 2 h. The coupling of the *N*-heteroaromatic carboxylic acids (1.89 mmol, 16 equiv.) was carried out by stirring for 24 h, instead. After the final coupling step, the resin was washed with DCM (5 x 2 mL), and a mixture of TFA/H₂O/TIPS (90:5:5) (3 mL) was added to the reaction vessel. Cleaving of the peptides from the resin was accomplished for 3 h with stirring. Afterwards, peptides were precipitated and washed twice with cold diethyl ether.

Peptides were purified *via* semi-preparative RP-HPLC (C₁₈ column, 10 μ m, 10 x 250 mm, *Merck*). Products were eluted with H₂O (+ 0.1% TFA) (Solvent A) and MeOH (+ 0.1% TFA) (Solvent B) using the gradient 0–5 min, 5 % B ; 5–40 min, 5 to 95 % B; 40–43 min, 95 % B; 43–48 min, 95 to 5% B. Elution was monitored by UV/VIS absorption at 240 nm (**AA1–AA4** and **CA1–CA5**) and also at 280 nm for **CA1**. Fractions with the peptide trifluoroacetate salts were dried by lyophilization. Purity and identity of peptides were confirmed by analytical RP-HPLC (C₁₈ column, 5 μ m, 3 x 250 mm, *Merck*) and ESI-MS.

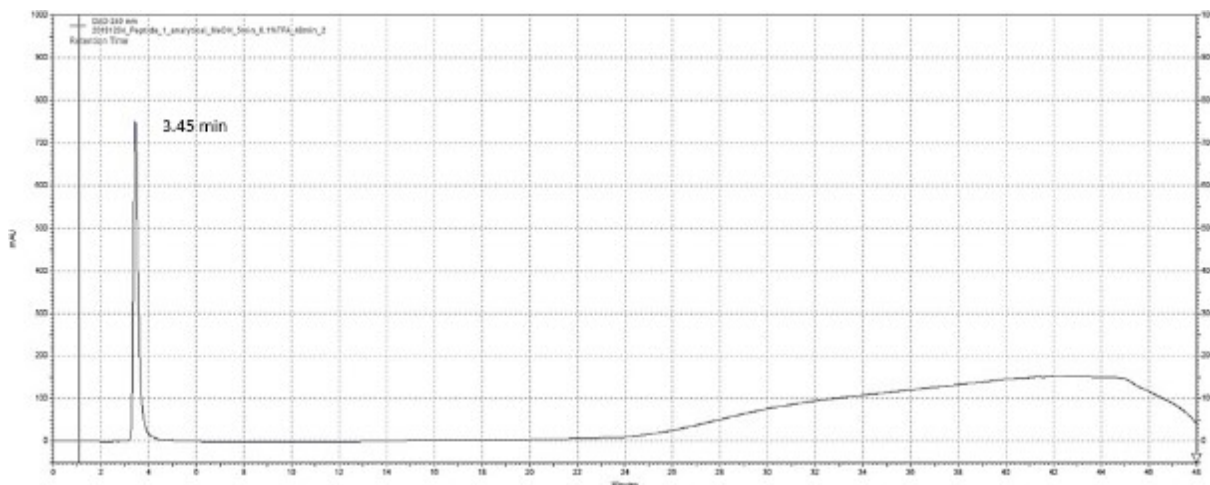


Figure S3.1. Chromatogram of the analytical run for **AA1** obtained by RP-HPLC.

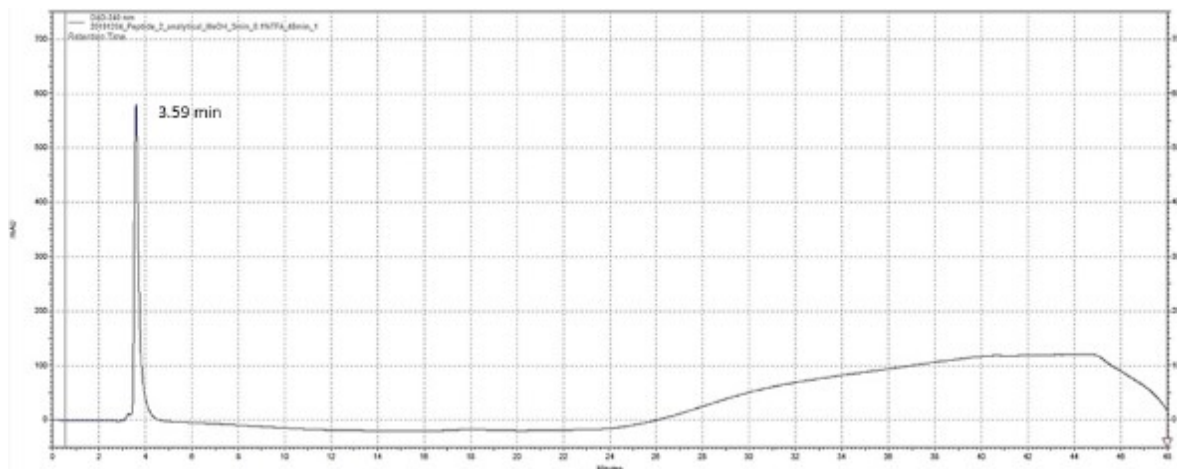


Figure S3.2. Chromatogram of the analytical run for **AA2** obtained by RP-HPLC.

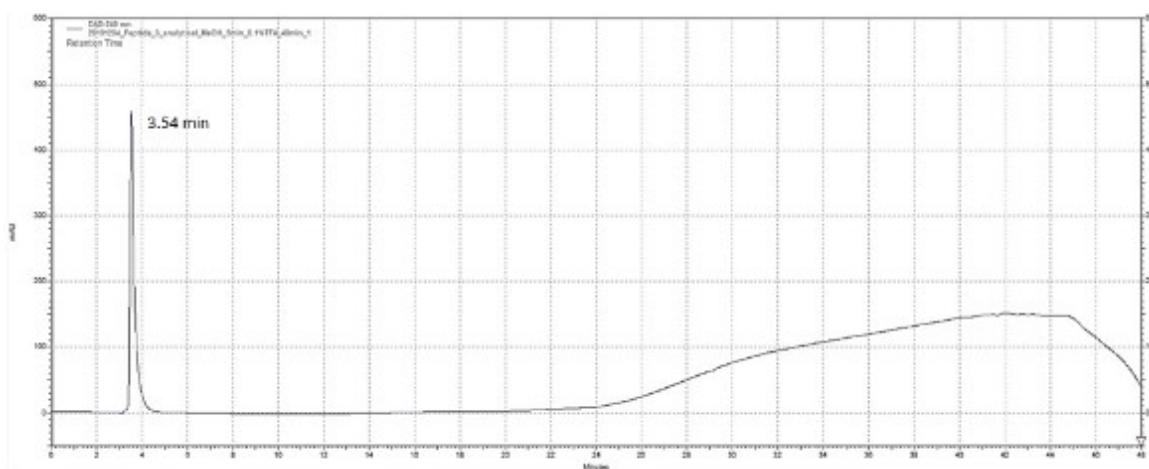


Figure S3.3. Chromatogram of the analytical run for **AA3** obtained by RP-HPLC.

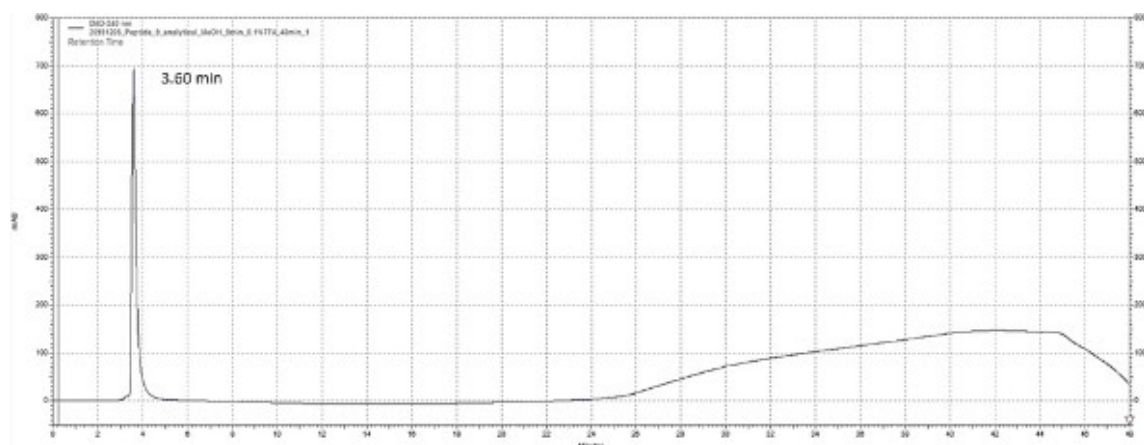


Figure S3.4. Chromatogram of the analytical run for **AA4** obtained by RP-HPLC.

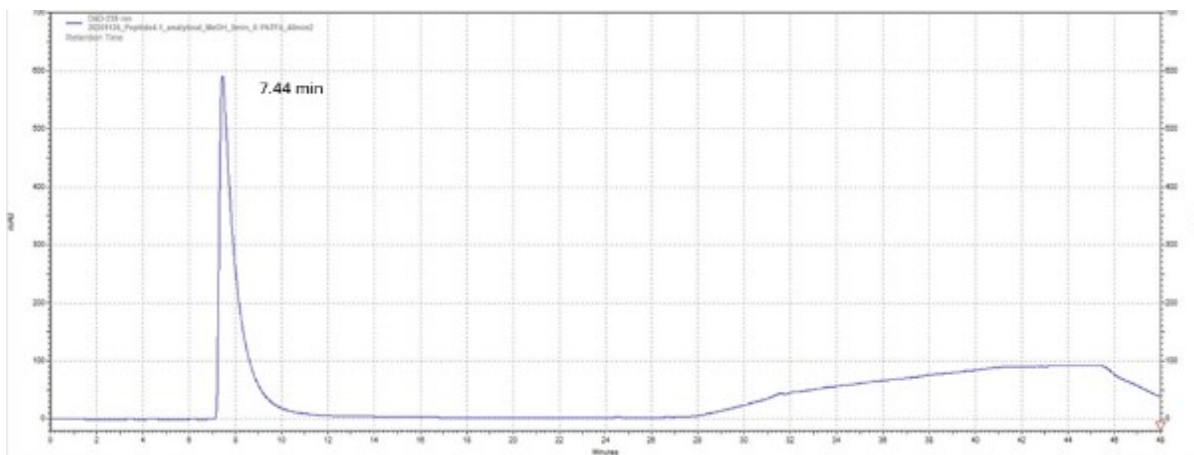


Figure S3.5. Chromatogram of the analytical run for **CA1** obtained by RP-HPLC.

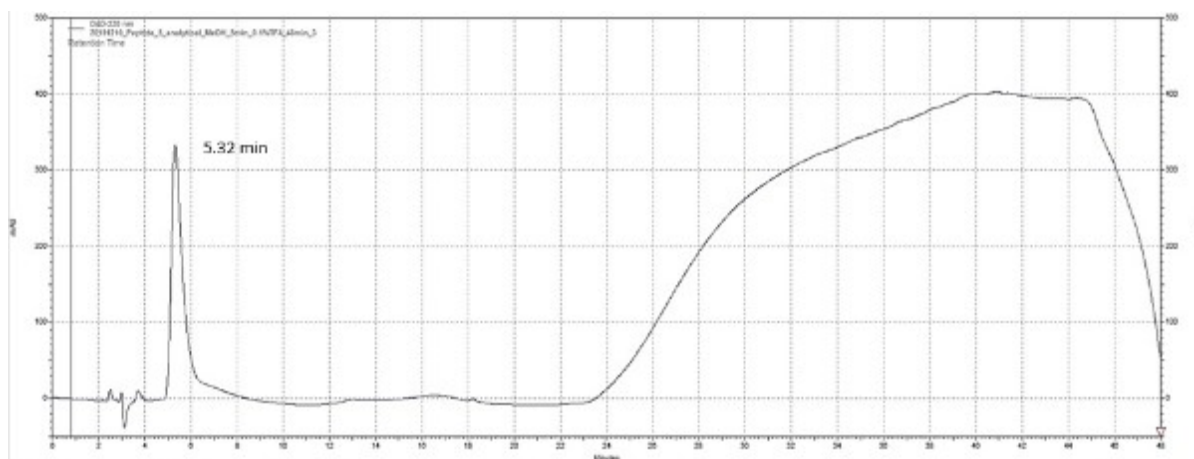


Figure S3.6. Chromatogram of the analytical run for **CA2** obtained by RP-HPLC.

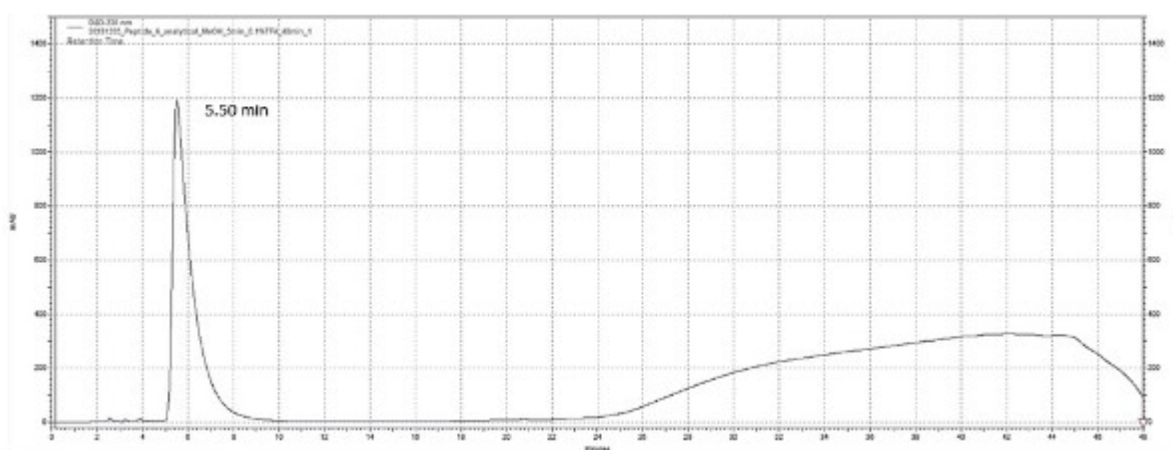


Figure S3.7. Chromatogram of the analytical run for **CA3** obtained by RP-HPLC.

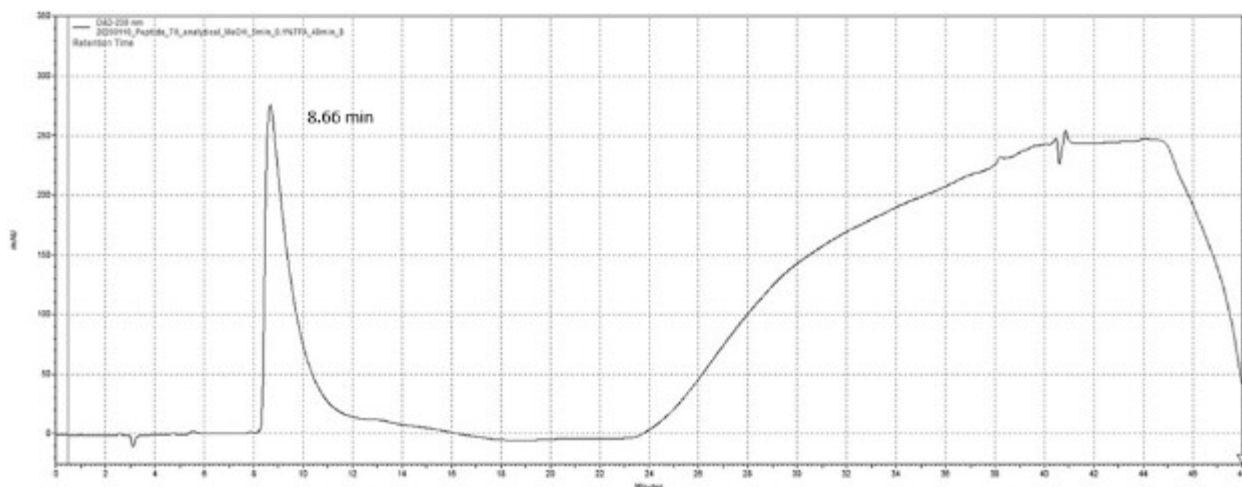


Figure S3.8. Chromatogram of the analytical run for CA4 obtained by RP-HPLC.

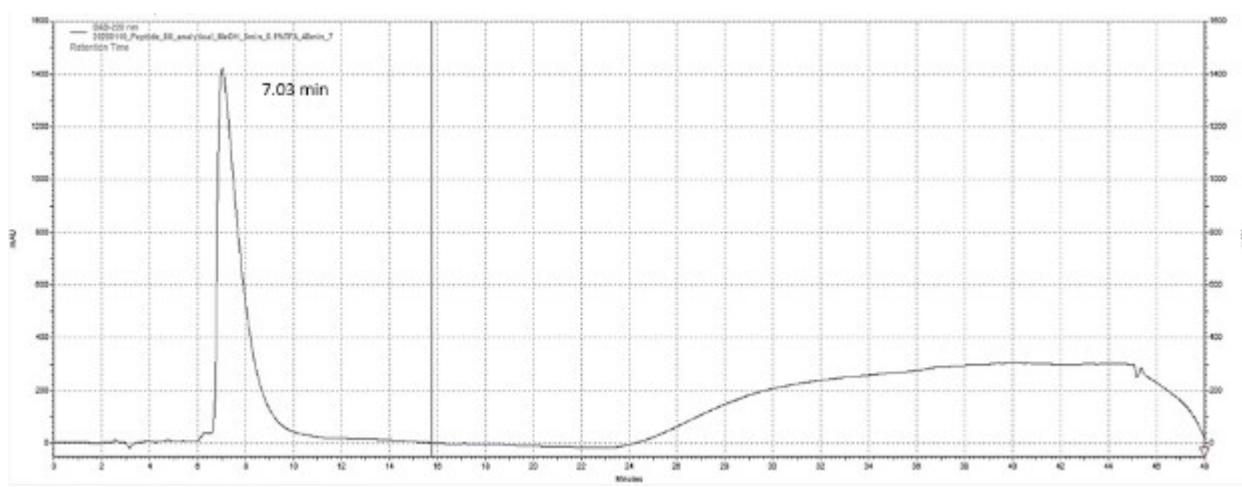


Figure S3.9. Chromatogram of the analytical run for CA5 obtained by RP-HPLC.

Table S3.1. Calculated and found m/z values in the ESI mass spectra of peptides **AA1–AA4** and **CA1–CA5**.

Peptide	$[M + H]^+$		$[2M + H]^+$	
	Calculated	Found	Calculated	Found
AA1	397.2306	397.2285	793.4540	793.4503
AA2	425.2619	425.2590	849.5166	849.5121
AA3	411.2463	411.2460	821.4853	821.4831
AA4	411.2463	411.2443	821.4853	821.4809
CA1	473.2619	473.2596	945.5166	945.5135
CA2	463.2524	463.2512	925.4976	925.4993
CA3	463.2524	463.2498	925.4976	925.4926
CA4	462.2572	462.2562	923.5071	923.5033
CA5	462.2572	462.2589	923.5071	923.5096

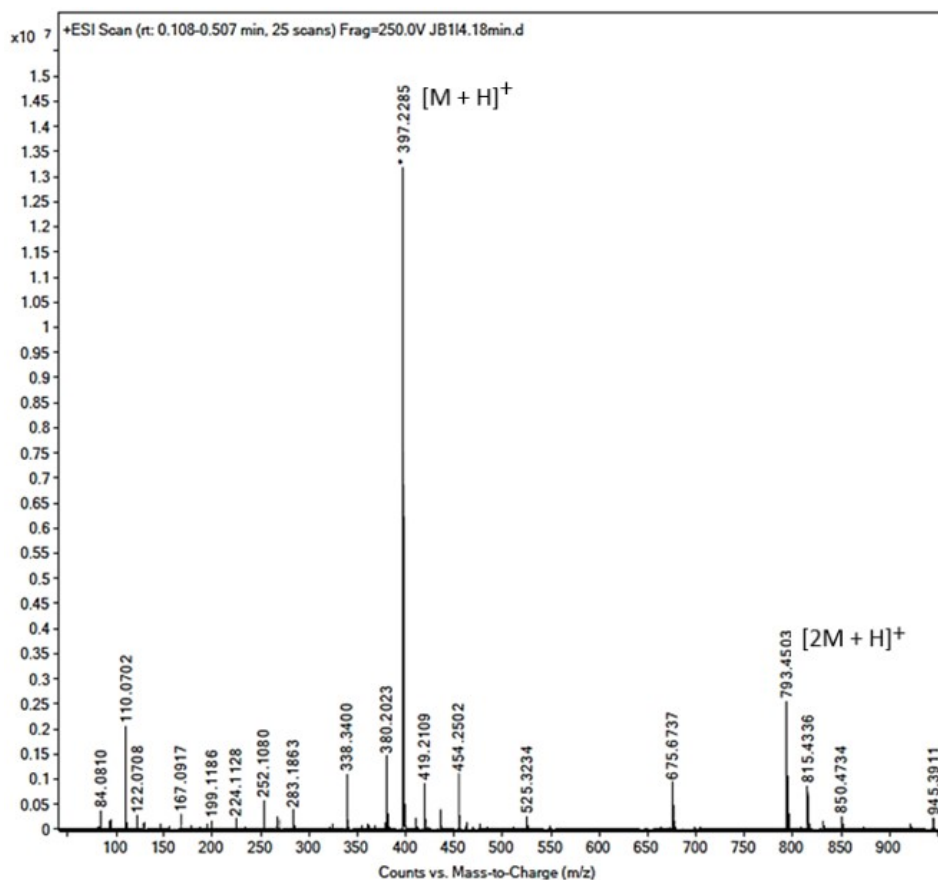


Figure S3.10. Mass spectrum of **AA1**. Dilution with MeOH.

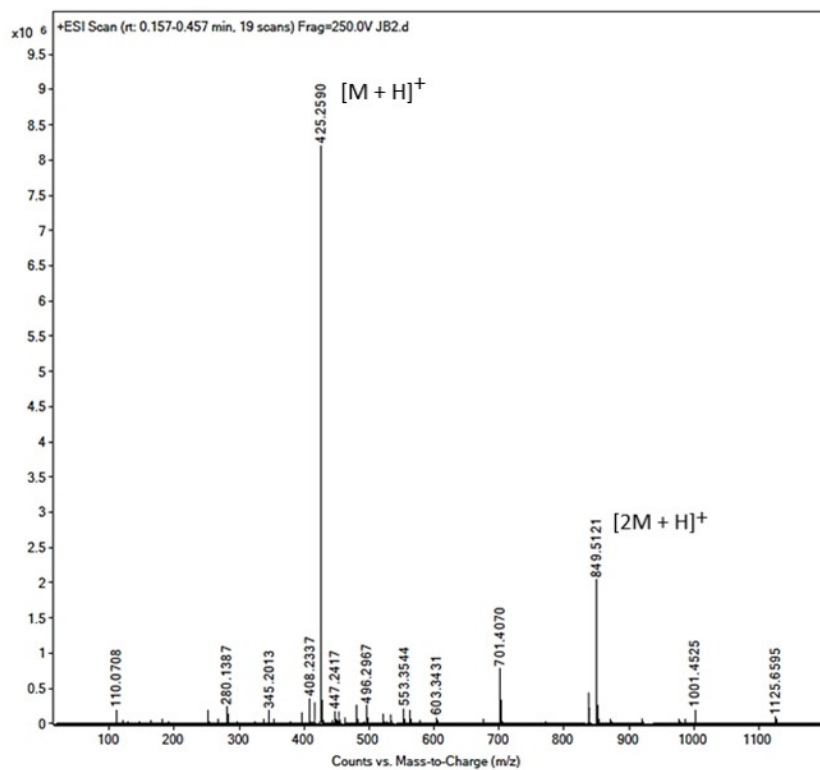


Figure S3.11. Mass spectrum of AA2. Dilution with MeOH.

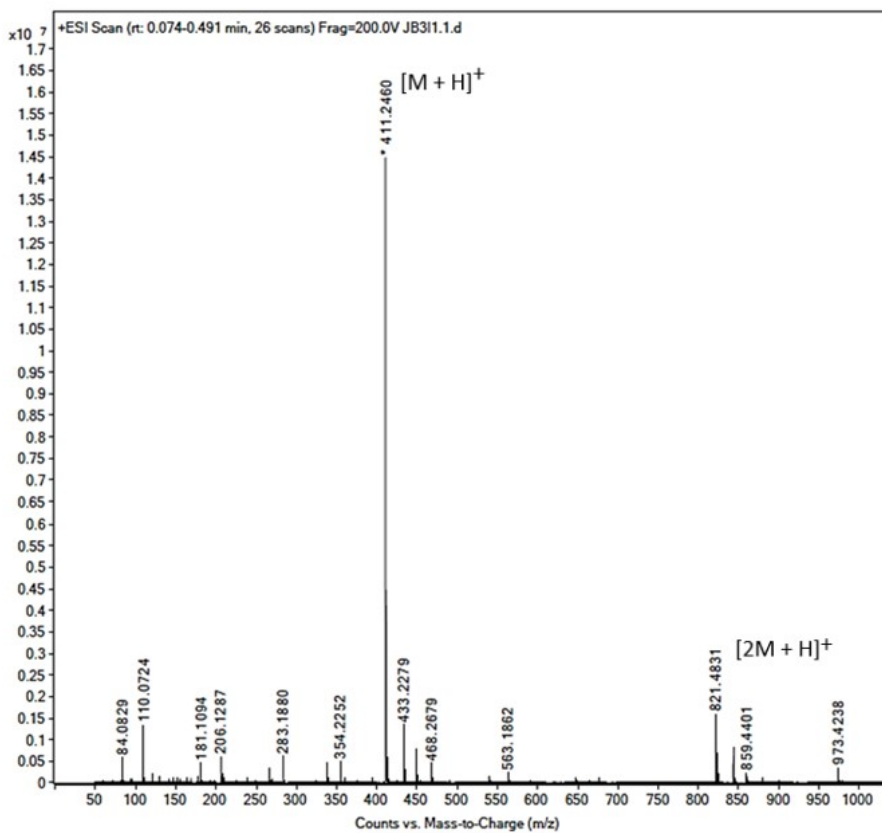


Figure S3.12. Mass spectrum of AA3. Dilution with MeOH.

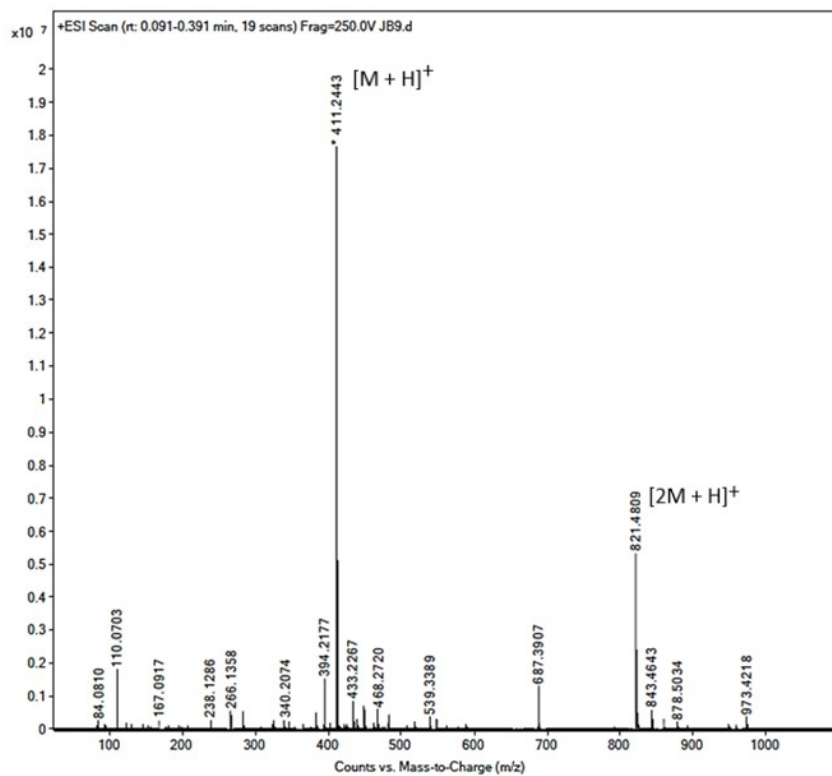


Figure S3.13. Mass spectrum of AA4. Dilution with MeOH.

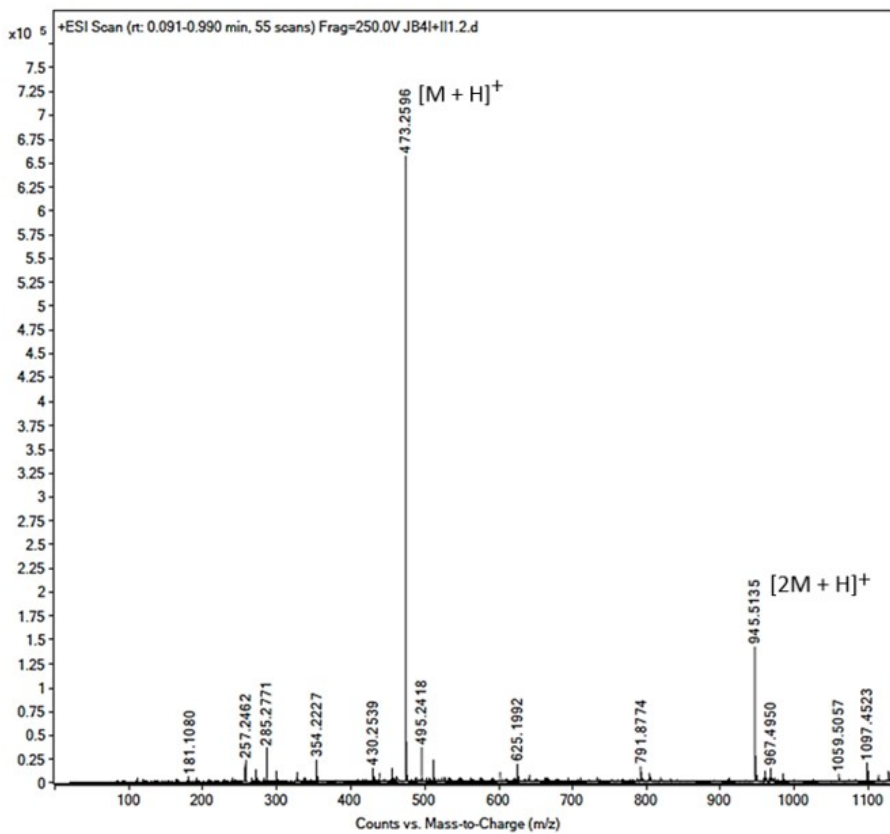


Figure S3.14. Mass spectrum of CA1. Dilution with MeOH.

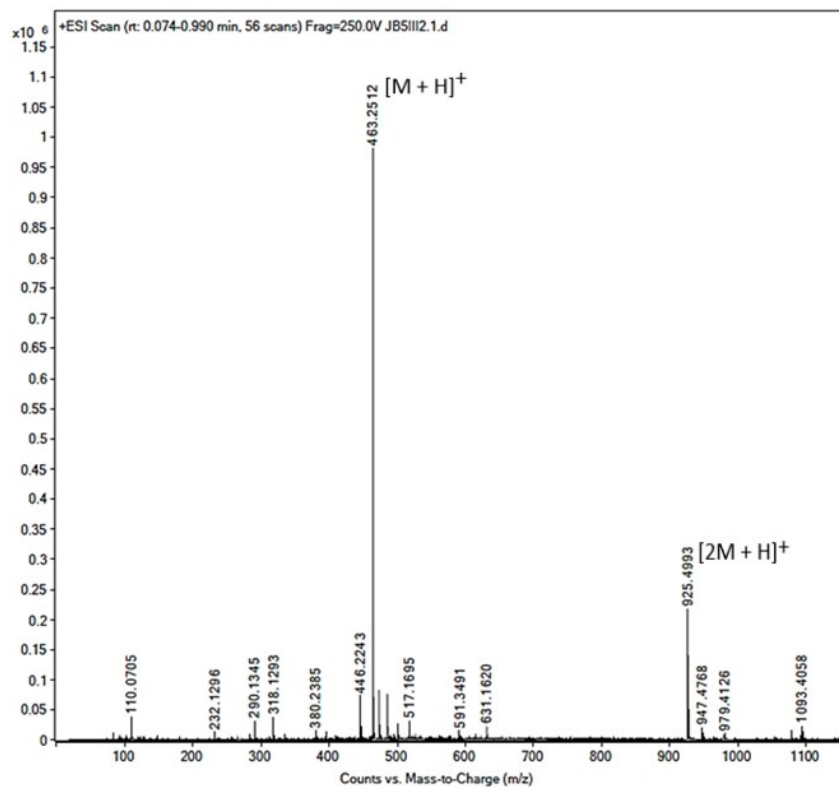


Figure S3.15. Mass spectrum of CA2. Dilution with MeOH.

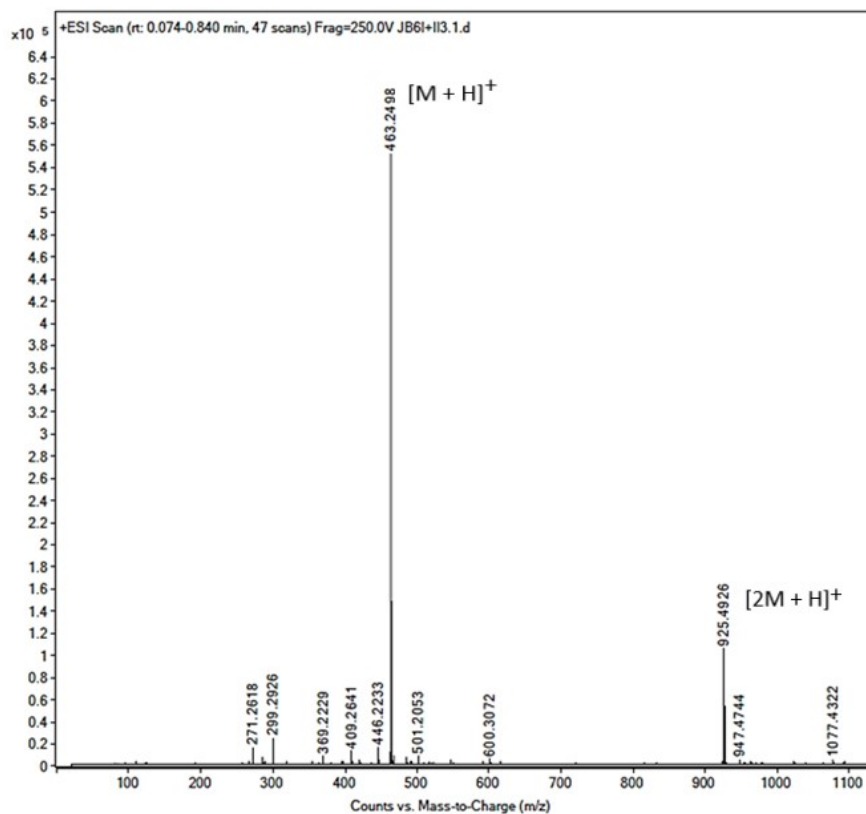


Figure S3.16. Mass spectrum of CA3. Dilution with MeOH.

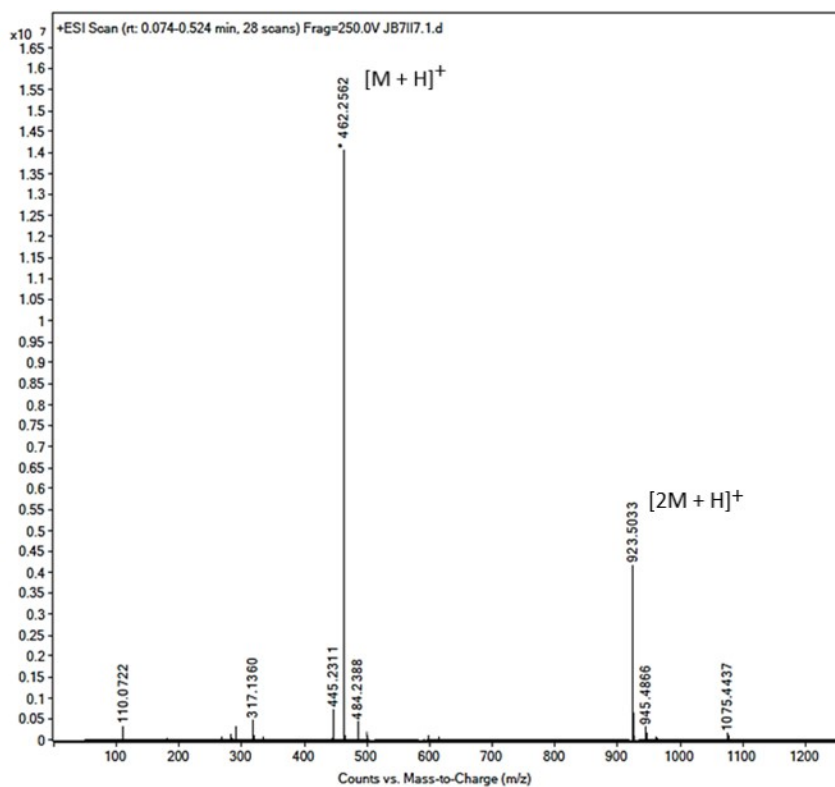


Figure S3.17. Mass spectrum of CA4. Dilution with MeOH.

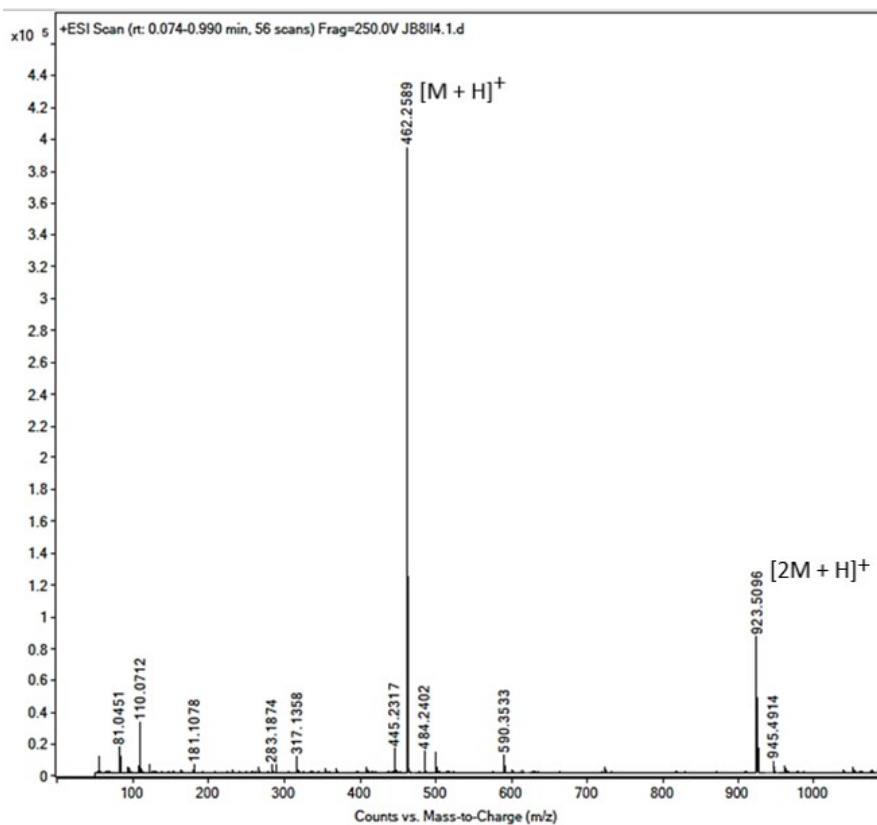


Figure S3.18. Mass spectrum of **CA5**. Dilution with MeOH.

Yields and concentrations of eluted peptide trifluoroacetate salts were determined by UV/VIS spectroscopy considering the presence of three trifluoroacetate counterions due to protonation of the imidazole nitrogen (His) and amine group of the lysine residue, and the terminal amine group (**AA1–AA4**) and the *N*-heteroaromatic (**CA1–CA5**), respectively.

Based on the *d-d* transition band observed for Cu(II)-ATCUN complexes, titration of peptide solutions (assuming 1 mM as the initial concentration from weighing as trifluoroacetate salt with just estimated amount of trifluoroacetate counterions) with steps of CuCl₂·2H₂O 0.05 mM (0.05 equiv.) in the presence of MOPS buffer (pH 7.4, 50 mM) was performed until observing the saturation point of the characteristic absorption band.⁹ Yields and concentrations of tetrapeptides were finally recalculated.

Table S3.2. Correction of the peptide concentration of **AA1–AA4** and **CA1–CA5** by the detection of the saturation point observed in the *d-d* transition band of Cu(II) complexes formed.

Peptide	Saturation point (equivalents)	Initial concentration (mM)	Adjusted concentration (mM)	Complex	λ_{\max} (nm) <i>d-d</i> transition band
AA1	0.90	50	45.0	Cu-AA1	527
AA2	0.70	50	37.5	Cu-AA2	670
AA3	0.85	50	42.5	Cu-AA3	555
AA4	0.80	50	40.0	Cu-AA4	539
CA1	0.55	50	27.5	Cu-CA1	594
CA2	0.35	50	17.5	Cu-CA2	634
CA3	0.40	10	4.0	Cu-CA3	670
CA4	0.45	50	22.5	Cu-CA4	603
CA5	0.40	25	10.0	Cu-CA5	645

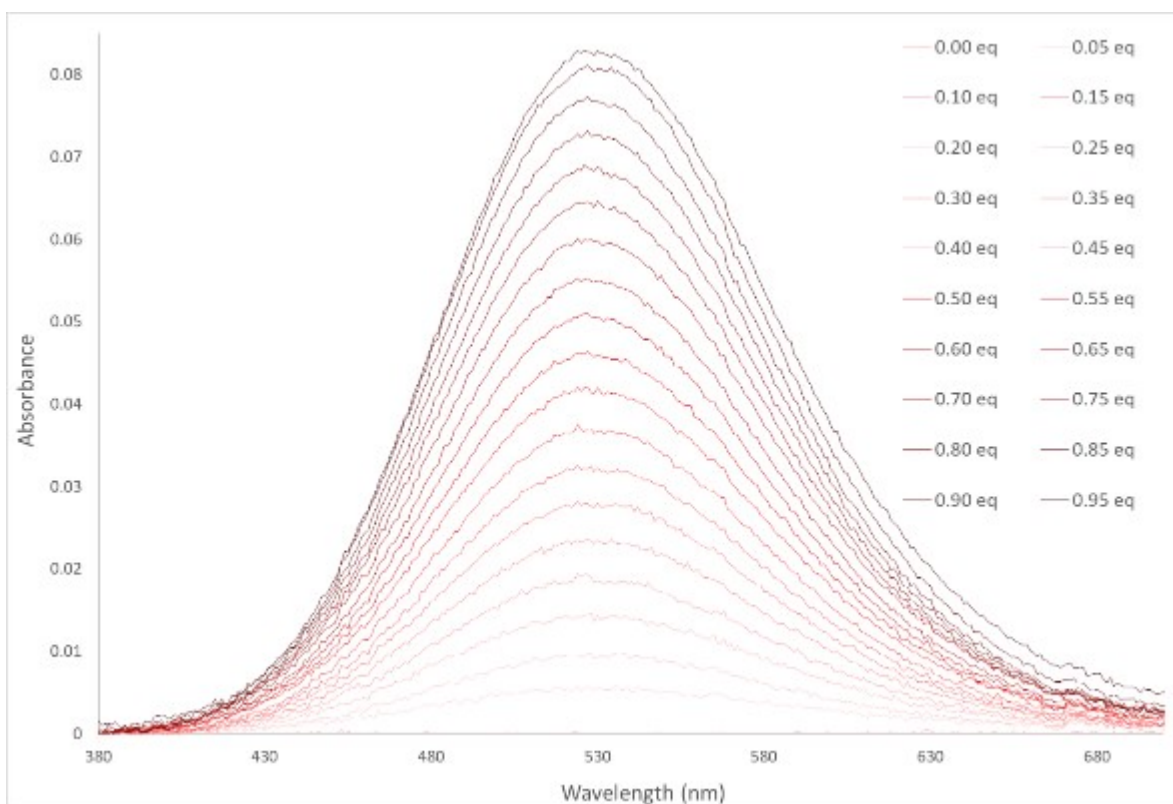


Figure S3.19. *d-d* transition band in the absorption spectrum of **Cu-AA1** with increasing concentrations of CuCl_2 (0.05 mM, 0.05 equiv.) in the presence of MOPS buffer (50 mM, pH 7.4).

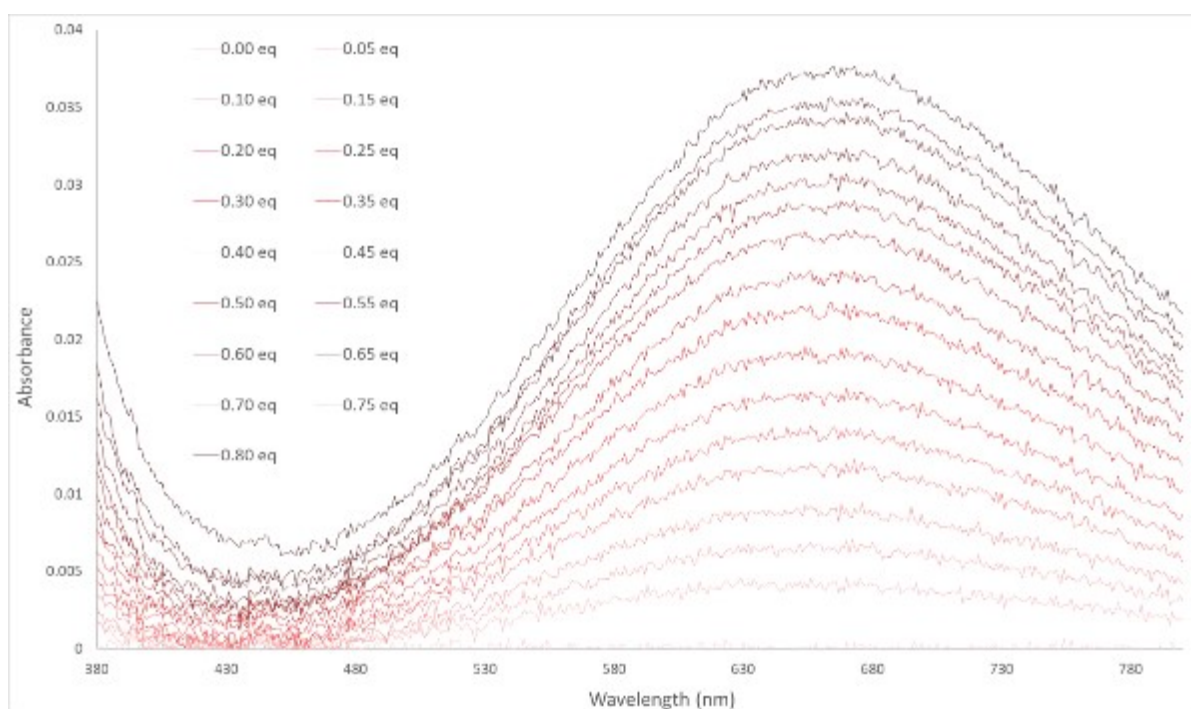


Figure S3.20. *d-d* transition band in the absorption spectrum of **Cu-AA2** with increasing concentrations of CuCl_2 (0.05 mM, 0.05 equiv.) in the presence of MOPS buffer (50 mM, pH 7.4).

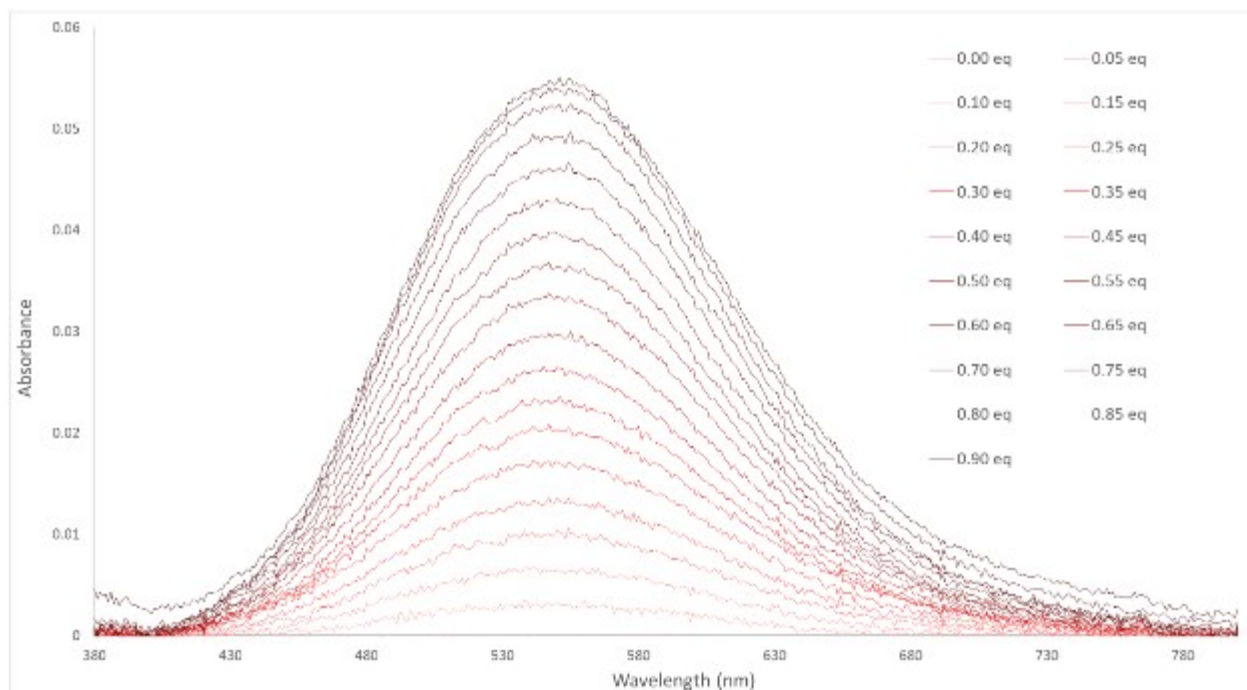


Figure S3.21. *d-d* transition band in the absorption spectrum of **Cu-AA3** with increasing concentrations of CuCl_2 (0.05 mM, 0.05 equiv.) in the presence of MOPS buffer (50 mM, pH 7.4).

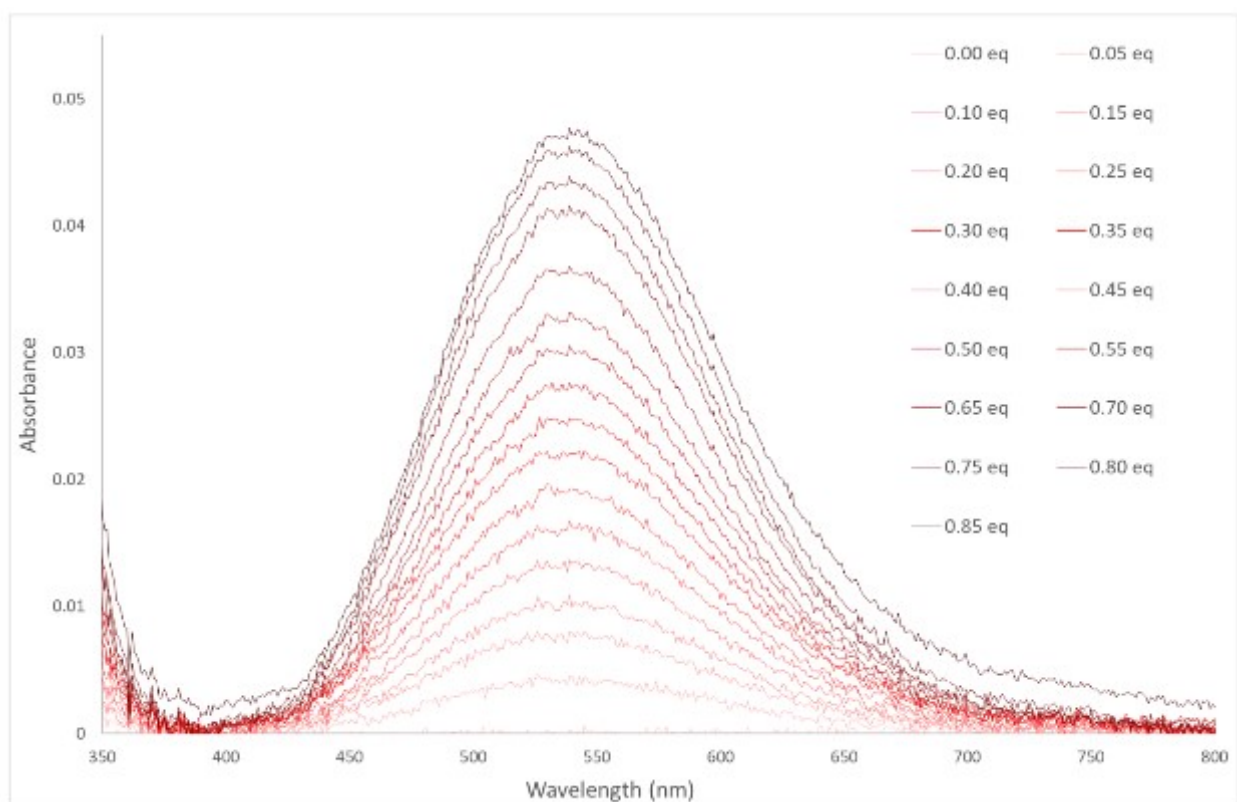


Figure S3.22. *d-d* transition band in the absorption spectrum of **Cu-AA4** with increasing concentrations of CuCl_2 (0.05 mM, 0.05 equiv.) in the presence of MOPS buffer (50 mM, pH 7.4).

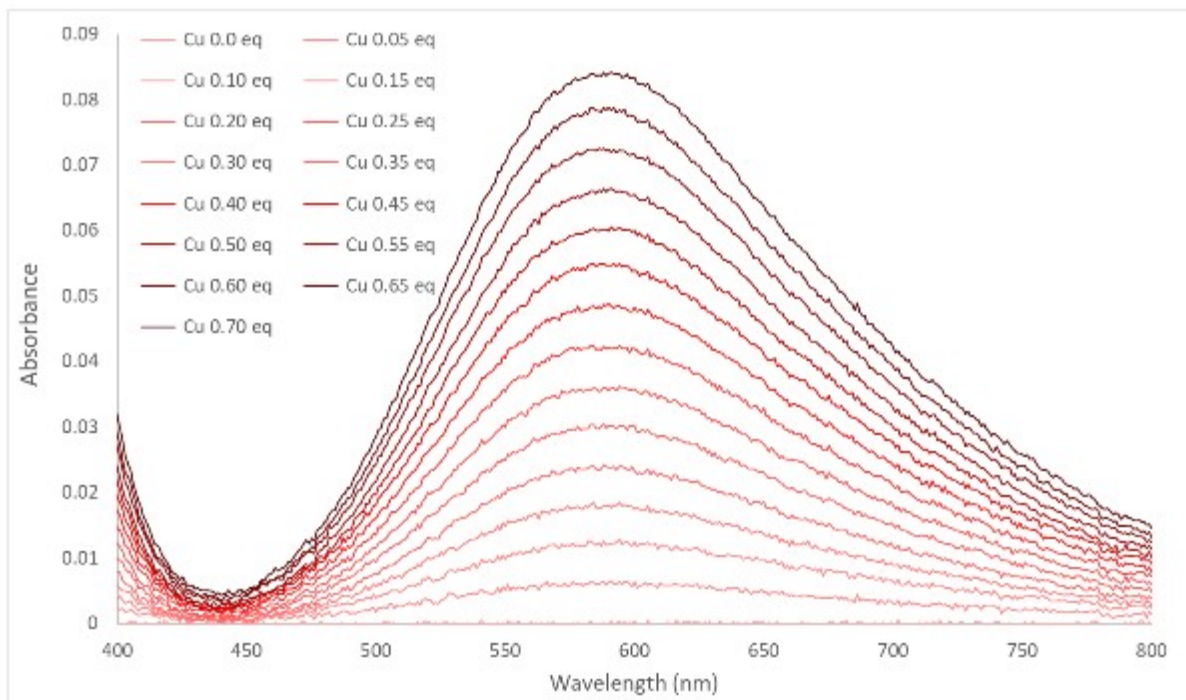


Figure S3.23. *d-d* transition band in the absorption spectrum of **Cu-CA1** with increasing concentrations of CuCl_2 (0.05 mM, 0.05 equiv.) in the presence of MOPS buffer (50 mM, pH 7.4).

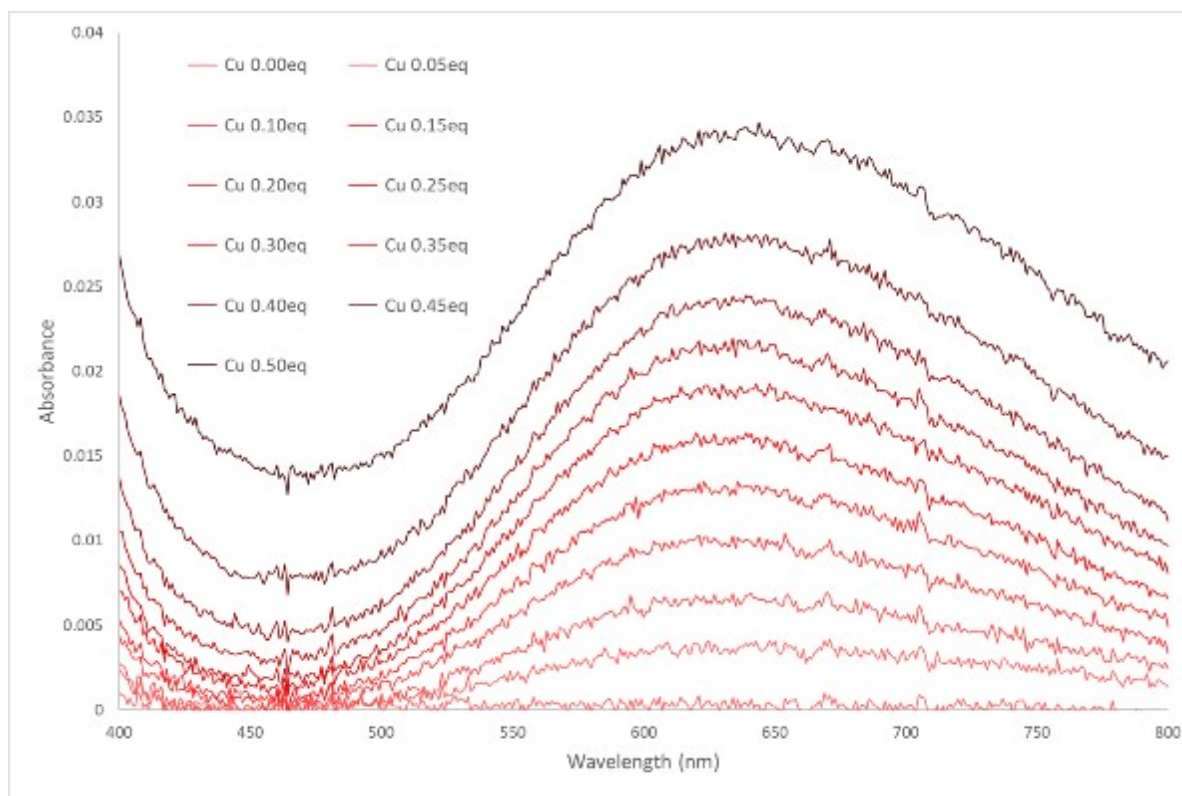


Figure S3.24. *d-d* transition band in the absorption spectrum of **Cu-CA2** with increasing concentrations of CuCl_2 (0.05 mM, 0.05 equiv.) in the presence of MOPS buffer (50 mM, pH 7.4).

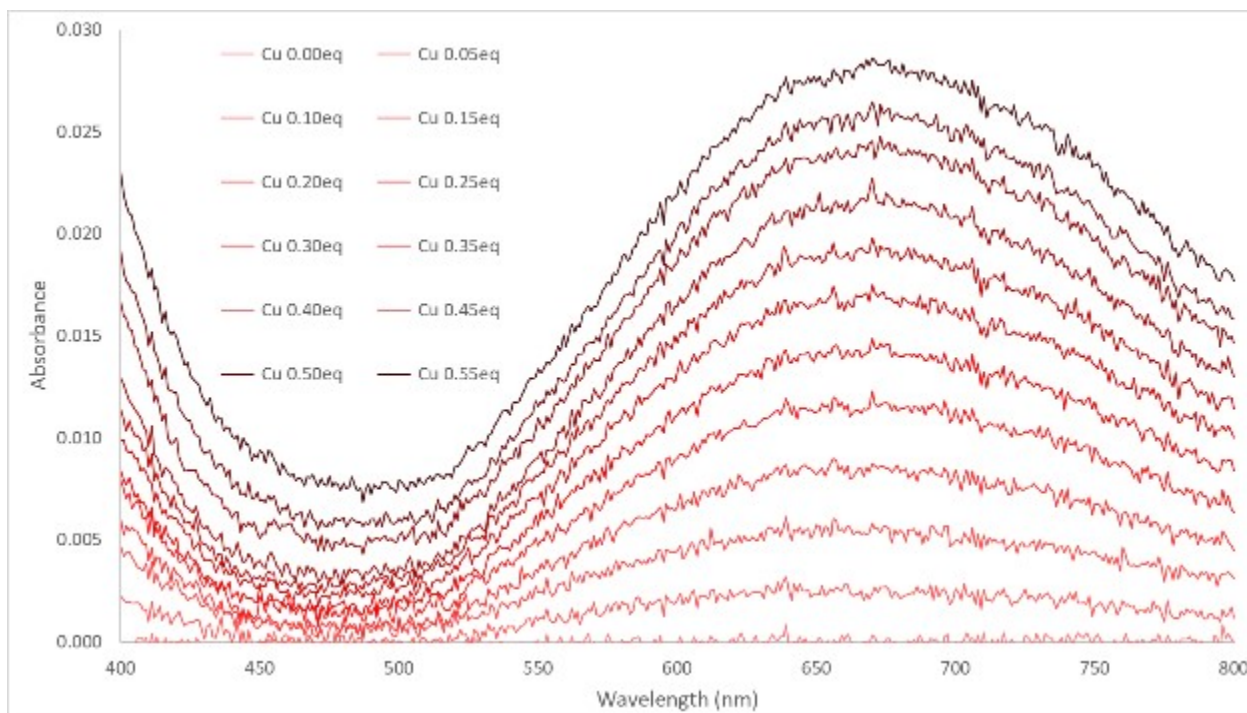


Figure S3.25. *d-d* transition band in the absorption spectrum of **Cu-CA3** with increasing concentrations of CuCl₂ (0.05 mM, 0.05 equiv.) in the presence of MOPS buffer (50 mM, pH 7.4).

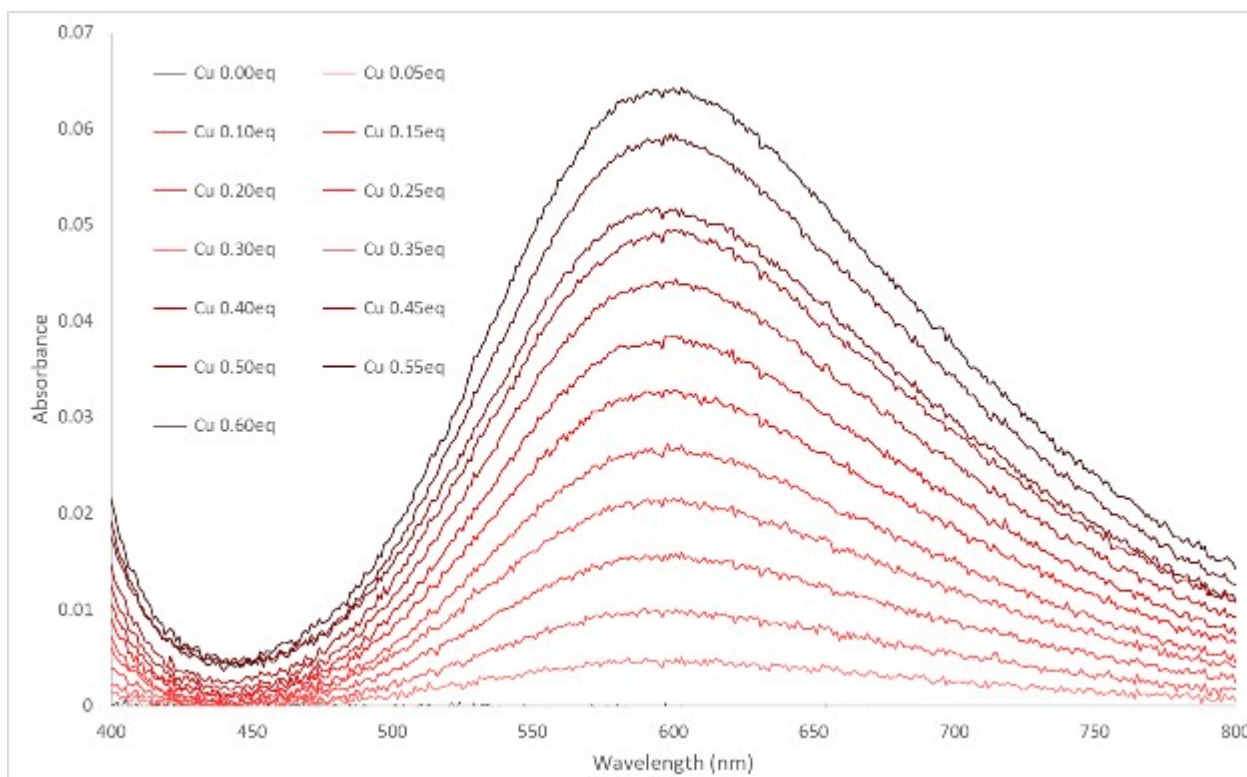


Figure S3.26. *d-d* transition band in the absorption spectrum of **Cu-CA4** with increasing concentrations of CuCl₂ (0.05 mM, 0.05 equiv.) in the presence of MOPS buffer (50 mM, pH 7.4).

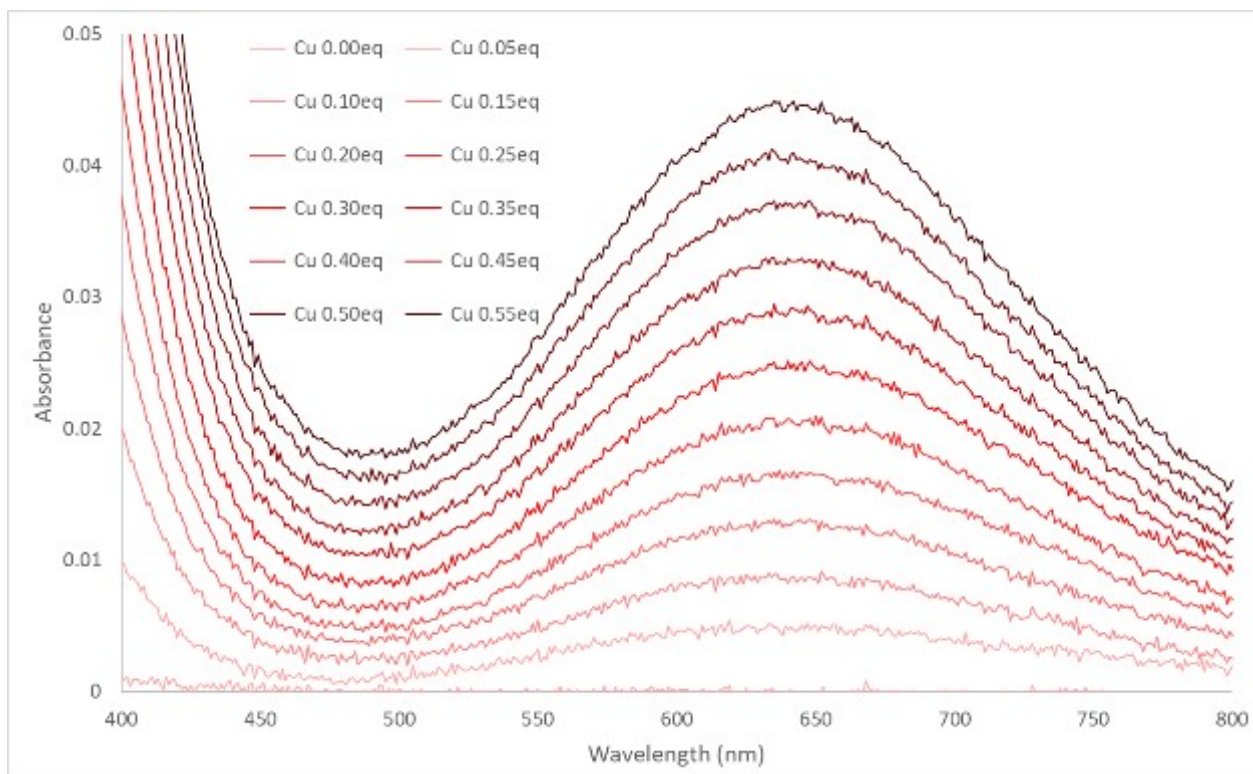


Figure S3.27. *d-d* transition band in the absorption spectrum of **Cu-CA5** with increasing concentrations of **CuCl₂** (0.05 mM, 0.05 equiv.) in the presence of MOPS buffer (50 mM, pH 7.4).

S4 Cu(II) complex synthesis and characterization

Complexes were prepared *in situ* by mixing solutions of CuCl₂ and peptides in the presence of MOPS buffer (20-fold excess, pH 7.4). For the subsequent DNA cleavage and ROS detection analysis by gel electrophoresis, complex solutions were prepared in a ratio of 1:1.25 Cu/peptide in order to ensure the absence of free Cu(II) in solution. For DNA binding studies by UV/VIS and CD spectroscopy as well as CV measurements complex solutions were prepared in a ratio of 1:1.05 Cu/peptide.

Their identities were verified by ESI-MS with complex solutions of a ratio of 1:1.25 CuCl₂/peptide and two-fold excess MOPS buffer at (pH 7.4) in a mixture H₂O/MeOH 1:5.

Table S4.1. Calculated and found m/z values in the ESI mass spectra of complexes **Cu-AA1–Cu-AA4** and **Cu-CA1–Cu-CA5**, * M refers to [Cu²⁺ + peptide].

Complex	[M – H] ⁺⁺		[M + Cl] ⁺⁺	
	Calculated	Found	Calculated	Found
Cu-AA1	458.1446	458.1454	494.1213	-
Cu-AA2	486.1759	486.1750	522.1526	522.1518
Cu-AA3	472.1602	472.1614	508.1369	508.1386
Cu-AA4	472.1602	472.1612	508.1369	-
Cu-CA1	534.1759	534.2166	570.1526	570.1546
Cu-CA2	524.1664	524.1679	560.1431	560.1436
Cu-CA3	524.1664	524.1683	560.1431	-
Cu-CA4	523.1711	523.1724	559.1478	559.1494
Cu-CA5	523.1711	523.1720	559.1478	559.1486

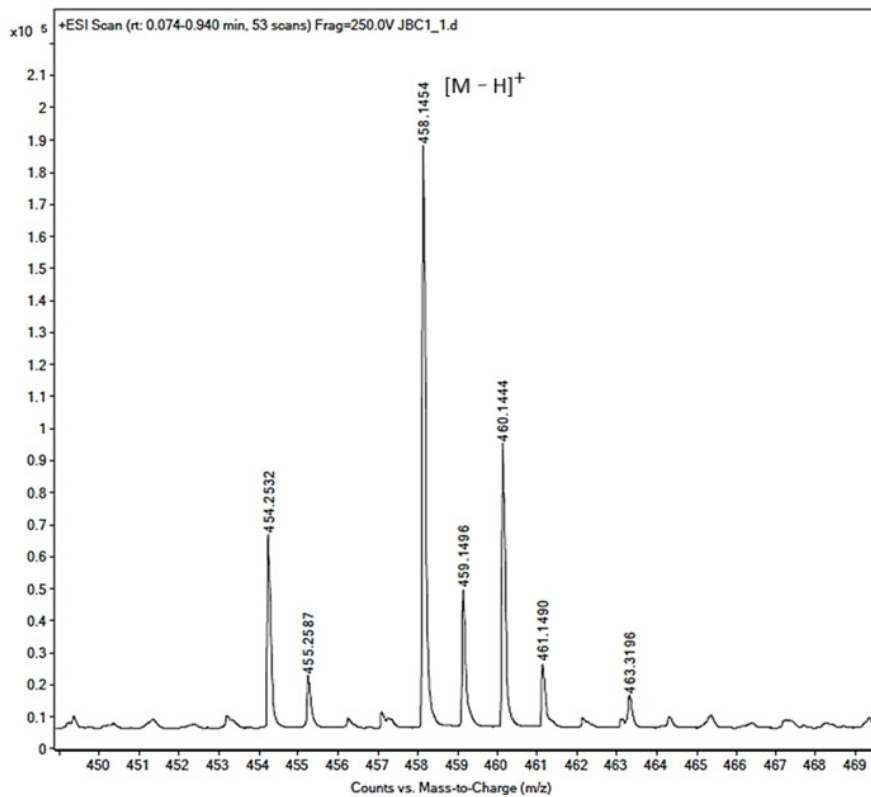


Figure S4.1. Mass spectrum of Cu-AA1. Dilution with H₂O/MeOH 1:5.

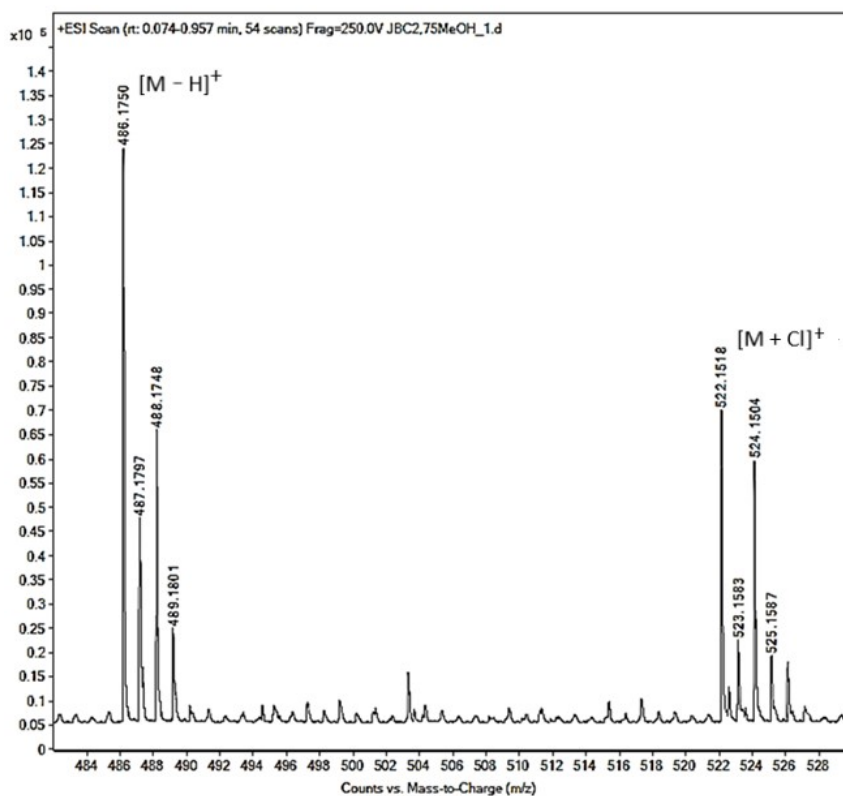


Figure S4.2. Mass spectrum of Cu-AA2. Dilution with H₂O/MeOH 1:5.

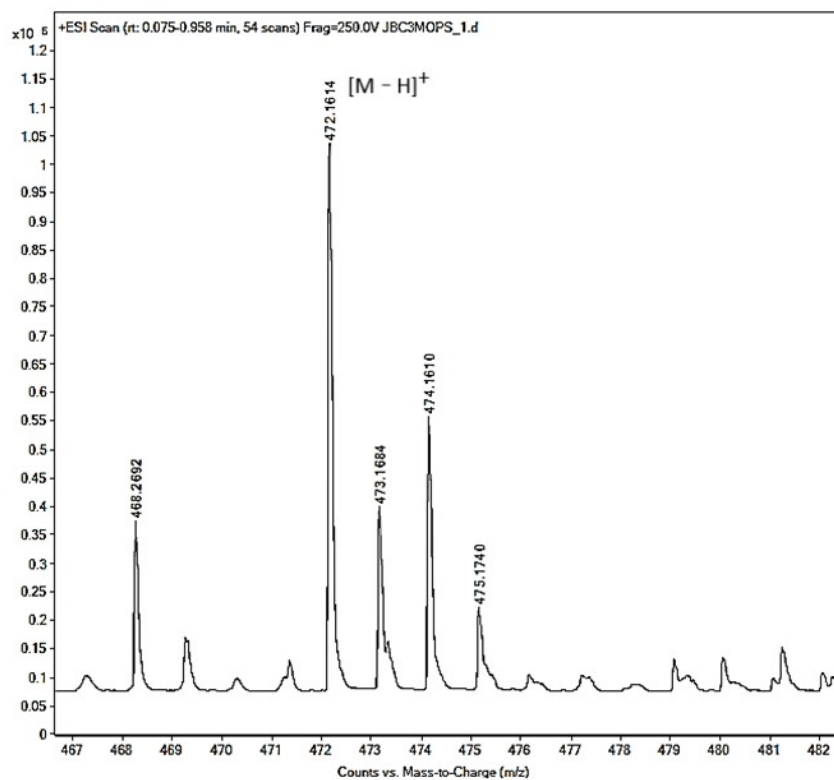


Figure S4.3. Mass spectrum of **Cu-AA3**. Dilution with H₂O/MeOH 1:5.

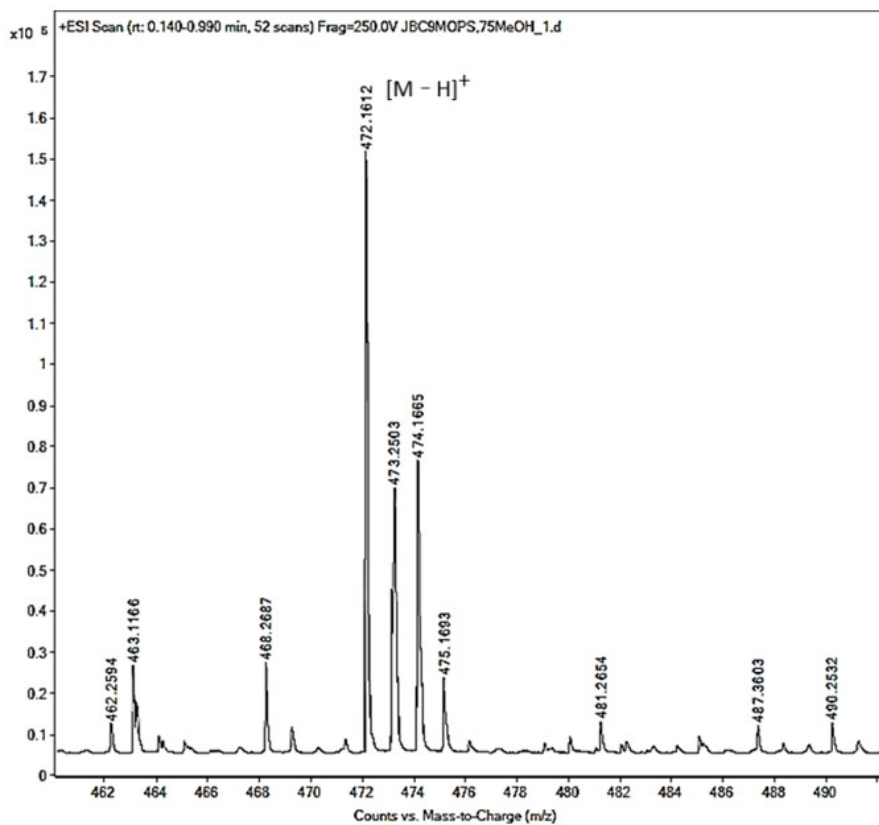


Figure S4.4. Mass spectrum of **Cu-AA4**. Dilution with H₂O/MeOH 1:5.

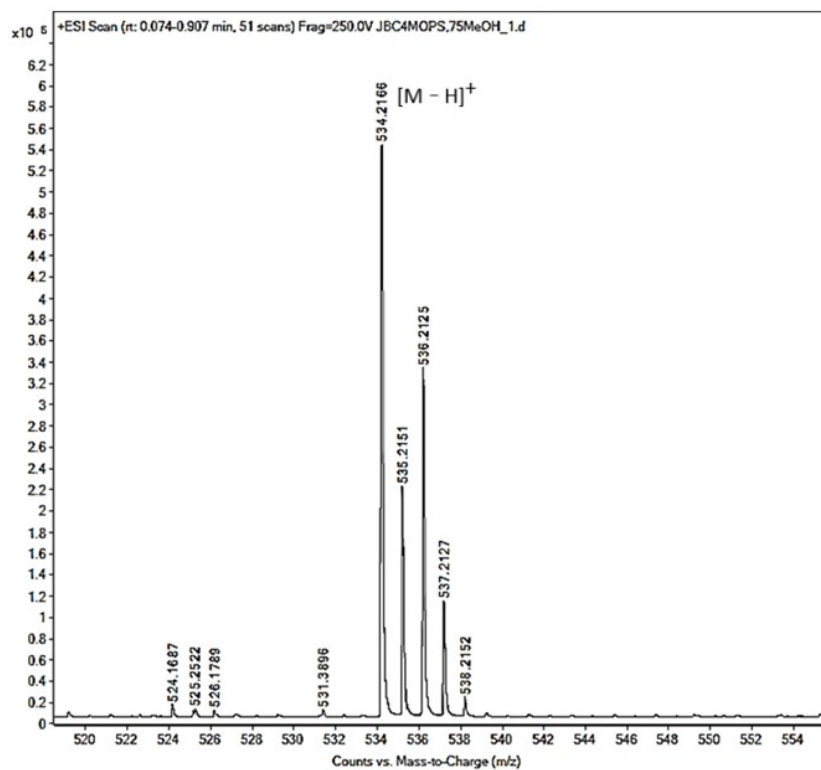


Figure S4.5. Mass spectrum of Cu-CA1. Dilution with H₂O/MeOH 1:5.

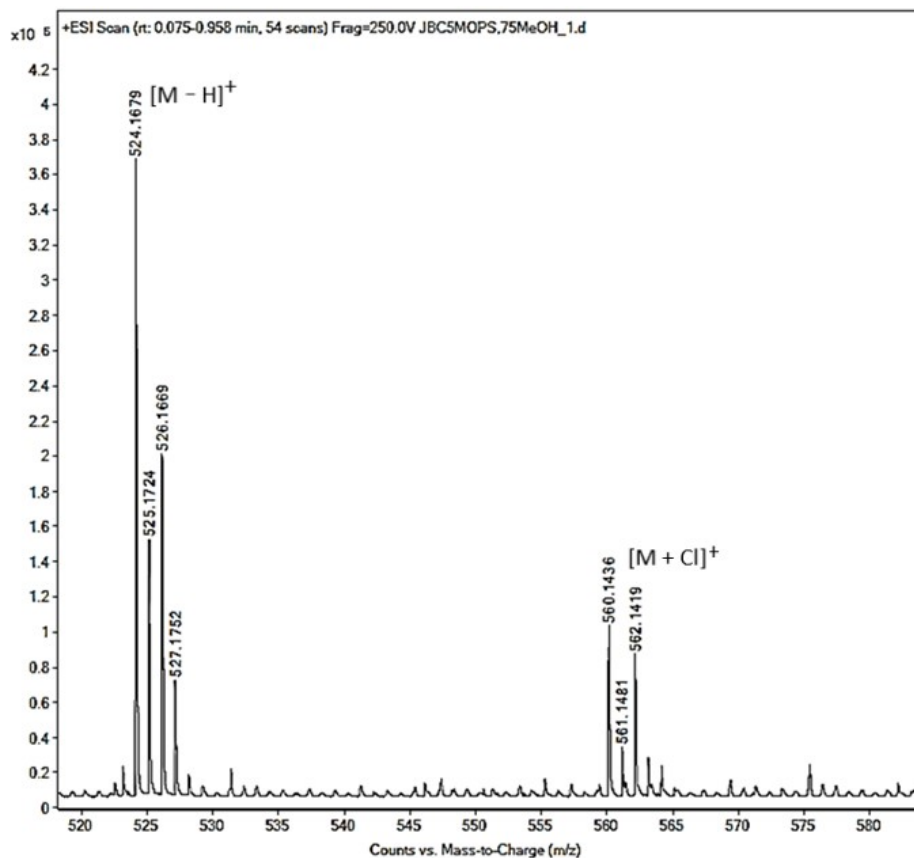


Figure S4.6. Mass spectrum of Cu-CA2. Dilution with H₂O/MeOH 1:5.

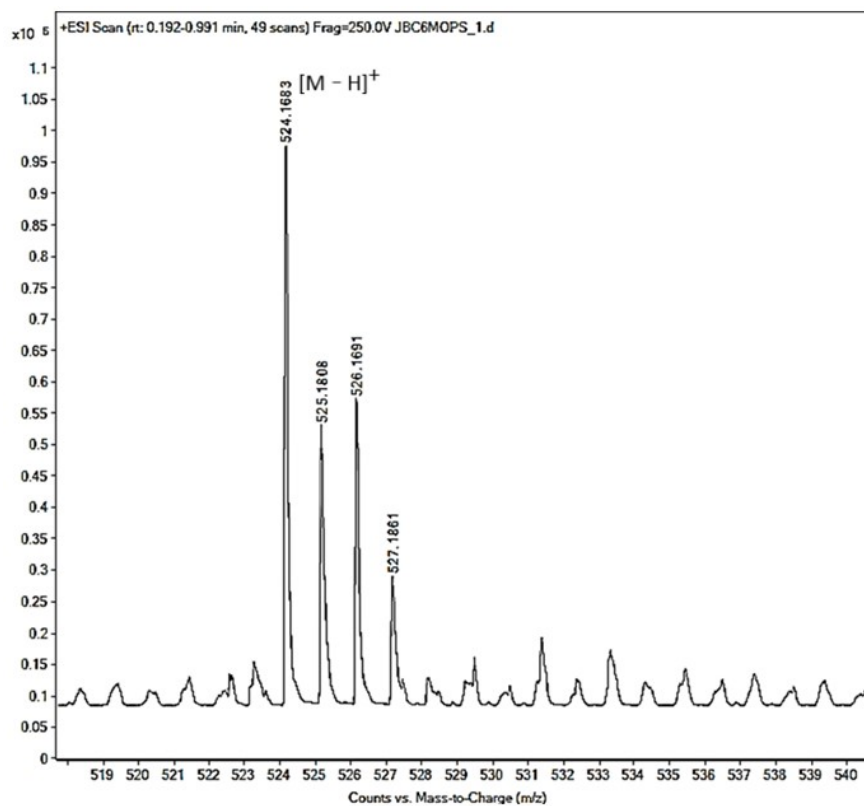


Figure S4.7. Mass spectrum of **Cu-CA3**. Dilution with H₂O/MeOH 1:5.

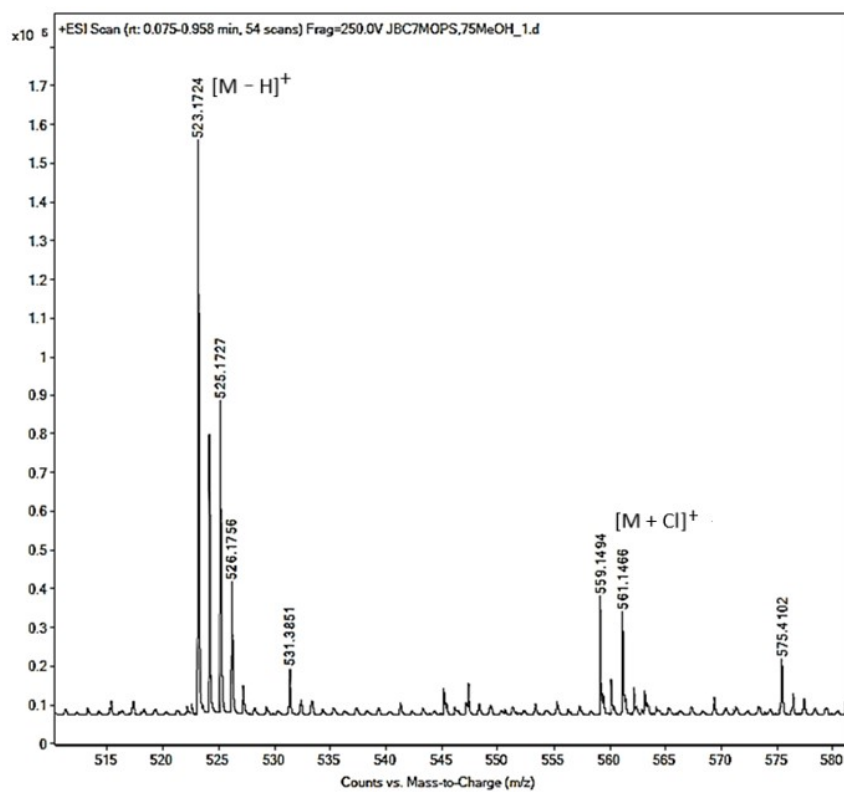


Figure S4.8. Mass spectrum of **Cu-CA4**. Dilution with H₂O/MeOH 1:5.

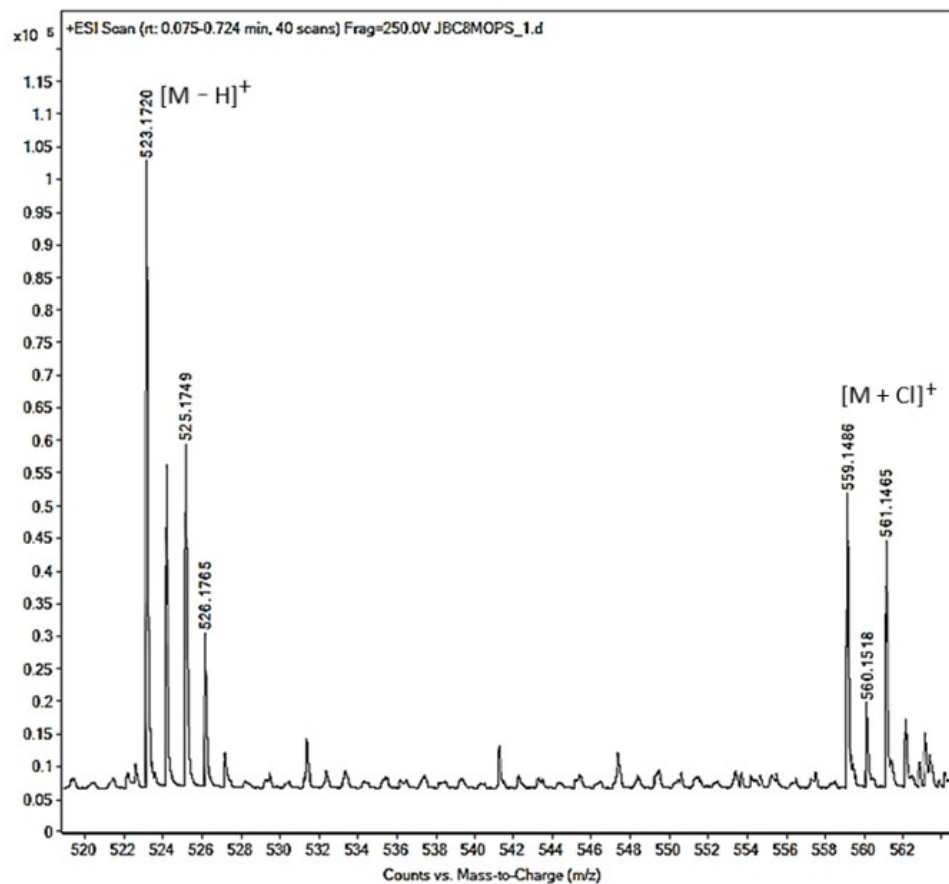


Figure S4.9. Mass spectrum of Cu-CA5. Dilution with H₂O/MeOH 1:5.

CD spectroscopy was applied to evaluate the structural features of Cu(II) complexes. *In situ* complexes were directly prepared in *Hellma* cuvettes (10 mm) by adding Milli-Q® water, MOPS buffer (pH 7.4, 20 mM), tetrapeptides **AA1–AA4** and **CA1–CA5** (1.0 mM), and CuCl₂ (0.8 mM). The wavelength range was set to 250–800 nm, the step size to 1 nm, and the time-per-point to 1 s. The baseline was set with MOPS buffer pH 7.4. CD spectra were taken as triplicates for each complex.

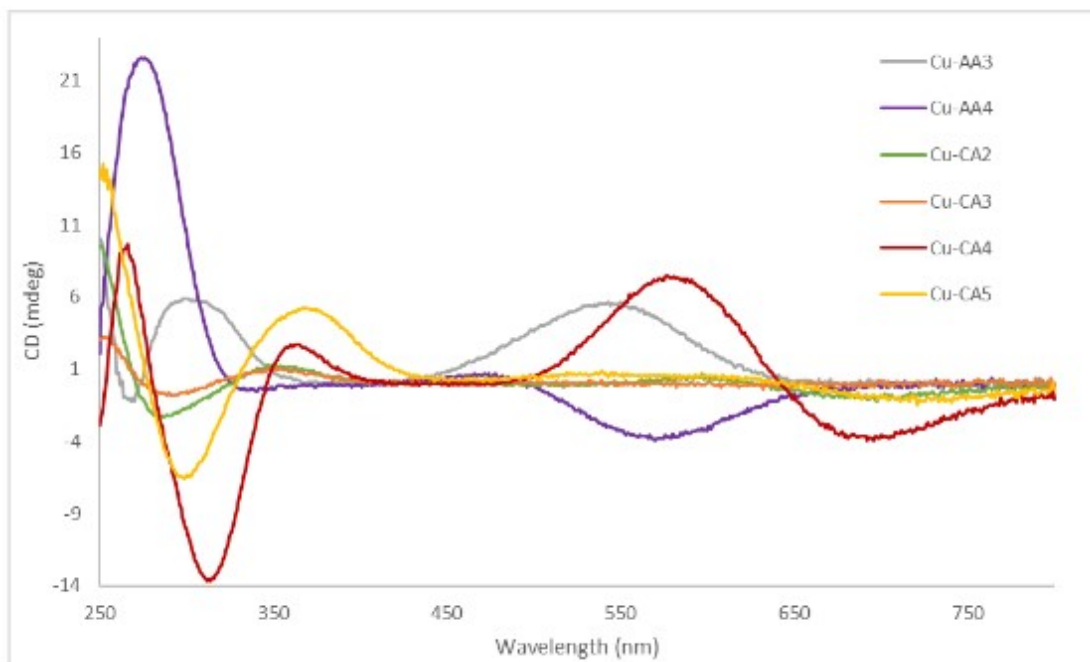


Figure S4.10. CD spectra of Cu(II) complexes **Cu-AA3**, **Cu-AA4** and **Cu-CA2–CA5** in the presence of MOPS buffer (pH 7.4).

In order to determine the stability of the corresponding Cu(I) complexes, peptides **AA1**, **AA2** and **CA1** were titrated to the Cu(I) complex [CuFz₂]³⁻ in a UV/VIS experiment.^{3,10}

K_{app} values were calculated by considering the increase/decrease of the characteristic absorption band of [CuFz₂]³⁻ at 470 nm ($\epsilon = 4320 \text{ M}^{-1} \text{ cm}^{-1}$) during the peptide titration (Figures S4.11-13), the association constant of Fz towards Cu(I) ($\beta = 3.7 \times 10^{11} \text{ M}^{-2}$) and the used concentrations of [CuFz₂]³⁻ (50 μM Cu(I), 105 μM Fz) and peptides (100–500 μM). For each peptide addition (100 μM) a K_{app} value was calculated. All obtained K_{app} values were averaged with the corresponding standard deviation (Table S4.2).¹⁰

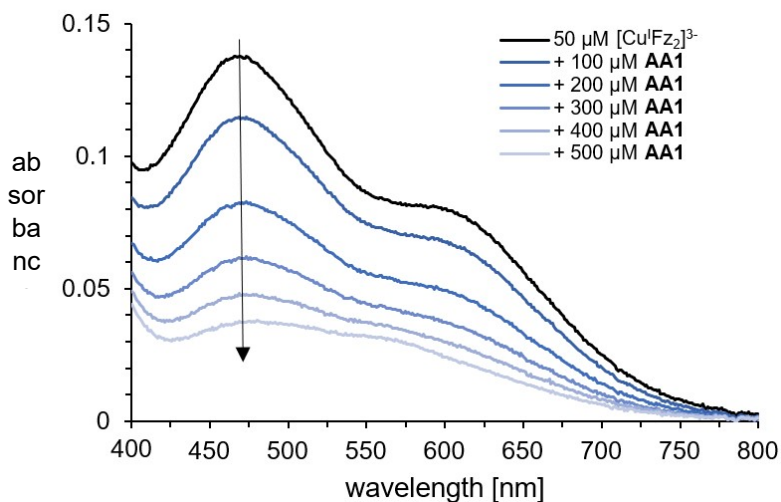


Figure S4.11. UV/VIS spectra of $[\text{CuFz}_2]^{3-}$ (50 μM , Cu(I):Fz ratio = 1:2.1) and successive titration of peptide **AA1** (100 to 500 μM) in HEPES (100 mM, pH 7.4) and 0.05% MeCN. The arrow indicates the decrease of the absorption band at 470 nm characteristic for the $[\text{CuFz}_2]^{3-}$ complex, which is used for calculation of K_{app} value for **AA1** (complex stability constants towards Cu(I)).¹⁰

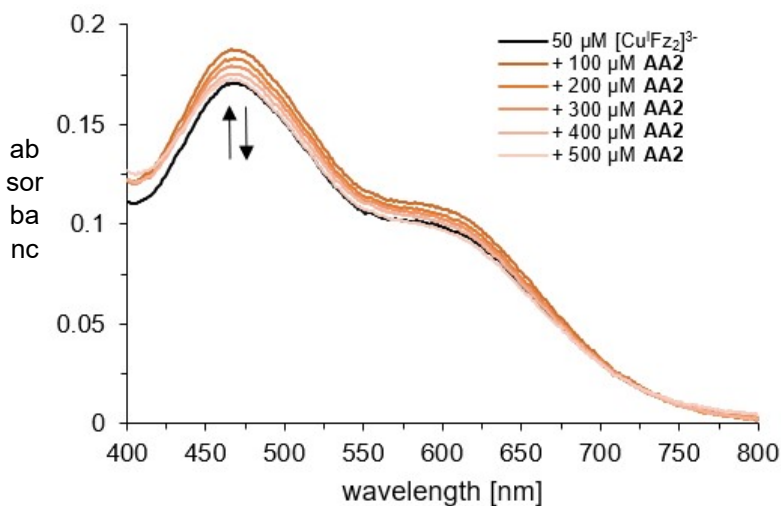


Figure S4.12. UV/VIS spectra of $[\text{CuFz}_2]^{3-}$ (50 μM , Cu(I):Fz ratio = 1:2.1) and successive titration of peptide **AA2** (100 to 500 μM) in HEPES (100 mM, pH 7.4) and 0.05% MeCN. The arrows indicate the increase/decrease of the absorption band at 470 nm characteristic for the $[\text{CuFz}_2]^{3-}$ complex, which is used for calculation of K_{app} value for **AA2** (complex stability constants towards Cu(I)).¹⁰

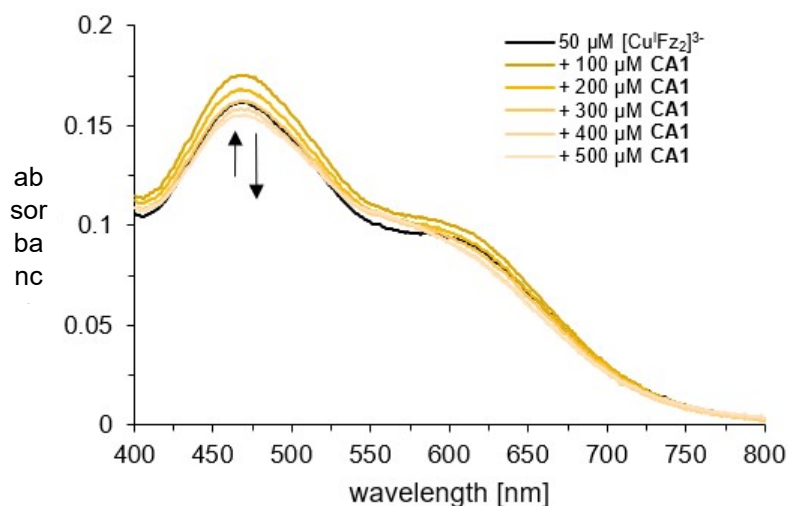


Figure S4.13. UV/VIS spectra of $[\text{Cu}(\text{Fz})_2]^{3-}$ (50 μM , Cu(I):Fz ratio = 1:2.1) and successive titration of peptide **CA1** (100 to 500 μM) in 100 mM HEPES (pH 7.4) and 0.05% MeCN. The arrows indicate the increase/decrease of the absorption band at 470 nm characteristic for the $[\text{Cu}(\text{Fz})_2]^{3-}$ complex, which is used for calculation of the K_{app} value for **CA1** (complex stability constants towards Cu(I)).¹⁰

Table S4.2. Complex stability constants of peptides **AA1**, **AA2** and **CA1** towards Cu(I) (K_{app}) with standard deviation calculated by competition with Fz and the association constant for $[\text{Cu}(\text{Fz})_2]^{3-}$ ($\beta = 3.7 \times 10^{11} \text{ M}^{-2}$).

peptide	chelate rings	K_{app} [10^6 M^{-1}]
AA1	5,6,6	20.60 ± 7.02
AA2	6,6,6	< 0.15
CA1	6,6,6	< 0.41

Note: The slight increase in the absorbance during the first titration step with **AA2** and **CA1** peptide is an indication that this assay might be “at its limit” concerning the range of investigated stability constants. The relatively strong chelator **AA1** directly leads to a decrease of $[\text{Cu}(\text{Fz})_2]^{3-}$ as expected, whereas **AA2** and **CA1** as presumably weaker chelators due their 6,6,6 chelate character show a different behavior: Addition of the latter peptides might lead to a shift of the chemical equilibrium $\text{Cu}^+ + 2 \text{Fz}^{2-} \rightleftharpoons [\text{Cu}(\text{Fz})_2]^{3-}$ towards the right side first, thus leading to higher concentration of $[\text{Cu}(\text{Fz})_2]^{3-}$ (the nominal calculated 50 μM of the complex are present as only about 35 μM when re-calculated from the absorbance value using the literature-reported extinction coefficient¹⁰). We thus suggest that the determined values for **AA2** ($0.15 \times 10^6 \text{ M}^{-1}$) and **CA1** ($0.41 \times 10^6 \text{ M}^{-1}$) are the upper limits for K_{app} , and the stability constants might actually be lower.

Table S4.3 Spin Hamiltonian parameters of copper complexes at 9.4 (X-band) and 34 GHz (Q-band)

Complex	Q-band (50 K)		X-band (77 K)	
	$^{63,65}\text{Cu}$ [A_{xx} , A_{yy} , A_{zz}] /MHz	[g_{xx} , g_{yy} , g_{zz}]	$^{63,65}\text{Cu}$ [A_{xx} , A_{yy} , A_{zz}] /MHz	[g_{xx} , g_{yy} , g_{zz}]
AA1	[30 30 580]	[2.045 2.045 2.196]	[30 70 600]	[2.050 2.070 2.196]
AA2	[30 70 450] *[70 70 550]	[2.065 2.065 2.305] *[2.065 2.065 2.287]	[30 30 550] *[30 70 450]	[2.068 2.068 2.287] *[2.065 2.065 2.305]
AA3	n.a.	n.a.	[40 70 600] $^{14}\text{N}(x2)$: [65 70 4]	[2.065 2.060 2.205]
CA1	[40 40 570] (15° tilted about y axis)	[2.056 2.056 2.269]	[40 40 570]	[2.058 2.058 2.260]
CA5	n.a.	n.a.	[40 40 570] $^{14}\text{N}(x4)$: [48 45 45]	[2.060 2.060 2.260]

* second component

n.a. not available

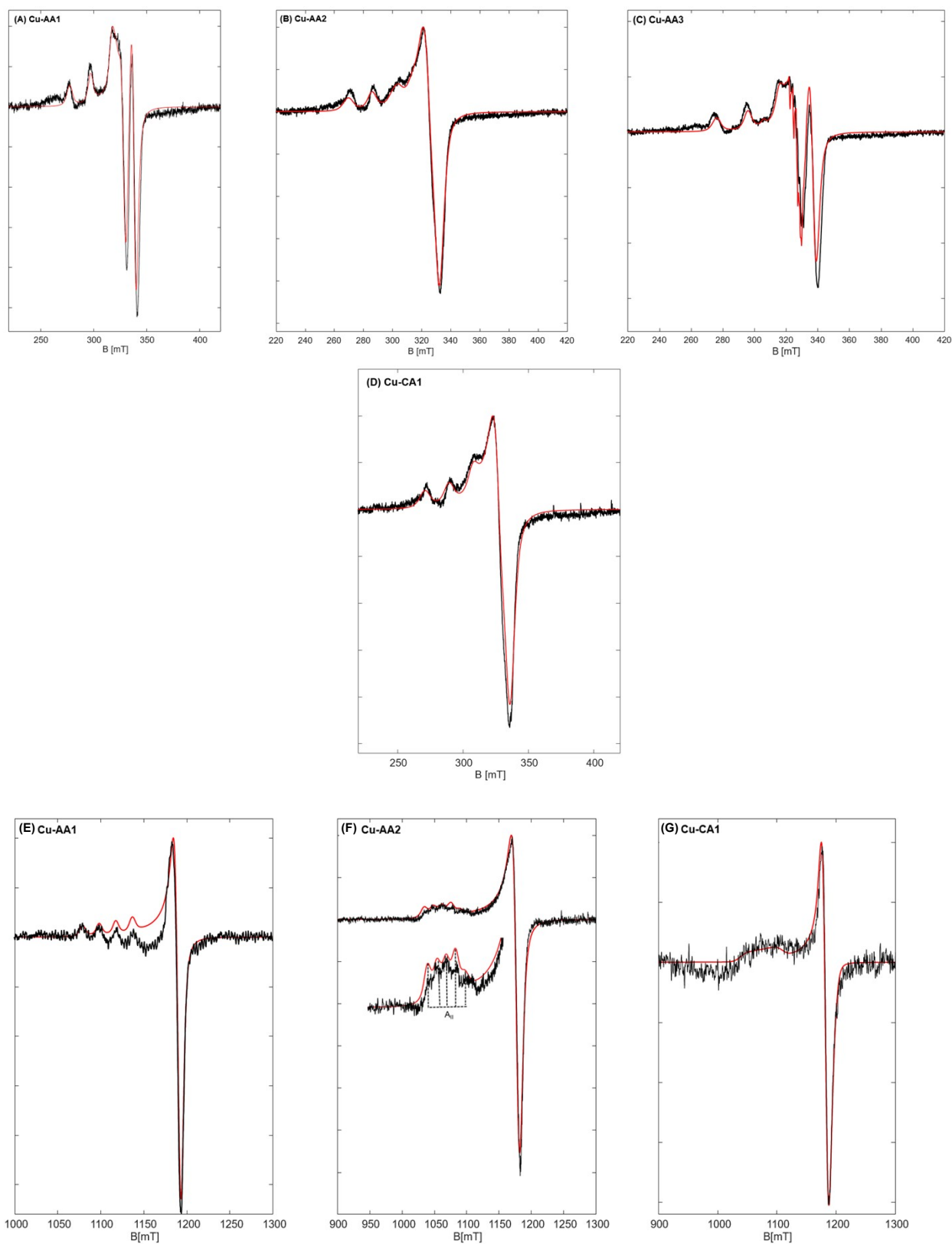


Figure S4.14. EPR spectra (in black) and their simulations (in red) of Cu-AA1 (A), Cu-AA2 (B), Cu-AA3 (C), and Cu-CA1 (D) complexes at 9.4 GHz, 77 K, and of Cu-AA1 (E), Cu-AA2 (F) and Cu-CA1 (G) complexes at 34 GHz, 50 K.

S5 DNA cleavage studies

1% agarose gel electrophoresis in 0.5X TBE buffer containing ethidium bromide (EtBr) 1% (0.2 $\mu\text{g}/\text{mL}$) was employed for the evaluation of the DNA cleavage activity. Solutions included Milli-Q[®] water, MOPS buffer pH 7.4 (50 mM), **Cu-AA1–Cu-AA4**, **Cu-CA1–Cu-CA5** complexes and CuCl_2 at concentrations 10 μM , 20 μM , 30 μM , 35 μM , and 40 μM , ascorbate (1 mM), and plasmid DNA pBR322 (0.025 $\mu\text{g}/\mu\text{L}$, 4361 bp from *Carl Roth*). Solutions were incubated for 1 h at 37 $^\circ\text{C}$, 500 rpm. After incubation, 1.5 μL of bromophenol blue and saccharose in water were added to each sample and the total volume was loaded into the pockets. Separation of DNA was carried out for 2 h at 40 V using a *Rotiphorese[®] PROfessional I* electrophoresis unit from *Carl Roth*. Supercoiled (Form I), nicked (Form II) and linear (Form III) DNA bands were visualized on a *Bio-Rad GelDoc EZ Imager*. Data were analyzed with *Bio-Rad's Image Lab Software* (Version 3.0). A correction factor of 1.22 was used for the supercoiled DNA band due to the reduced ability of EtBr to intercalate into this form, relative to form II and III.¹¹ In all cases, experiments were performed at least in triplicate.

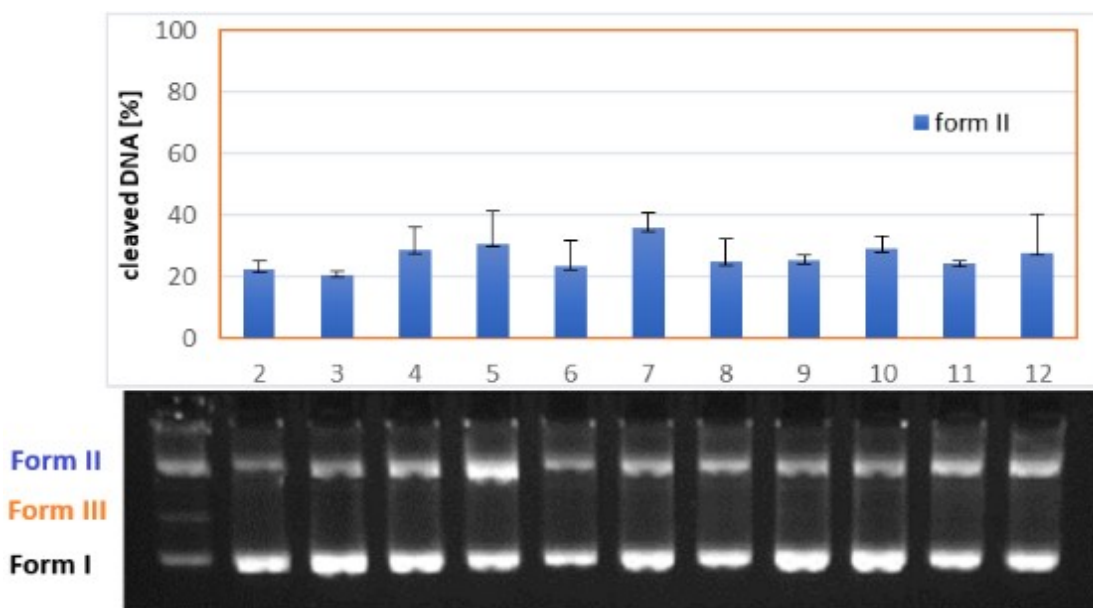


Figure S5.1. DNA cleavage activity of complexes **Cu-AA1–Cu-AA4**, **Cu-CA1–Cu-CA5** and CuCl_2 at a concentration of 10 μM . Lane 1: DNA ladder (forms I, II and III), lane 2: DNA reference, lanes 3-12: **Cu-AA1–Cu-AA4**, **Cu-CA1–Cu-CA5** and CuCl_2 .

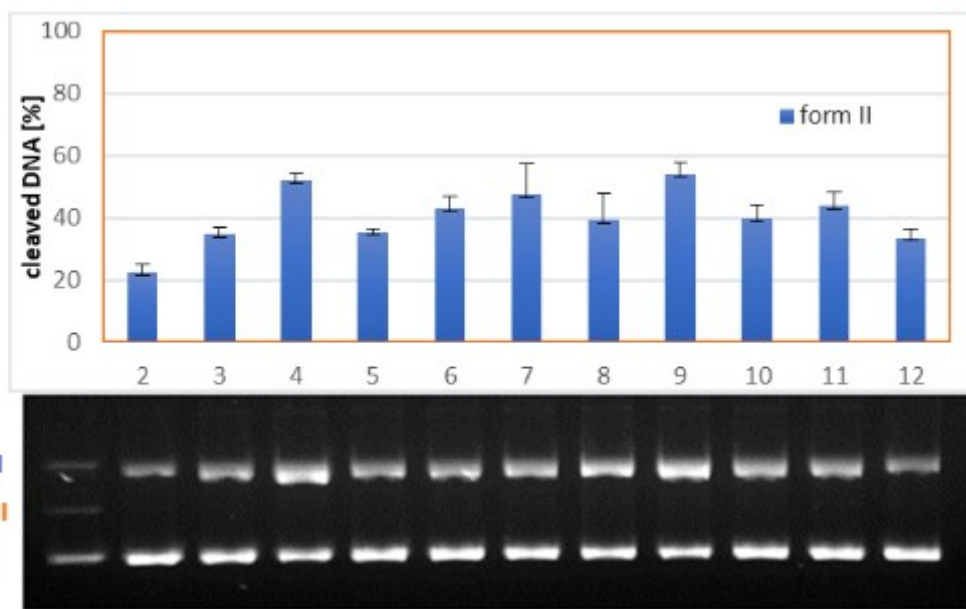


Figure S5.2. DNA cleavage activity of complexes **Cu-AA1-Cu-AA4**, **Cu-CA1-Cu-CA5** and **CuCl₂** at a concentration of 20 μM. Lane 1: DNA ladder (forms I, II and III), lane 2: DNA reference, lanes 3-12: **Cu-AA1-Cu-AA4**, **Cu-CA1-Cu-CA5** and **CuCl₂**.

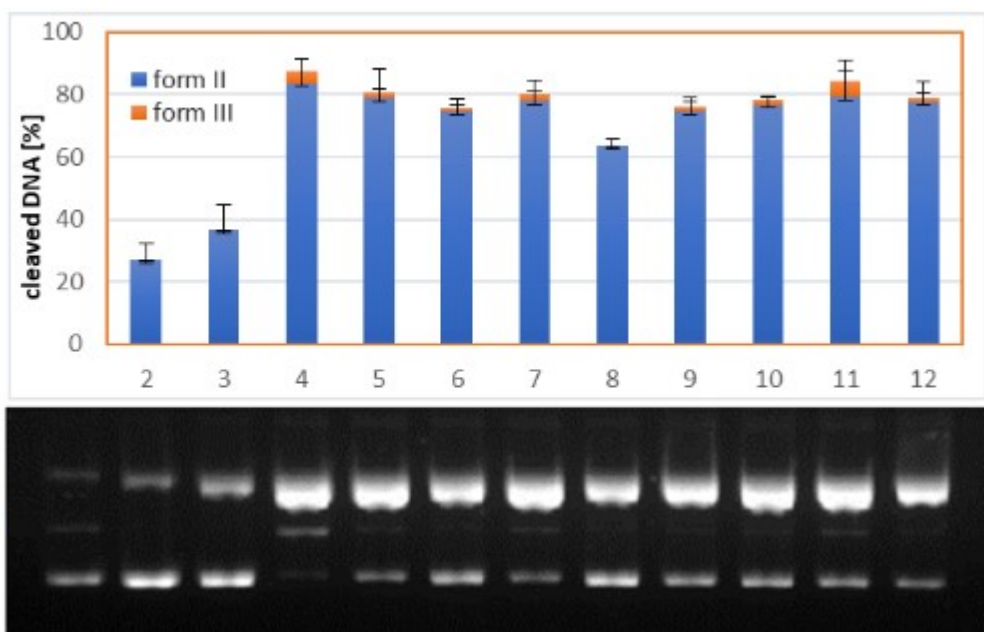


Figure S5.3. DNA cleavage activity of complexes **Cu-AA1-Cu-AA4**, **Cu-CA1-Cu-CA5** and **CuCl₂** at a concentration of 30 μM. Lane 1: DNA ladder (forms I, II and III), lane 2: DNA reference, lanes 3-12: **Cu-AA1-Cu-AA4**, **Cu-CA1-Cu-CA5** and **CuCl₂**.

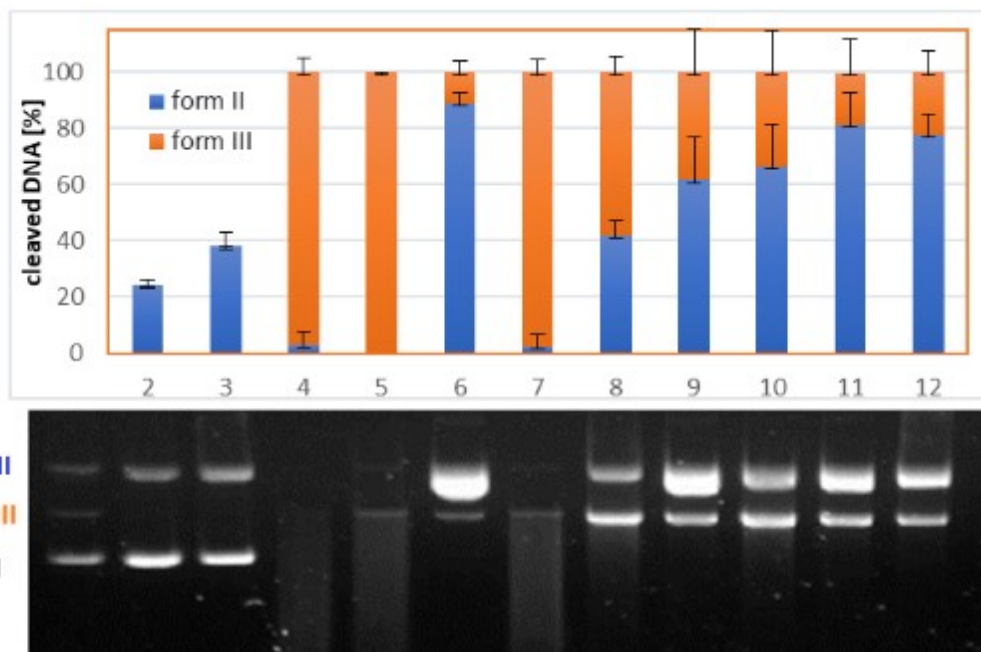


Figure S5.4. DNA cleavage activity of complexes **Cu-AA1-Cu-AA4**, **Cu-CA1-Cu-CA5** and CuCl_2 at a concentration of $40 \mu\text{M}$. Lane 1: DNA ladder (forms I, II and III), lane 2: DNA reference, lanes 3-12: **Cu-AA1-Cu-AA4**, **Cu-CA1-Cu-CA5** and CuCl_2 .

Complexes **Cu-AA2** and **Cu-CA1** were employed to evaluate ROS generation following the same incubation conditions previously described and in the presence of one of the ROS scavengers: DMSO (400 mM), NaN₃ (10 mM), pyruvate (2.5 mM) with a concentration of 100 mM MOPS to keep the pH value constant at 7.4, and superoxide dismutase (SOD, 625 U/mL). In all cases, experiments were performed at least in triplicate.

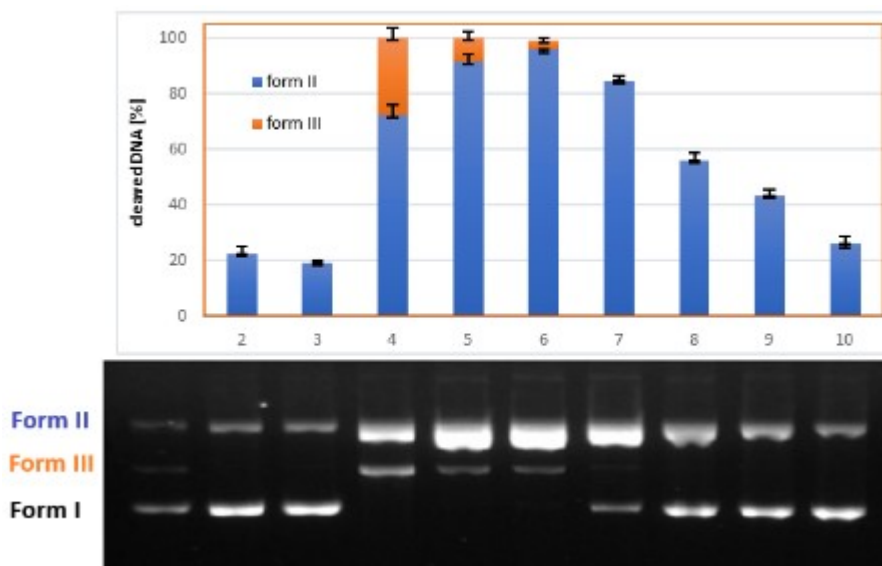


Figure S5.5. Reactive oxygen species (ROS) assay by gel electrophoresis for complex **Cu-AA2** at a concentration of 35 μ M. Lane 1: DNA ladder (forms I, II and III), lane 2: DNA reference, lane 3: complex without asCH⁺, lane 4–10: complex with asCH⁺ and the following scavengers: lane 4: none, lane 5: DMSO (400 mM), lane 6: NaN₃ (10 mM), lane 7: pyruvate (2.5 mM), lane 8: SOD (625 U/mL), lane 9: pyruvate (2.5 mM) and SOD (625 U/mL), lane 10: DMSO (400 mM), NaN₃ (10 mM), pyruvate (2.5 mM), SOD (625 U/mL).

S6 ROS detection by fluorescence spectroscopy

Complexes **Cu-AA2** and **Cu-CA1** were chosen in order to evaluate the formation of $\cdot\text{OH}$ and H_2O_2 by changes in the fluorescence emission spectra of TPA and PBSF, respectively. Solutions of the corresponding Cu(II) complex (35 μM) were prepared in the presence of MOPS buffer (50 mM, pH 7.4), ascorbate (ascH^- , 1 mM), fluorogenic dyes TPA (0.5 mM) or PBSF (25 μM) and the corresponding scavengers DMSO (400 mM) for $\cdot\text{OH}$ or pyruvate (2.5 mM) for H_2O_2 . Samples were prepared following the order: Milli-Q[®] water, buffer, dye, ROS scavenger, Cu(II) complex, ascorbate, and were incubated at 37 °C, 500 rpm for 1 h and 2.5 h, respectively. Fluorescence spectra were recorded immediately after incubation and were collected at room temperature and in the range of 350–550 nm for TPA-containing samples ($\lambda_{\text{ex}} = 320 \text{ nm}$), and 490–580 nm, for PBSF-containing samples ($\lambda_{\text{ex}} = 485 \text{ nm}$). The scan rate was 120 nm/min, the photomultiplier voltage adjusted to 900 V and 750 V using TPA and PBSF, respectively.

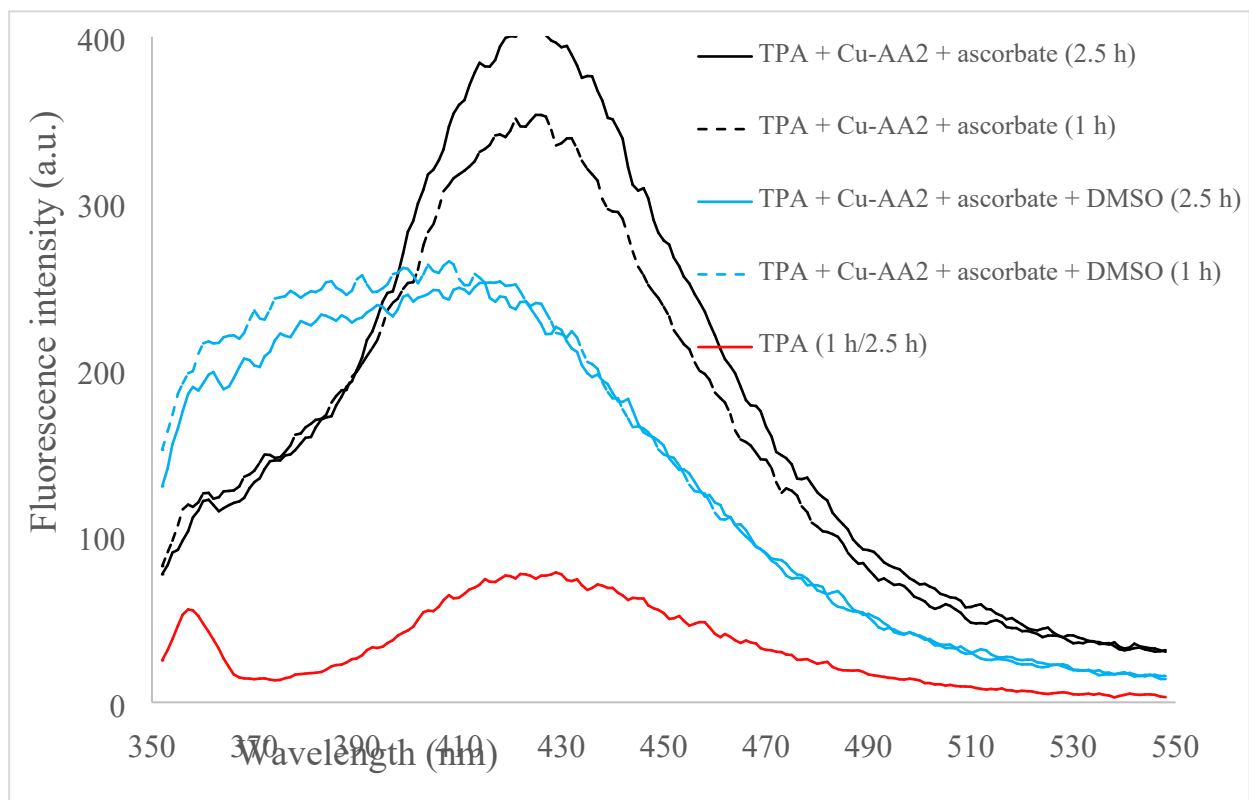


Figure S6.1. Fluorescence emission recorded after incubation of TPA (0.5 mM, $\lambda_{\text{ex}} = 320 \text{ nm}$, $\lambda_{\text{em}} = 428 \text{ nm}$) with complex **Cu-AA2** (35 μM) in the presence of MOPS buffer (50 mM, pH 7.4), ascH^- (1 mM) and the scavenging agent DMSO (400 mM) at 37 °C for the indicated time.

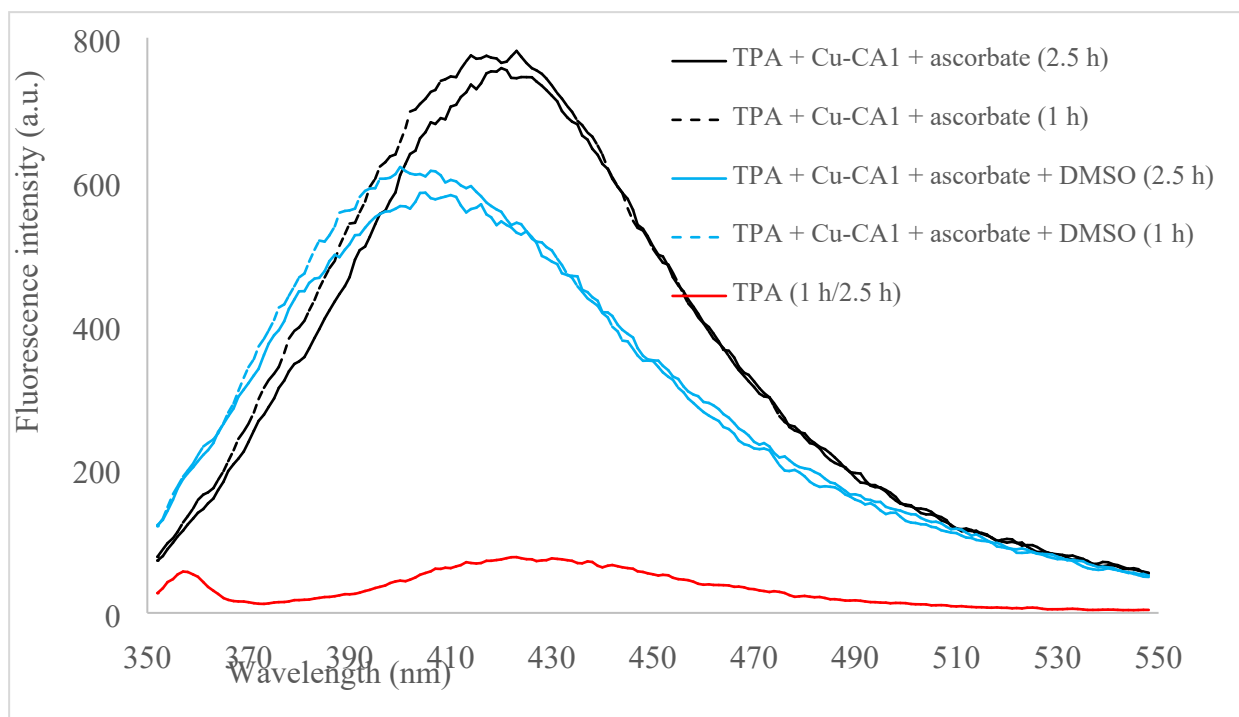


Figure S6.2. Fluorescence emission recorded after incubation of TPA (0.5 mM, $\lambda_{\text{ex}} = 320$ nm, $\lambda_{\text{em}} = 428$ nm) with complex **Cu-CA1** (35 μM) in the presence of MOPS buffer (50 mM, pH 7.4), ascH^- (1 mM) and the scavenging agent DMSO (400 mM) at 37 $^\circ\text{C}$ for the indicated time.

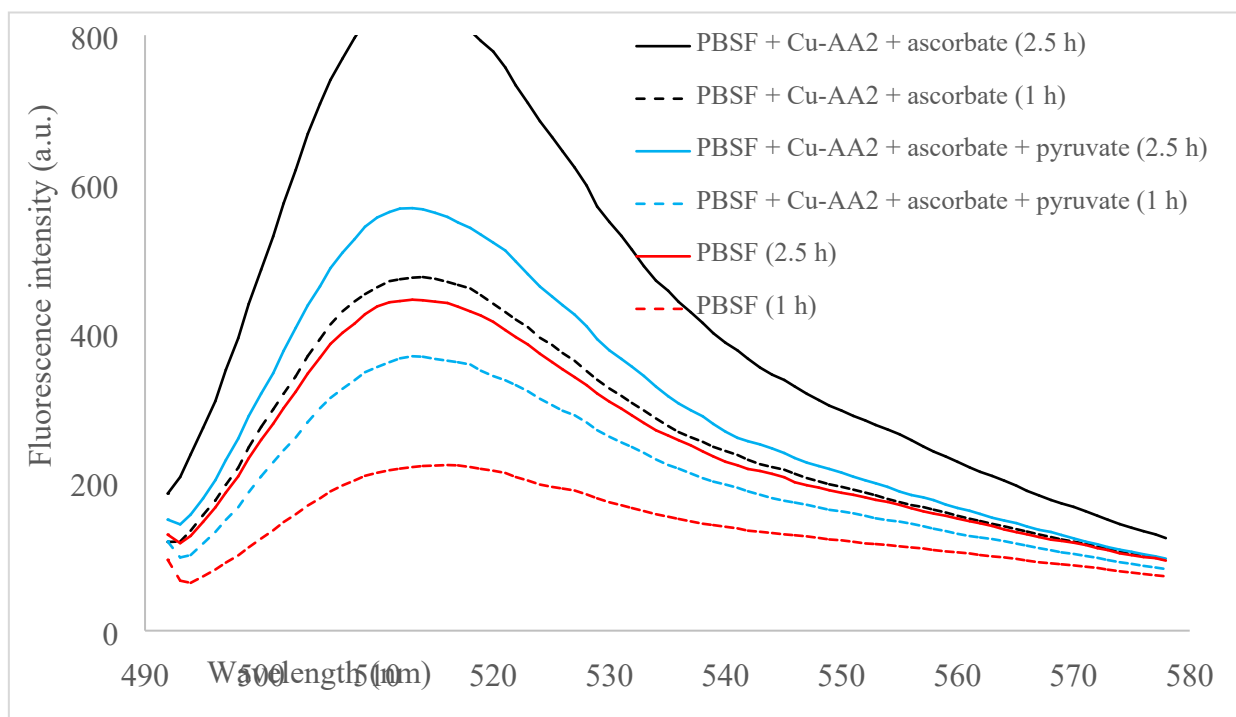


Figure S6.3. Fluorescence emission recorded after incubation of PBSF (25 μM , $\lambda_{\text{ex}} = 485$ nm, $\lambda_{\text{em}} = 513$ nm) with complex **Cu-AA2** (35 μM) in the presence of MOPS buffer (50 mM, pH 7.4), ascH^- (1 mM), and the scavenging agent pyruvate (2.5 mM) at 37 $^\circ\text{C}$ for the indicated time.

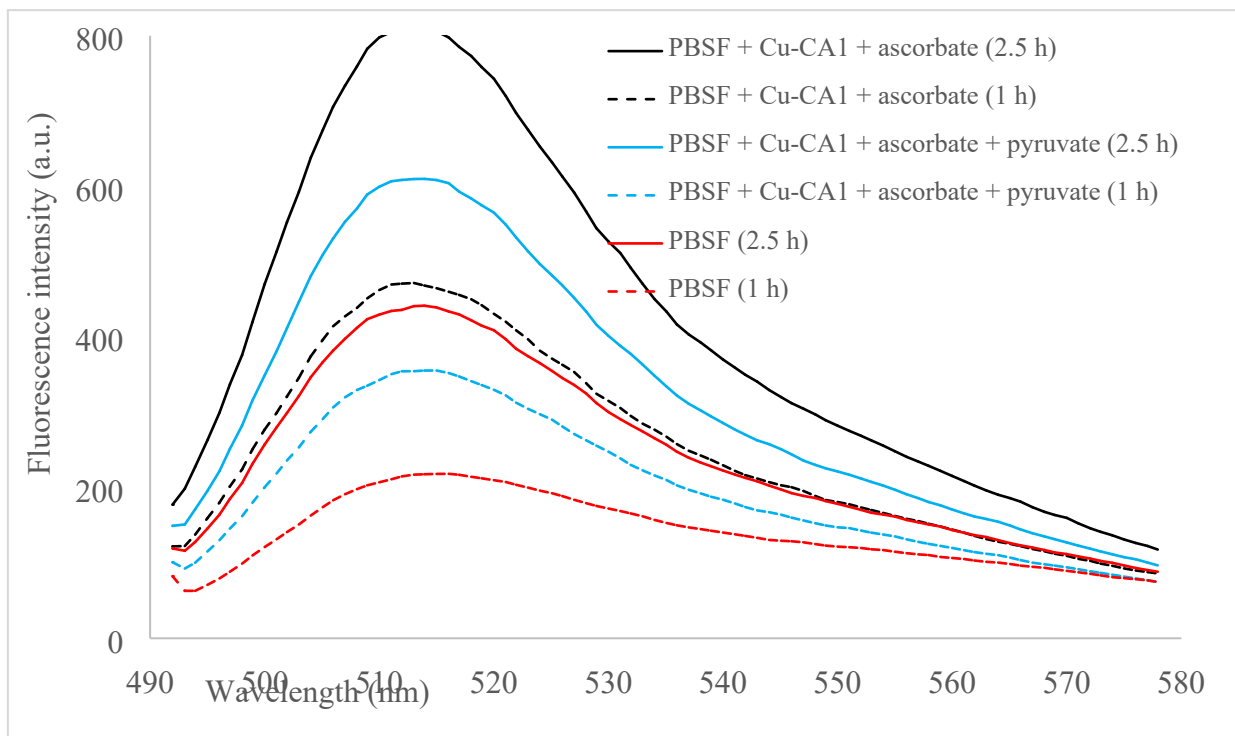


Figure S6.4. Fluorescence emission recorded after incubation of PBSF (25 μM , $\lambda_{\text{ex}} = 485 \text{ nm}$, $\lambda_{\text{em}} = 513 \text{ nm}$) with complex **Cu-CA1** (35 μM) in the presence of MOPS buffer (50 mM, pH 7.4), ascorbate (1 mM), and the scavenging agent pyruvate (2.5 mM) at 37 $^{\circ}\text{C}$ for the indicated time.

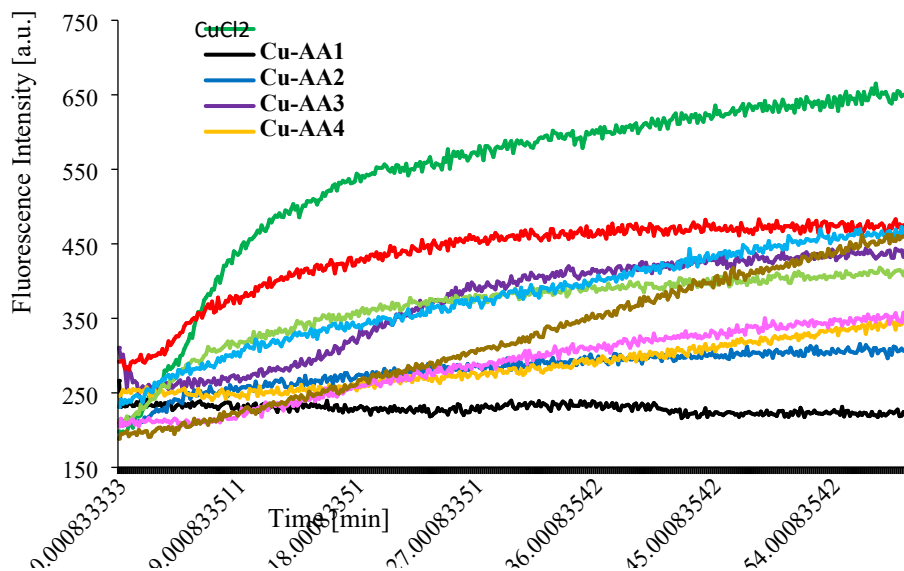


Figure S6.7. Kinetics of H_2O_2 evolution: Fluorescence emission based on fluorescein formation by PBSF perhydrolysis (25 μM , $\lambda_{\text{ex}} = 485 \text{ nm}$, $\lambda_{\text{em}} = 513 \text{ nm}$) with complexes **Cu-AA1–Cu-AA4**, **Cu-CA1–Cu-CA5** and CuCl_2 (35 μM) in the presence of ascorbate (1 mM) and MOPS buffer (50 mM, pH 7.4) at room temperature.

S7 DNA interaction studies

UV/VIS spectroscopy

The melting temperature of calf thymus DNA (CT-DNA, 50 μM) in the presence of MOPS buffer (50 mM, pH 7.4) and *in situ* prepared Cu(II)-peptide complexes and CuCl_2 (2.5 μM) was determined by UV/VIS spectroscopy at 260 nm. Melting curves were collected in the range of 65 and 90 $^\circ\text{C}$ with a heating rate of 0.5 $^\circ\text{C}/\text{min}$. Solutions were prepared in Hellma cuvettes following the order: Milli-Q[®] water, MOPS buffer, CT-DNA, complexes **Cu-AA1–Cu-AA4**, **Cu-CA1–Cu-CA5** and CuCl_2 in solution. Melting curves are shown as the average of at least two experiments. Normalization of the absorbance was applied for better visualization and determination of the melting temperature at the value 0.5.

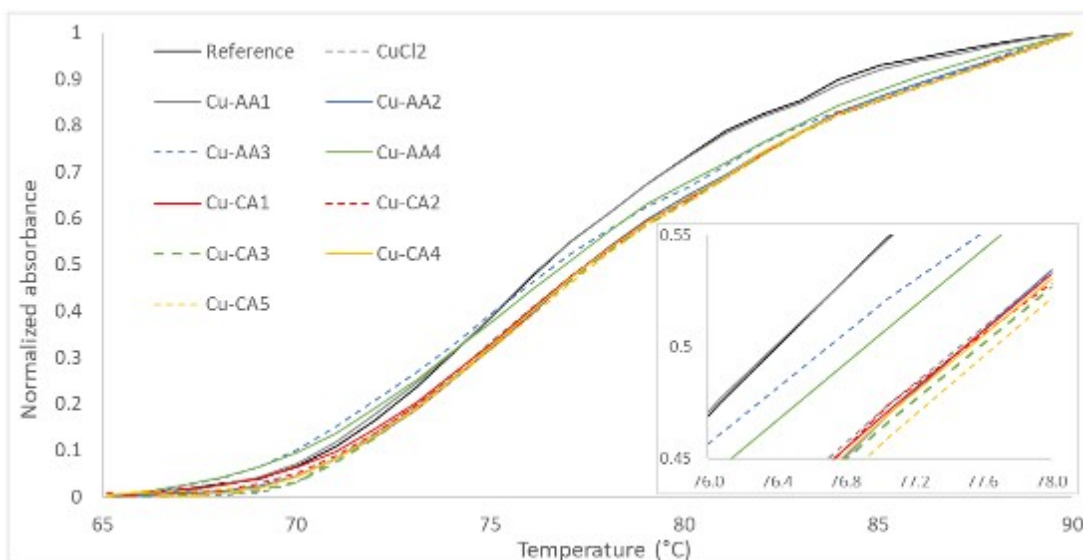


Figure S7.1. Normalized melting temperatures of CT-DNA in the presence of complexes **Cu-AA1–Cu-AA4**, **Cu-CA1–Cu-CA5** and CuCl_2 (2.5 μM)

Table S7.1. Melting temperature (T_m) of CT-DNA in the presence of Cu(II) complexes.

Compound	T_m ($^\circ\text{C}$)	ΔT_m ($^\circ\text{C}$)
Reference	76.4	–
CuCl_2	77.4	1.0
Cu-AA1	76.4	0
Cu-AA2	77.5	1.1
Cu-AA3	76.7	0.3
Cu-AA4	76.9	0.5
Cu-CA1	77.5	1.1
Cu-CA2	77.5	1.1
Cu-CA3	77.6	1.2
Cu-CA4	77.5	1.1
Cu-CA5	77.7	1.3

CD spectroscopy

Binding interactions were additionally analyzed by circular dichroism spectroscopy. CD spectra of CT-DNA (100 μM) with increasing concentrations of the Cu(II) complexes or CuCl_2 in MOPS buffer (50 mM, pH 7.4) were recorded in the range of 220 nm to 320 nm with a measuring velocity of 100 nm/min and a data point interval of 0.1 nm. Solutions were prepared in Hellma cuvettes and *in situ* prepared complexes **Cu-AA1–Cu-AA4**, **Cu-CA1–Cu-CA5** and CuCl_2 were added stepwise, starting from 10 μM up to 60 μM (40 μM for CuCl_2).

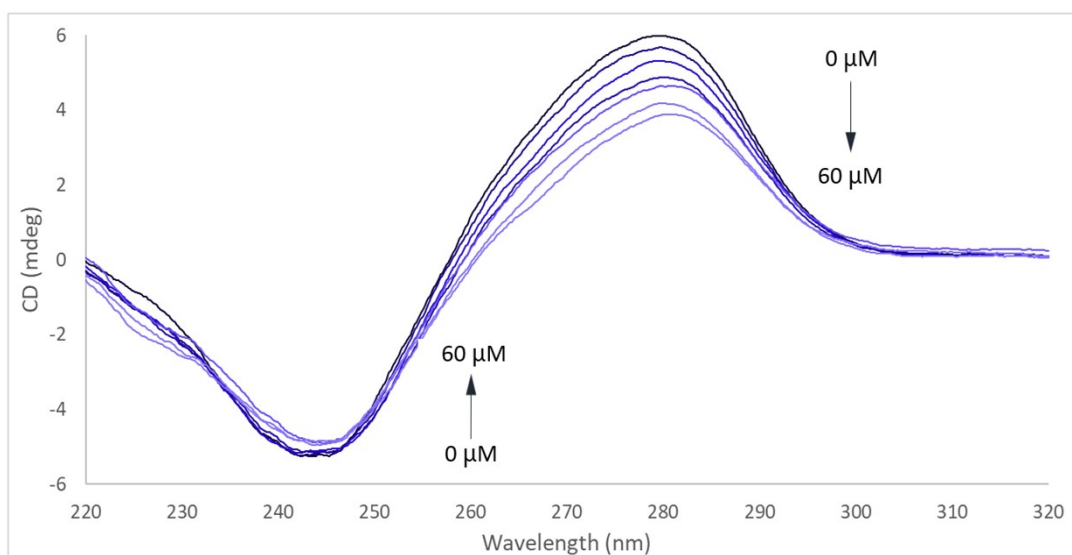


Figure S7.2. CD spectrum of CT-DNA (100 μM) in MOPS buffer (50 mM, pH 7.4) with increasing amount of complex **Cu-AA2** (0 μM to 60 μM).

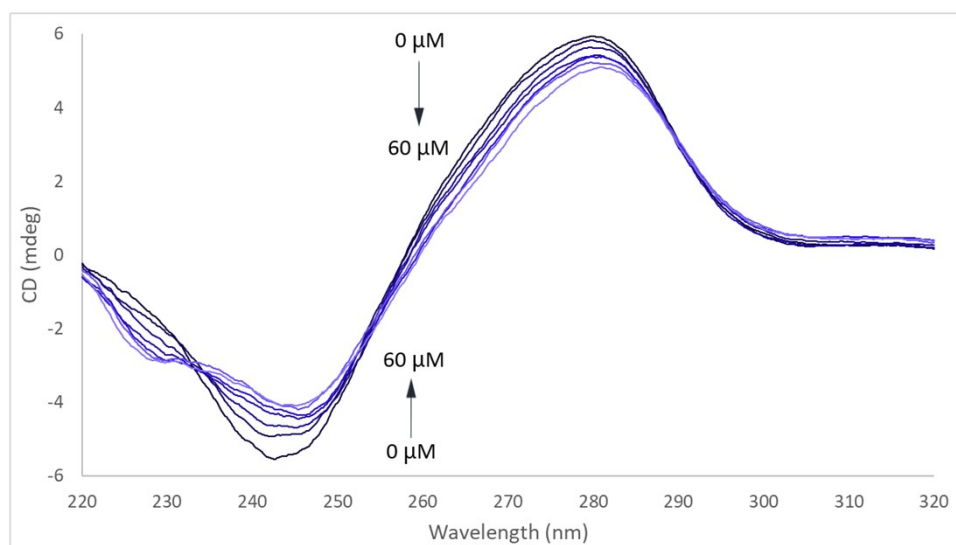


Figure S7.3. CD spectrum of CT-DNA (100 μM) in MOPS buffer (50 mM, pH 7.4) with complex **Cu-AA3** (0 μM to 60 μM).

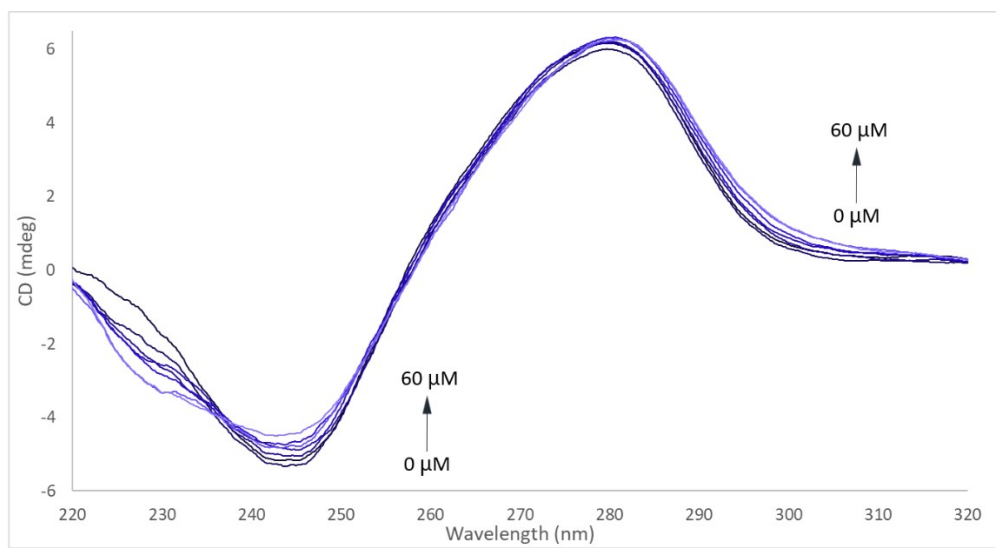


Figure S7.4. CD spectrum of CT-DNA (100 μM) in MOPS buffer (50 mM, pH 7.4) with complex **Cu-AA4** (0 μM to 60 μM).

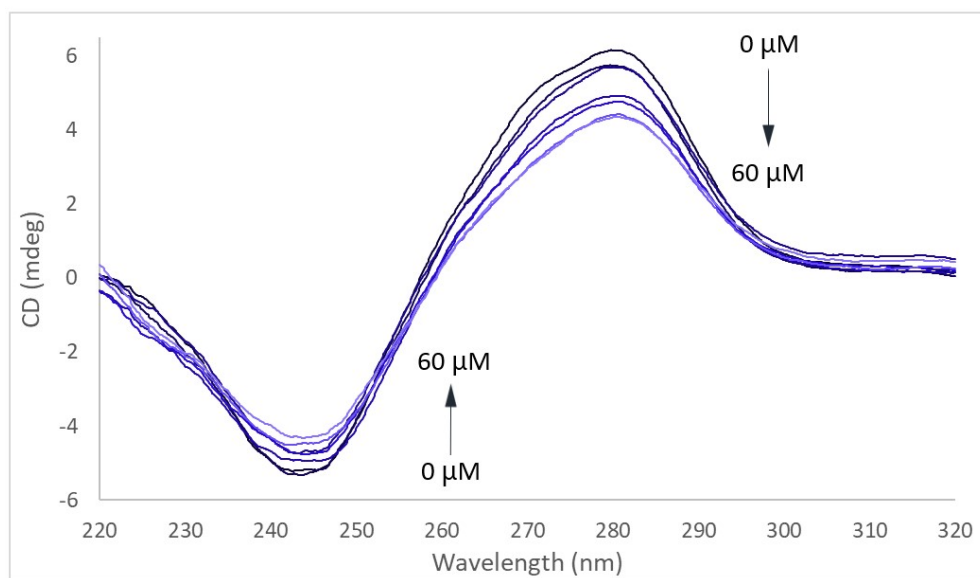


Figure S7.5. CD spectrum of CT-DNA (100 μM) in MOPS buffer (50 mM, pH 7.4) with complex **Cu-CA2** (0 μM to 60 μM).

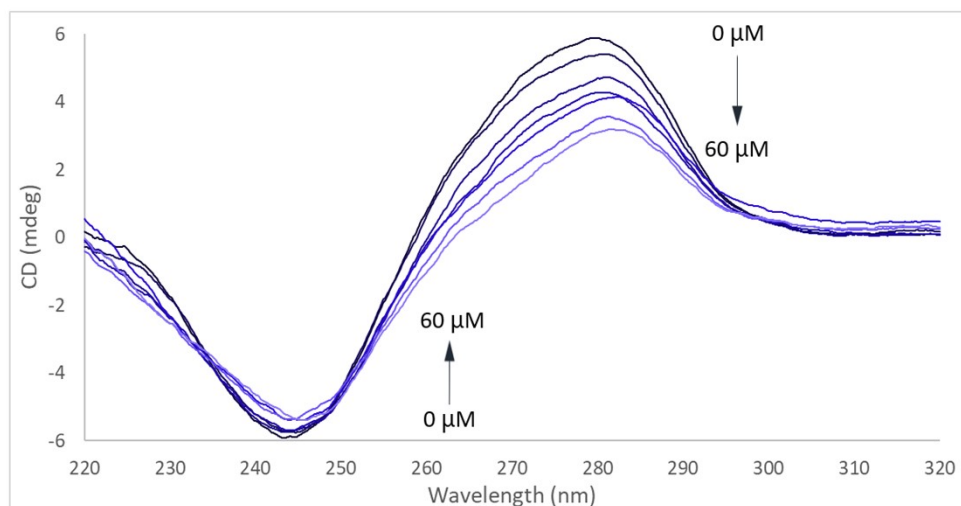


Figure S7.6. CD spectrum of CT-DNA (100 μM) in MOPS buffer (50 mM, pH 7.4) with complex **Cu-CA3** (0 μM to 60 μM).

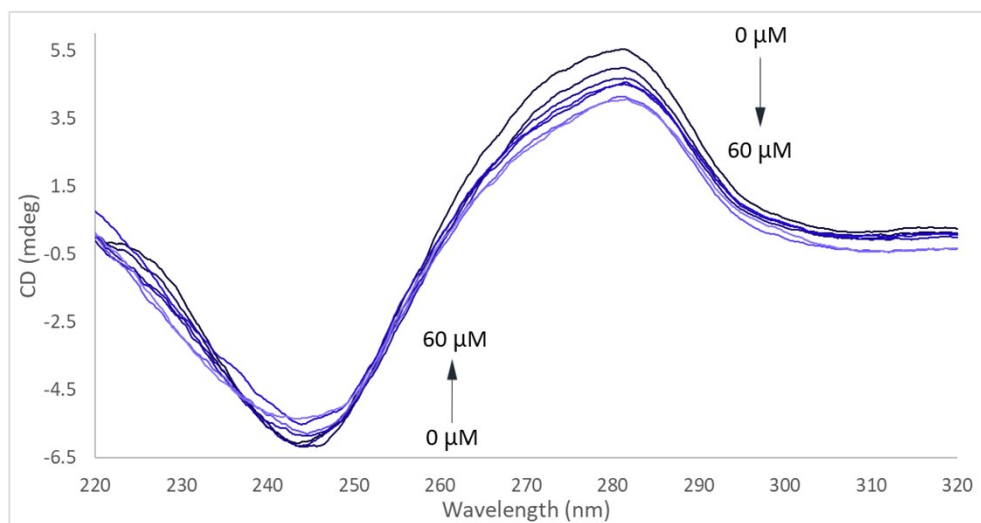


Figure S7.7. CD spectrum of CT-DNA (100 μM) in MOPS buffer (50 mM, pH 7.4) with complex **Cu-CA4** (0 μM to 60 μM).

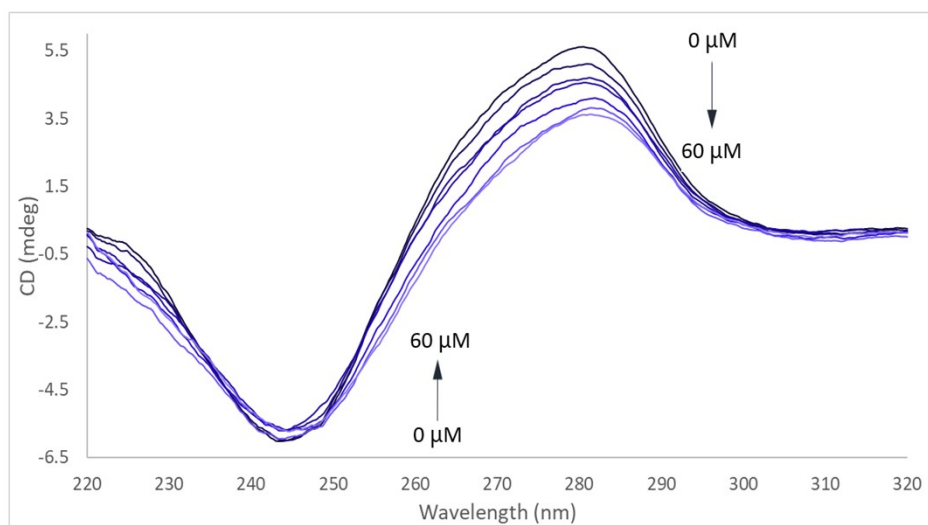


Figure S7.8. CD spectrum of CT-DNA (100 μM) in MOPS buffer (50 mM, pH 7.4) with complex Cu-CA5 (0 μM to 60 μM).

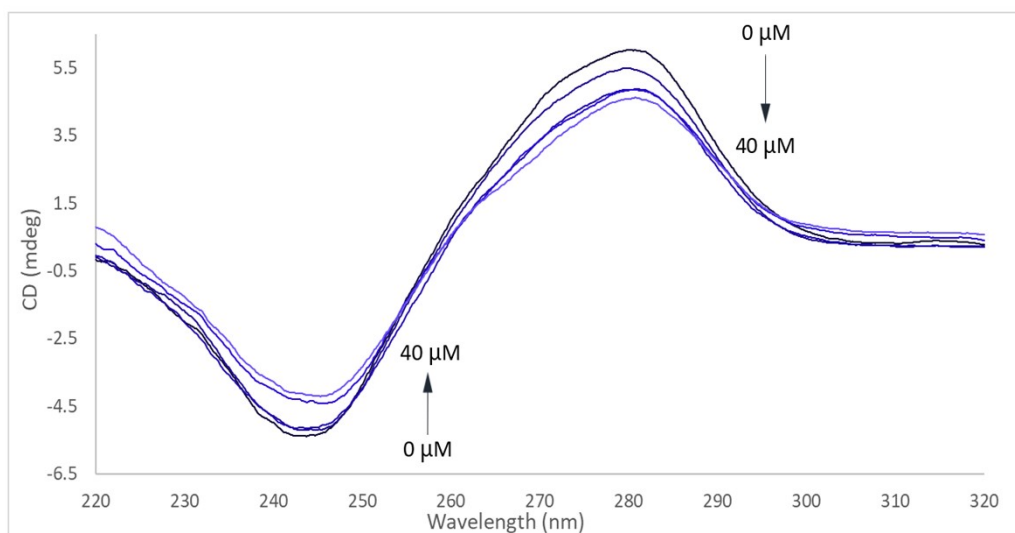


Figure S7.9. CD spectrum of CT-DNA (100 μM) in MOPS buffer (50 mM, pH 7.4) with CuCl_2 from (0 μM to 40 μM).

S8 Cyclic voltammetry

Cyclic voltammetry experiments were conducted following conditions previously described in the literature,¹² but considering the Ag pseudoreference electrode used in this experiment (*cf.* S1). Aqueous solutions of Cu(II) complexes with a concentration of 0.5 mM were prepared. Voltammograms were recorded using KNO₃/HNO₃ with a concentration of 96 mM/4 mM as the electrolyte solution. The pH was measured before adding the complex to the electrolyte solution to give an initial value around 6–7. Cu(II) complexes were prepared by mixing separately peptides and CuCl₂ solutions and subsequently adding them to the electrolyte solutions. pH values were taken again and were adjusted with KOH and HNO₃ to 7.4 to finally record the voltammograms. In the case of buffered solutions, aqueous solutions were prepared by mixing tetrapeptides and CuCl₂ (ratio 1:1.1 CuCl₂/peptides) to reach a concentration of 0.5 mM in the presence of MOPS buffer (5-fold excess, pH 7.4). Cu(II) complex solutions were then added to the electrolyte solution of KCl (100 mM) to finally record the voltammograms.

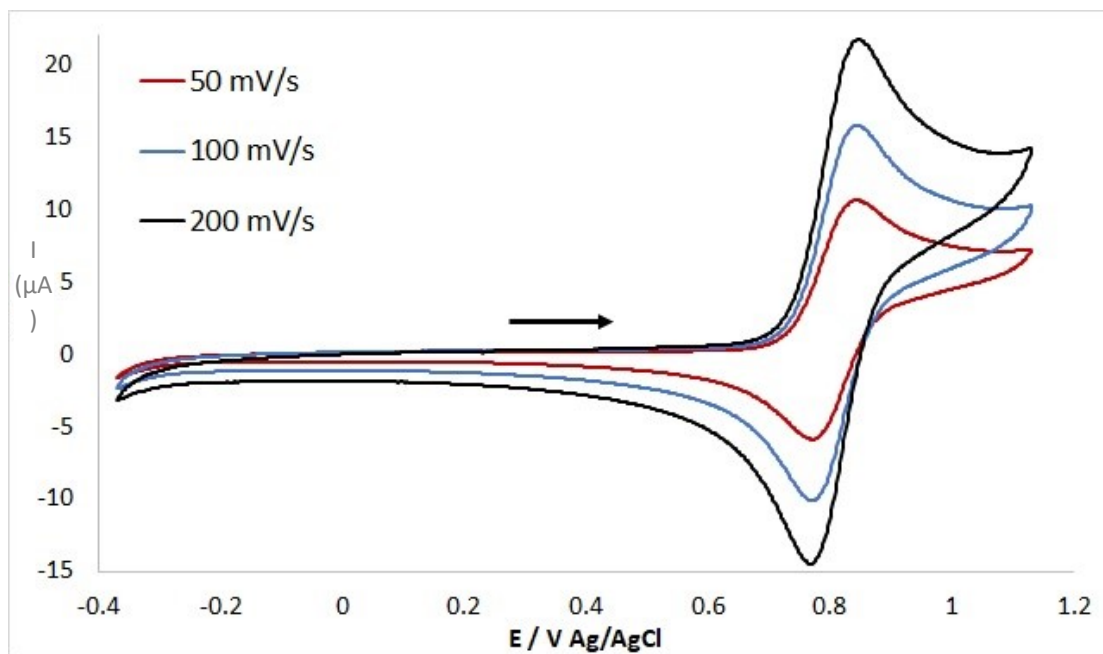


Figure S8.1a. Cyclic voltammogram of complex **Cu-AA1** (0.5 mM) with $\text{KNO}_3/\text{HNO}_3$ as electrolyte solution (96/4 mM) at pH 7.4. The arrow indicates the starting point and direction of the potential scanning (anodic direction).

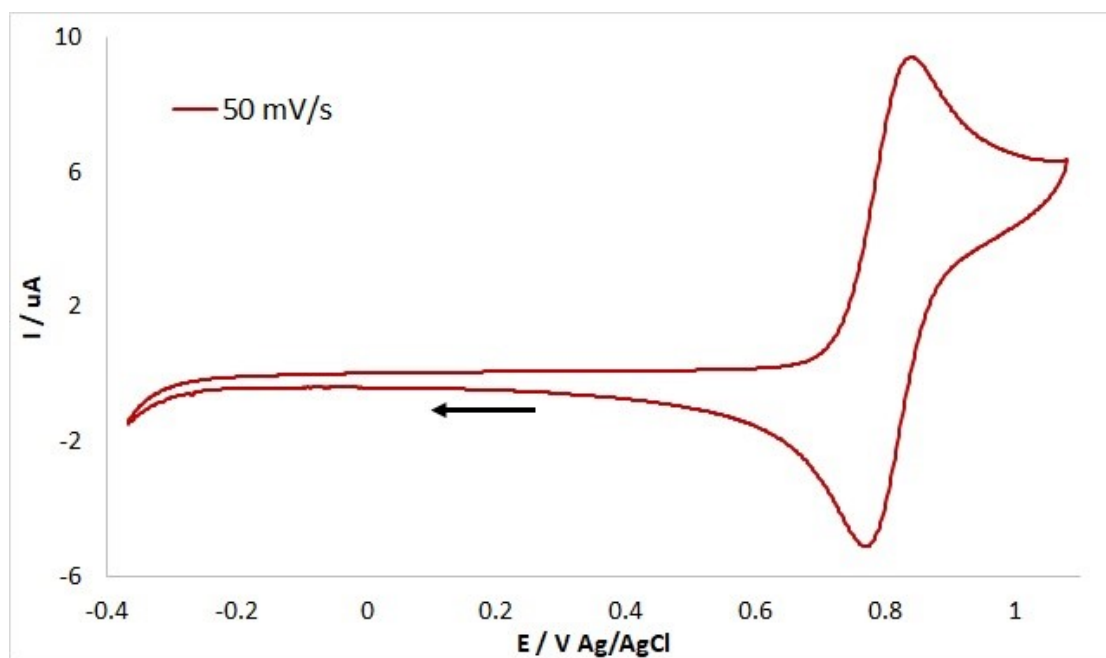


Figure S8.1b. Cyclic voltammogram of complex **Cu-AA1** (0.5 mM) with $\text{KNO}_3/\text{HNO}_3$ as electrolyte solution (96/4 mM) at pH 7.4. The arrow indicates the starting point and direction of the potential scanning (cathodic direction).

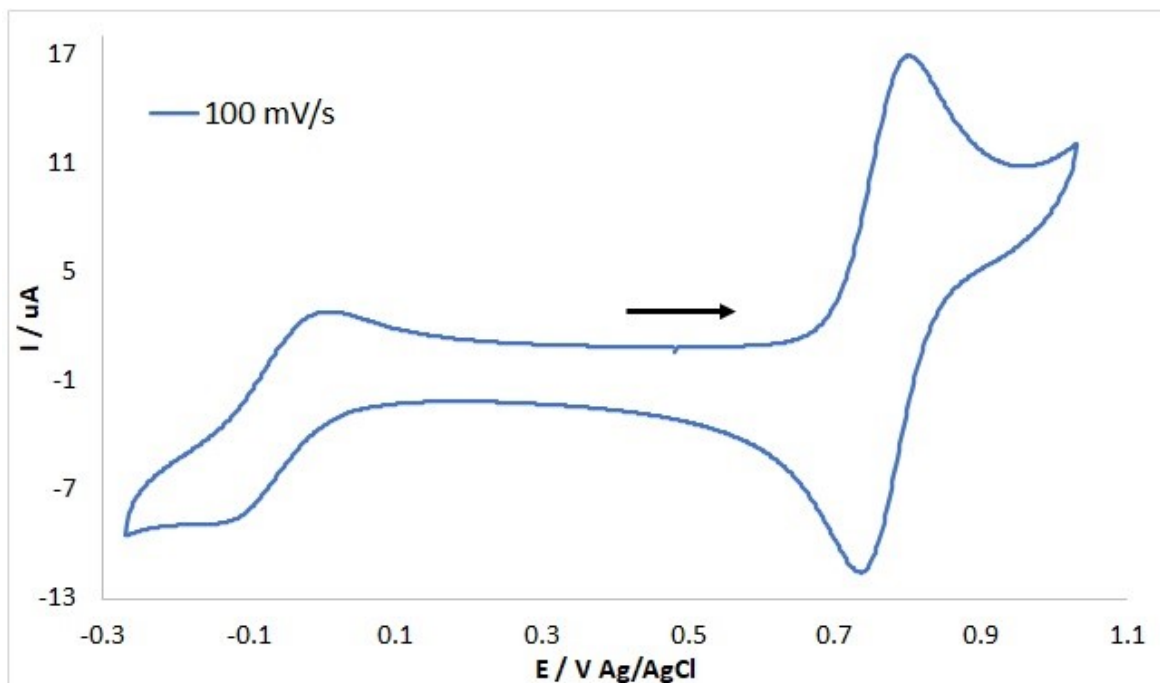


Figure S8.1c. Cyclic voltammogram of complex **Cu-AA1** (0.5 mM) with KCl as electrolyte solution (100 mM) in the presence of MOPS (pH 7.4, 5-fold excess). The arrow indicates the starting point and direction of the potential scanning (anodic direction).

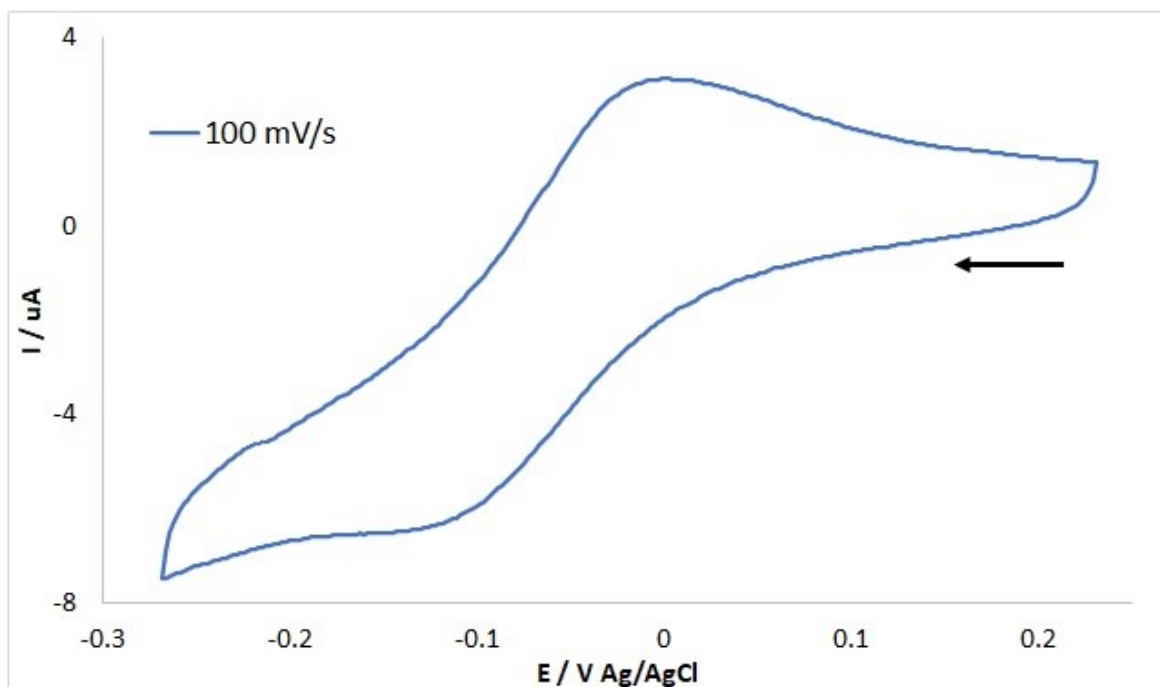


Figure S8.1d. Cyclic voltammogram of complex **Cu-AA1** (0.5 mM) with KCl as electrolyte solution (100 mM) in the presence of MOPS (pH 7.4, 5-fold excess). The arrow indicates the starting point and direction of the potential scanning (cathodic direction).

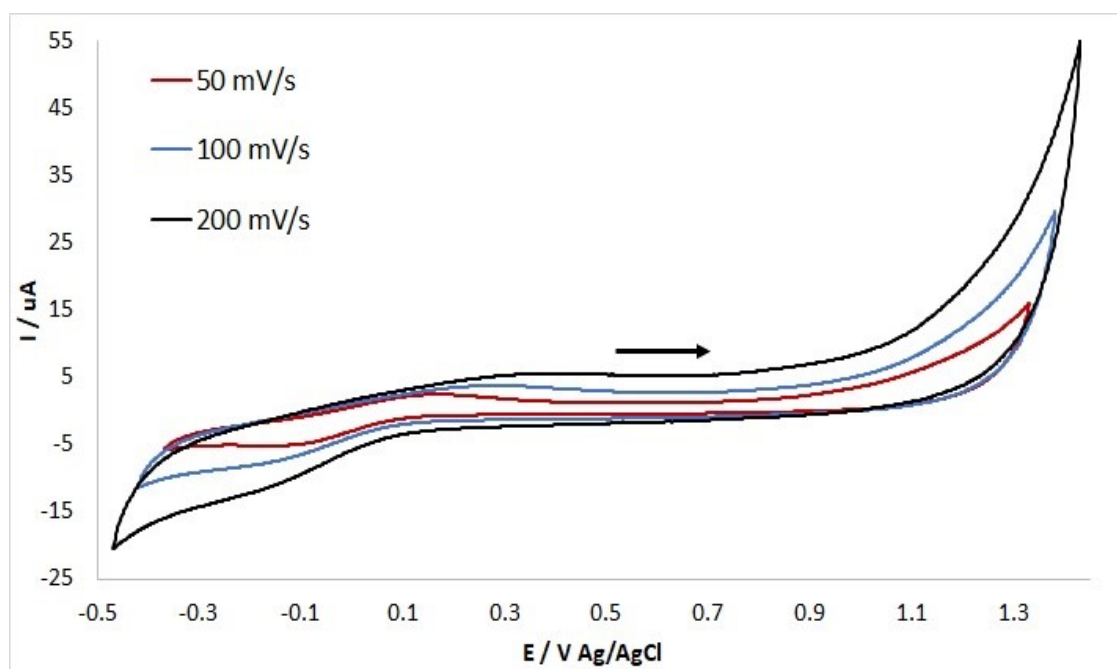


Figure S8.2a. Cyclic voltammogram of complex **Cu-AA2** (0.5 mM) with $\text{KNO}_3/\text{HNO}_3$ as electrolyte solution (96/4 mM) at pH 7.4. The arrow indicates the starting point and direction of the potential scanning (anodic direction).

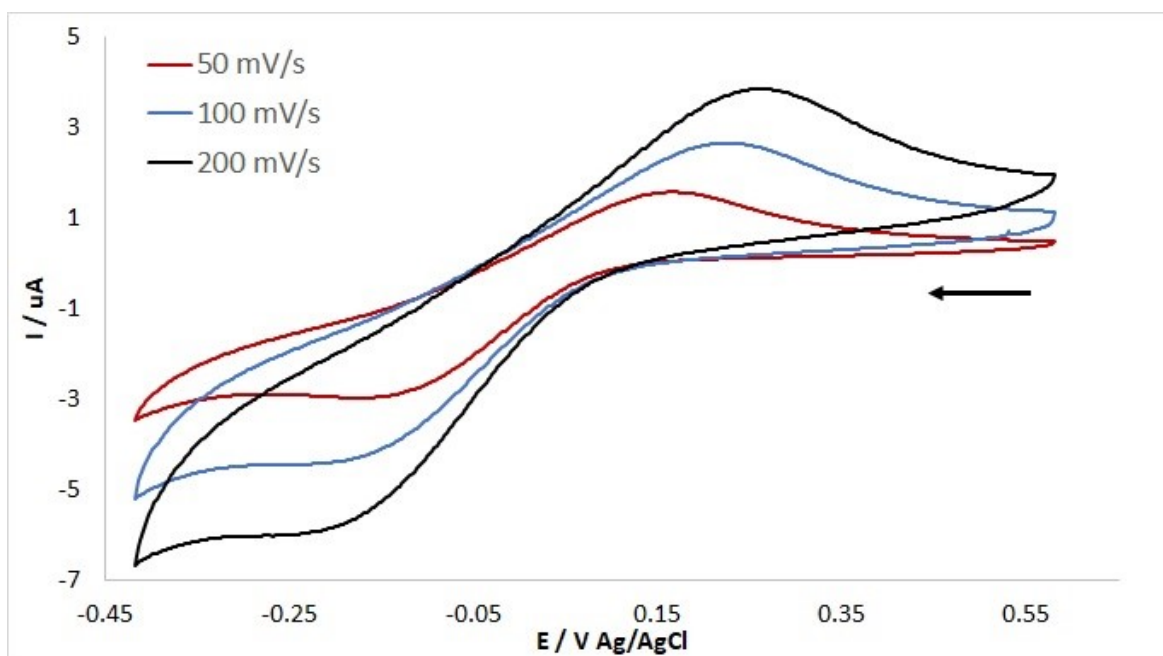


Figure S8.2b. Cyclic voltammogram of complex **Cu-AA2** (0.5 mM) with $\text{KNO}_3/\text{HNO}_3$ as electrolyte solution (96/4 mM) at pH 7.4. The arrow indicates the starting point and direction of the potential scanning (cathodic direction).

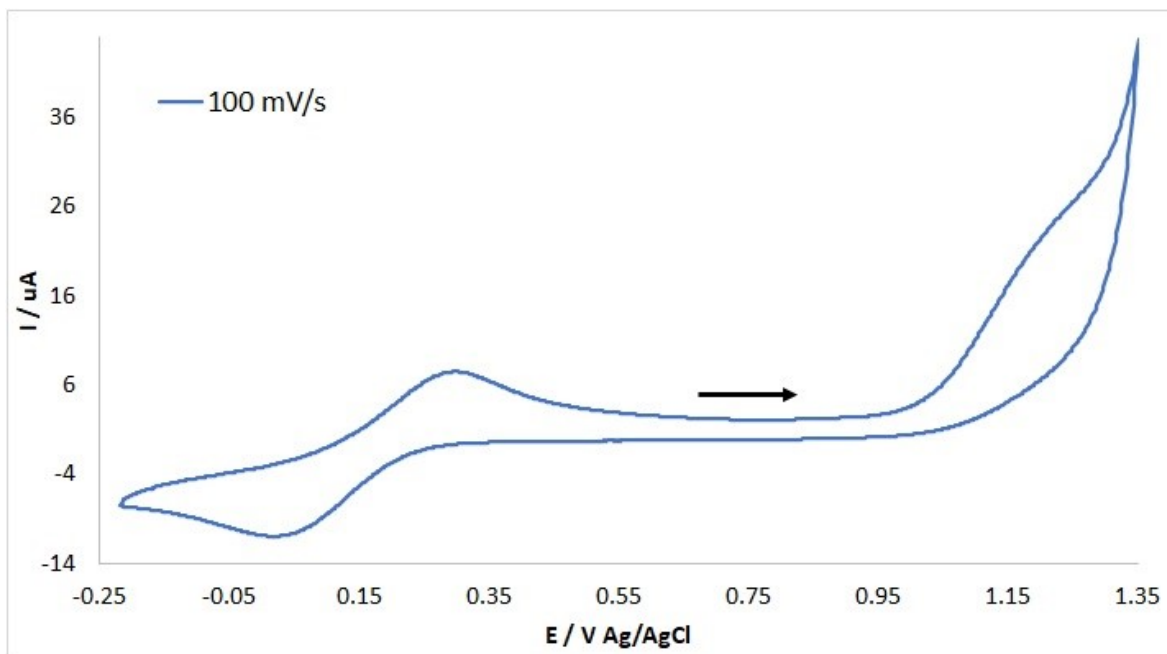


Figure S8.2c. Cyclic voltammogram of complex **Cu-AA2** (0.5 mM) with KCl as electrolyte solution (100 mM) in the presence of MOPS (pH 7.4, 5-fold excess). The arrow indicates the starting point and direction of the potential scanning (anodic direction).

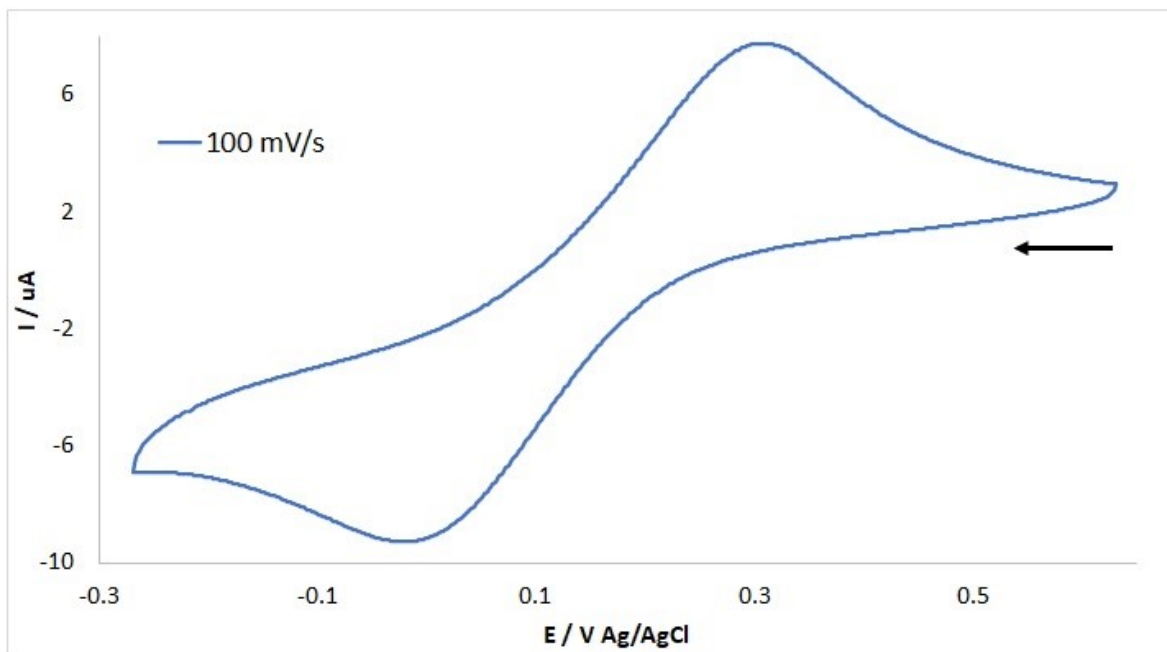


Figure S8.2d. Cyclic voltammogram of complex **Cu-AA2** (0.5 mM) with KCl as electrolyte solution (100 mM) in the presence of MOPS (pH 7.4, 5-fold excess). The arrow indicates the starting point and direction of the potential scanning (cathodic direction).

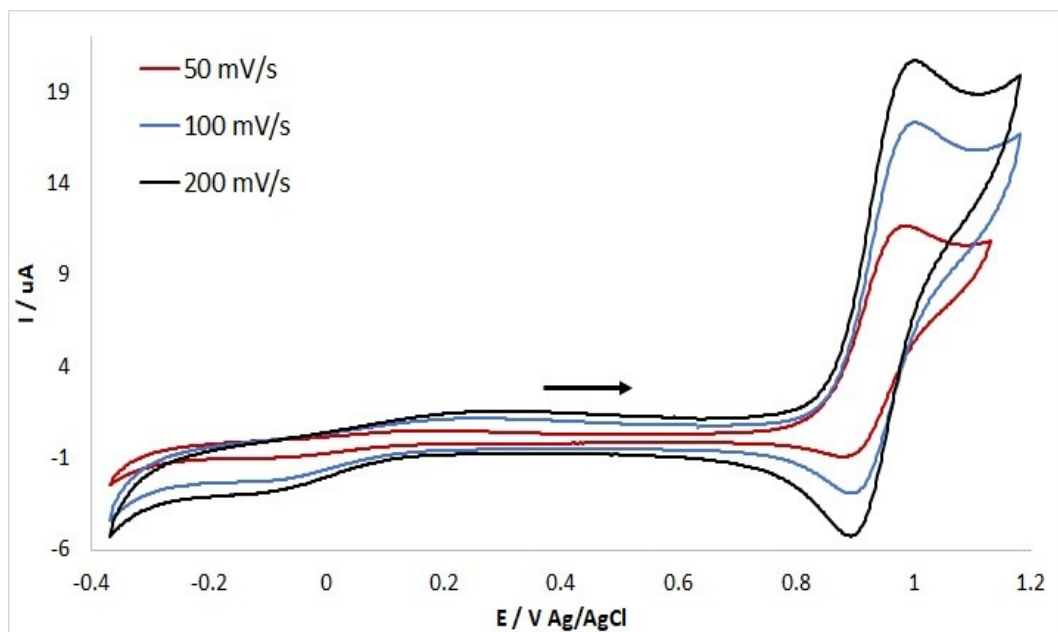


Figure S8.3a. Cyclic voltammogram of complex **Cu-AA3** (0.5 mM) with $\text{KNO}_3/\text{HNO}_3$ as electrolyte solution (96/4 mM) at pH 7.4. The arrow indicates the starting point and direction of the potential scanning (anodic direction).

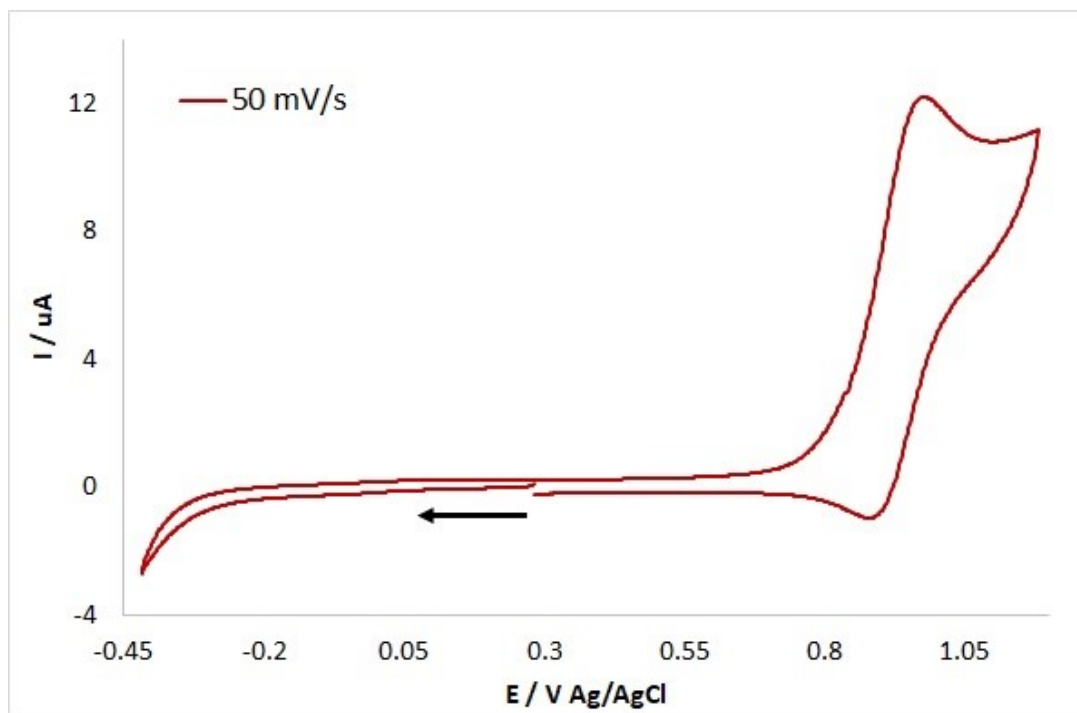


Figure S8.3b. Cyclic voltammogram of complex **Cu-AA3** (0.5 mM) with $\text{KNO}_3/\text{HNO}_3$ as electrolyte solution (96/4 mM) at pH 7.4. The arrow indicates the starting point and direction of the potential scanning (cathodic direction).

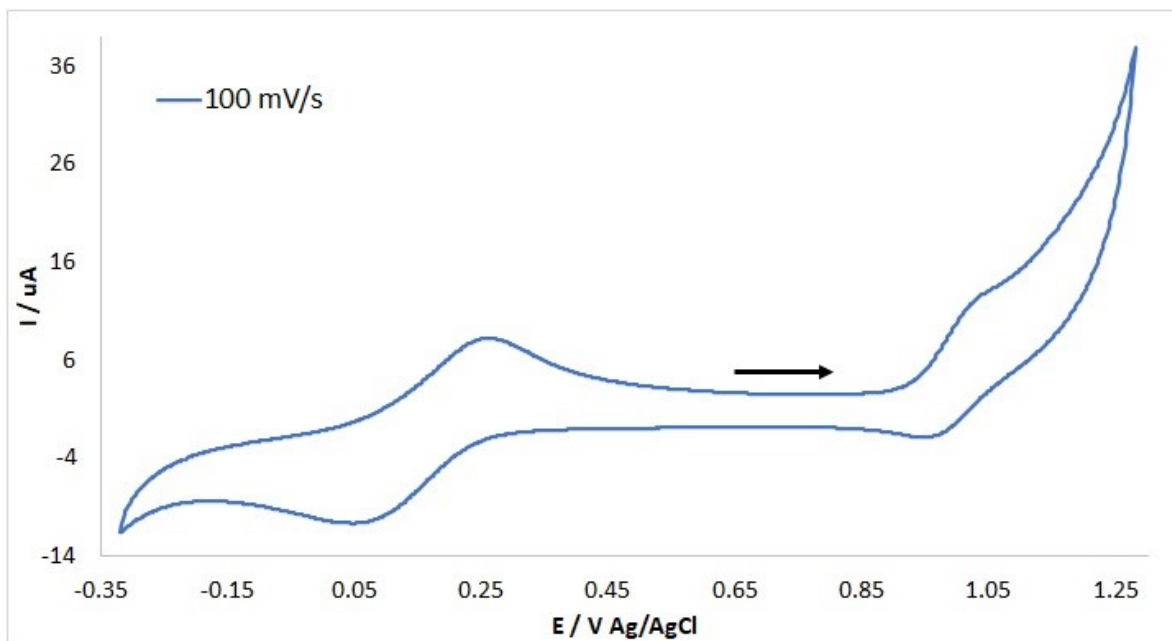


Figure S8.3c. Cyclic voltammogram of complex **Cu-AA3** (0.5 mM) with KCl as electrolyte solution (100 mM) in the presence of MOPS (pH 7.4, 5-fold excess). The arrow indicates the starting point and direction of the potential scanning (anodic direction).

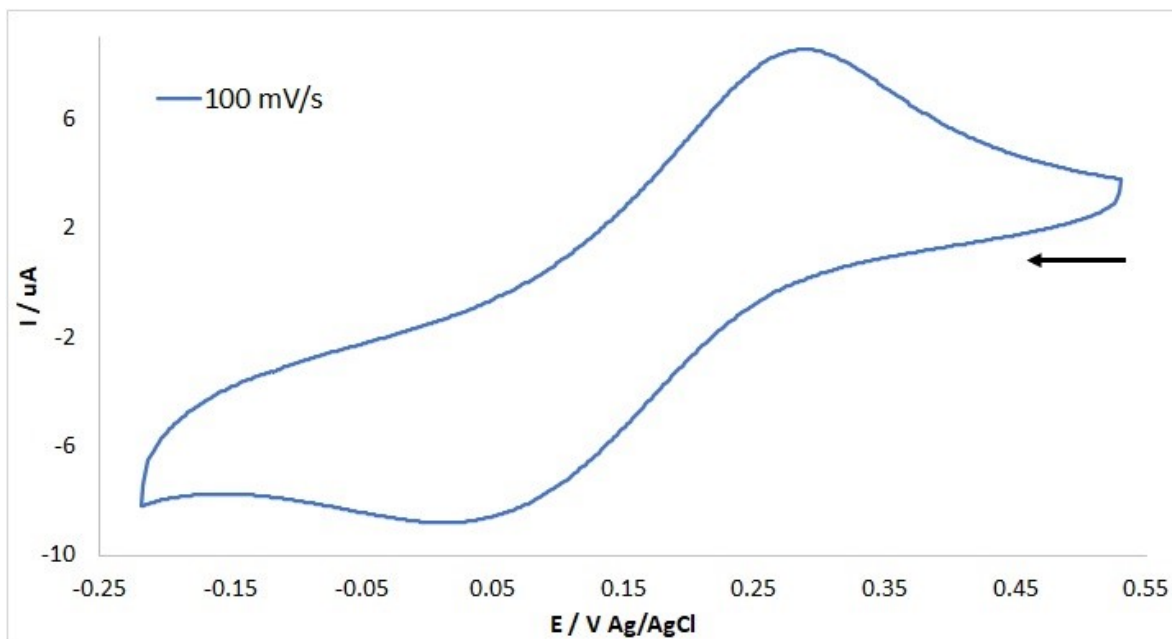


Figure S8.3d. Cyclic voltammogram of complex **Cu-AA3** (0.5 mM) with KCl as electrolyte solution (100 mM) in the presence of MOPS (pH 7.4, 5-fold excess). The arrow indicates the starting point and direction of the potential scanning (cathodic direction).

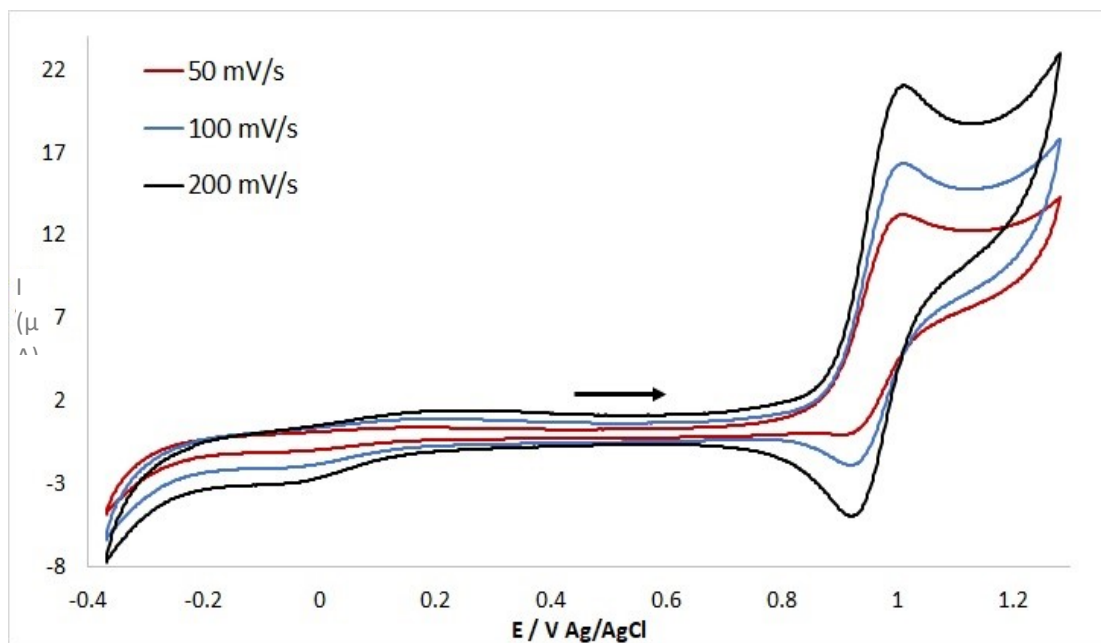


Figure S8.4a. Cyclic voltammogram of complex **Cu-AA4** (0.5 mM) with $\text{KNO}_3/\text{HNO}_3$ as electrolyte solution (96/4 mM) at pH 7.4. The arrow indicates the starting point and direction of the potential scanning (anodic direction).

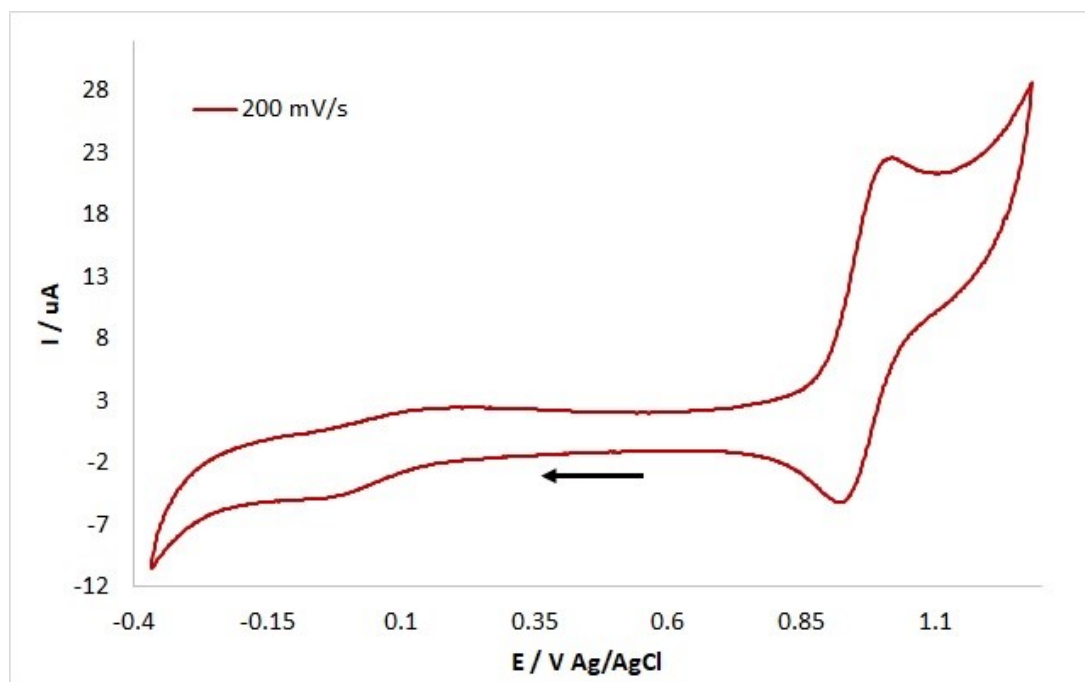


Figure S8.4b. Cyclic voltammogram of complex **Cu-AA4** (0.5 mM) with $\text{KNO}_3/\text{HNO}_3$ as electrolyte solution (96/4 mM) at pH 7.4. The arrow indicates the starting point and direction of the potential scanning (cathodic direction).

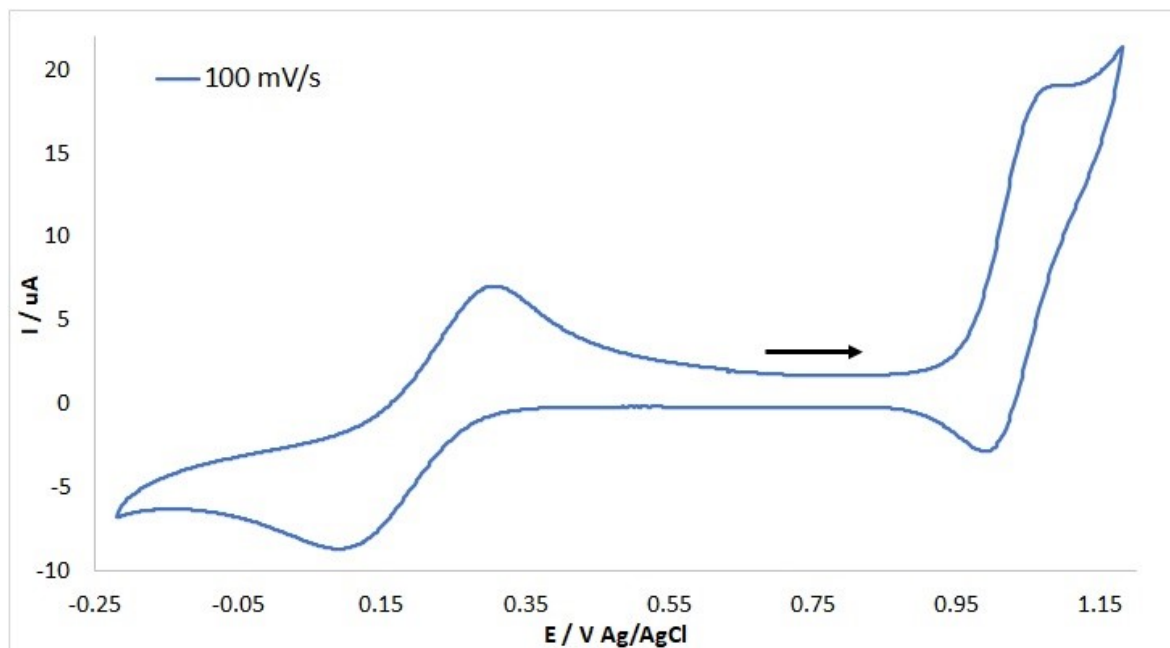


Figure S8.4c. Cyclic voltammogram of complex **Cu-AA4** (0.5 mM) with KCl as electrolyte solution (100 mM) in the presence of MOPS (pH 7.4, 5-fold excess). The arrow indicates the starting point and direction of the potential scanning (anodic direction).

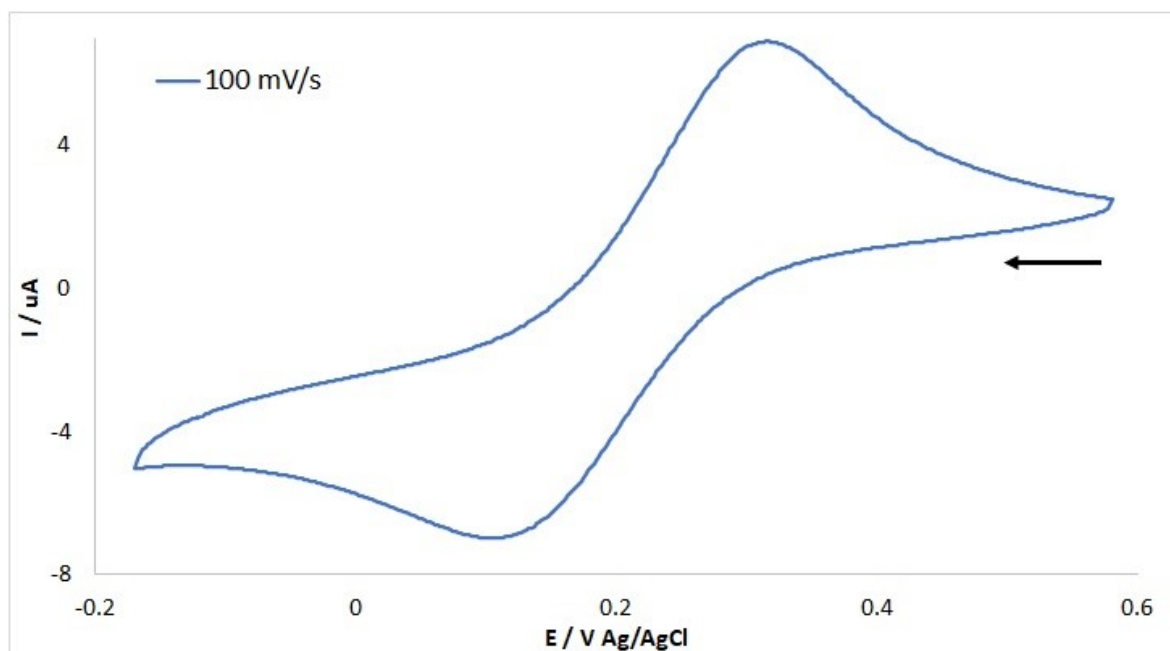


Figure S8.4d. Cyclic voltammogram of complex **Cu-AA4** (0.5 mM) with KCl as electrolyte solution (100 mM) in the presence of MOPS (pH 7.4, 5-fold excess). The arrow indicates the starting point and direction of the potential scanning (cathodic direction).

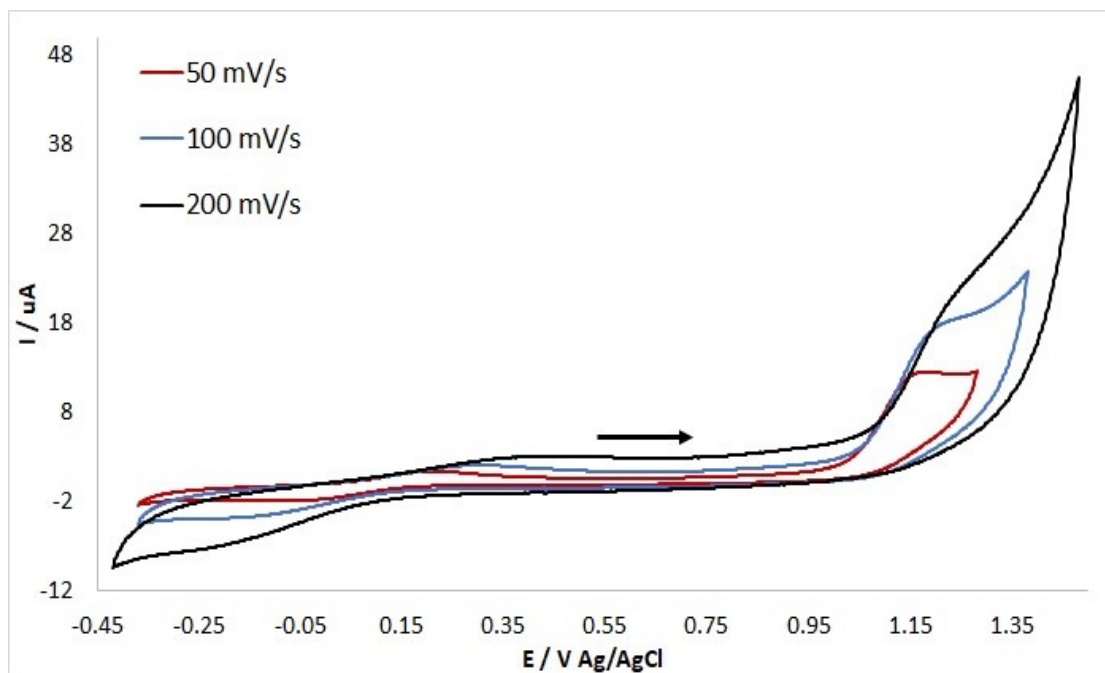


Figure S8.5a. Cyclic voltammogram of complex **Cu-CA1** (0.5 mM) with KNO₃/HNO₃ as electrolyte solution (96/4 mM) at pH 7.4. The arrow indicates the starting point and direction of the potential scanning (anodic direction).

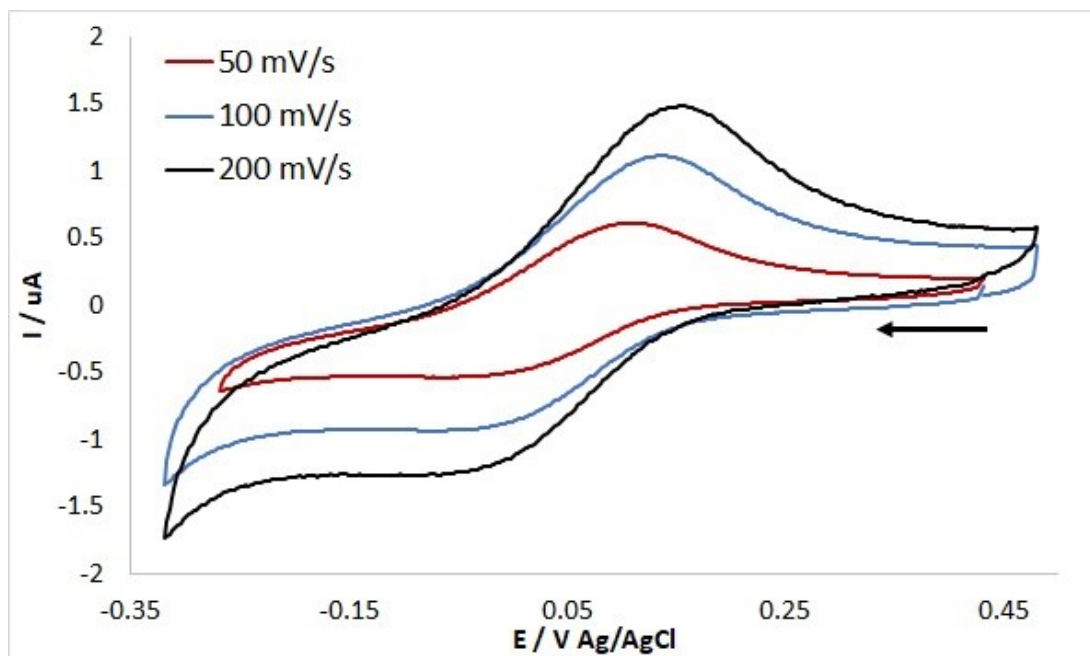


Figure S8.5b. Cyclic voltammogram of complex **Cu-CA1** (0.5 mM) with KNO₃/HNO₃ as electrolyte solution (96/4 mM) at pH 7.4. The arrow indicates the starting point and direction of the potential scanning (cathodic direction).

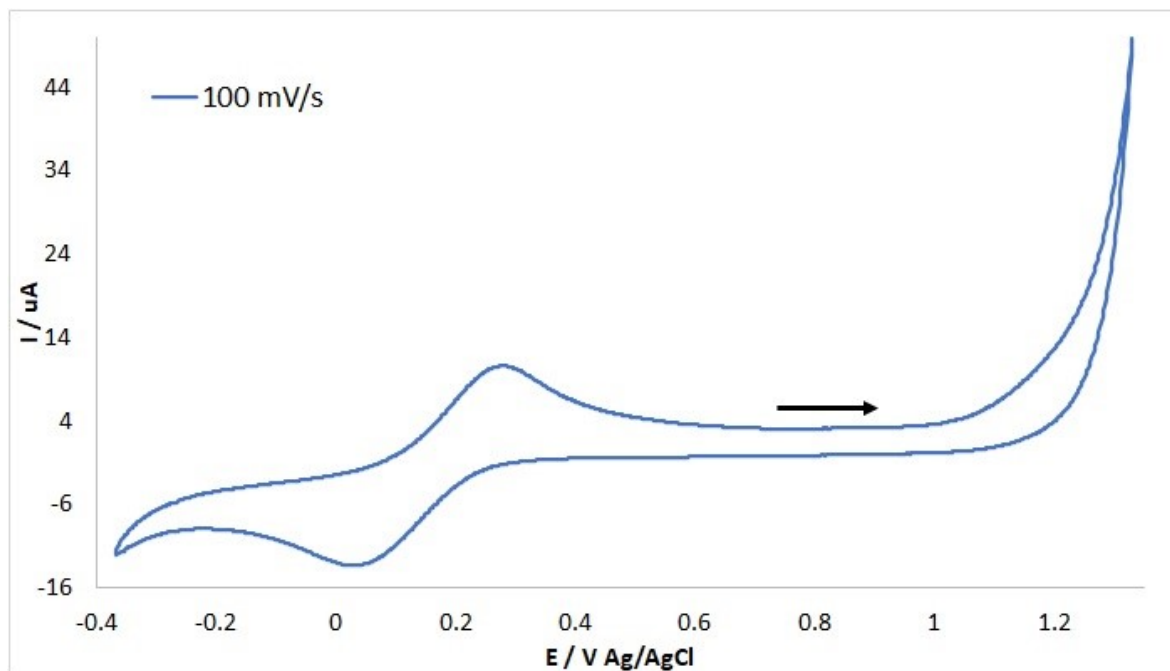


Figure S8.5c. Cyclic voltammogram of complex **Cu-CA1** (0.5 mM) with KCl as electrolyte solution (100 mM) in the presence of MOPS (pH 7.4, 5-fold excess). The arrow indicates the starting point and direction of the potential scanning (anodic direction).

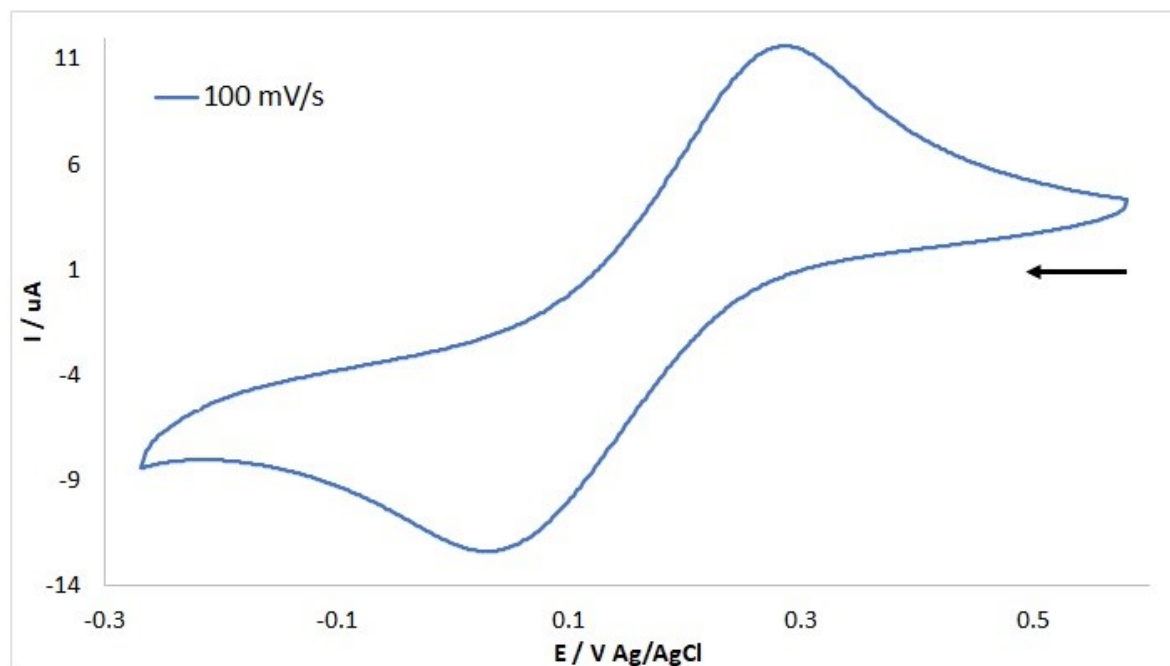


Figure S8.5d. Cyclic voltammogram of complex **Cu-CA1** (0.5 mM) with KCl as electrolyte solution (100 mM) in the presence of MOPS (pH 7.4, 5-fold excess). The arrow indicates the starting point and direction of the potential scanning (cathodic direction).

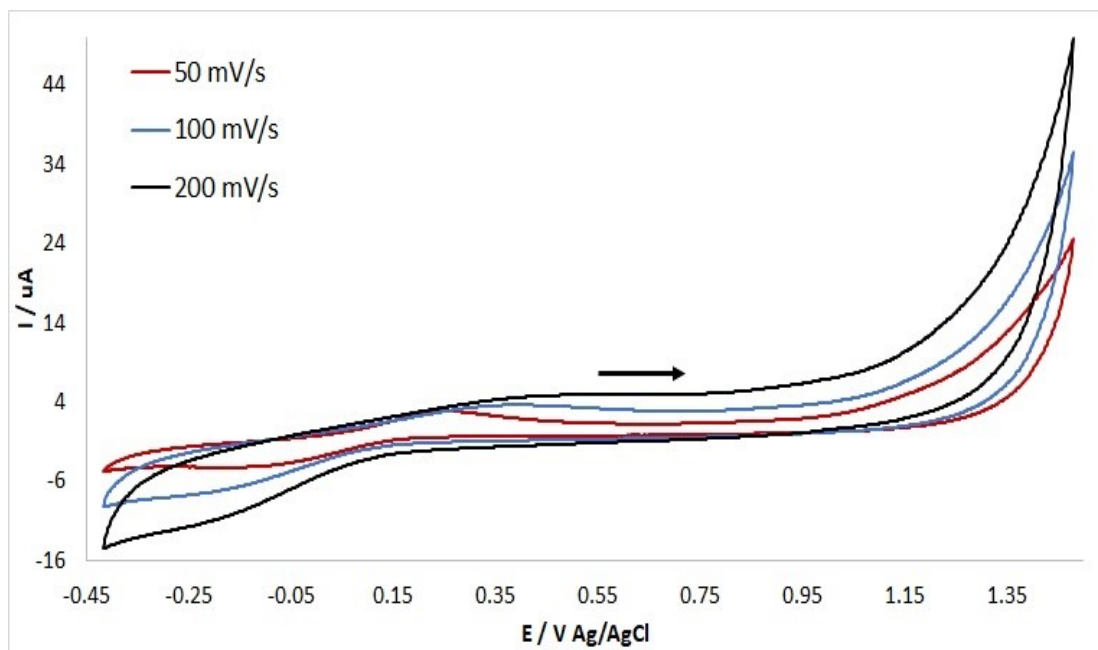


Figure S8.6a. Cyclic voltammogram of complex **Cu-CA2** (0.5 mM) with $\text{KNO}_3/\text{HNO}_3$ as electrolyte solution (96/4 mM) at pH 7.4. The arrow indicates the starting point and direction of the potential scanning (anodic direction).

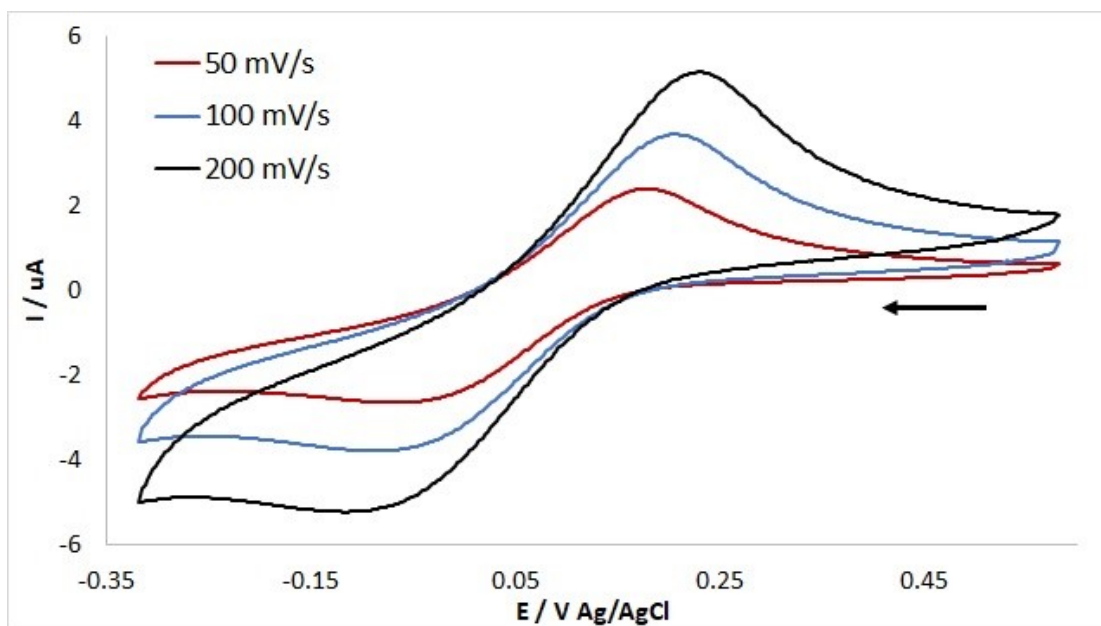


Figure S8.6b. Cyclic voltammogram of complex **Cu-CA2** (0.5 mM) with $\text{KNO}_3/\text{HNO}_3$ as electrolyte solution (96/4 mM) at pH 7.4. The arrow indicates the starting point and direction of the potential scanning (cathodic direction).

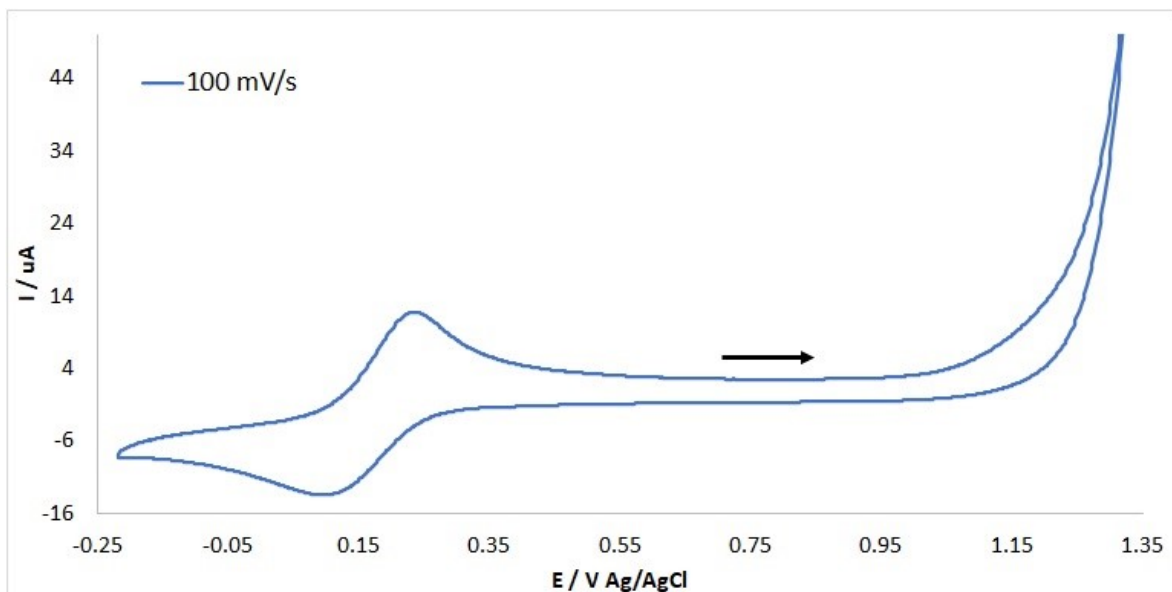


Figure S8.6c. Cyclic voltammogram of complex **Cu-CA2** (0.5 mM) with KCl as electrolyte solution (100 mM) in the presence of MOPS (pH 7.4, 5-fold excess). The arrow indicates the starting point and direction of the potential scanning (anodic direction).

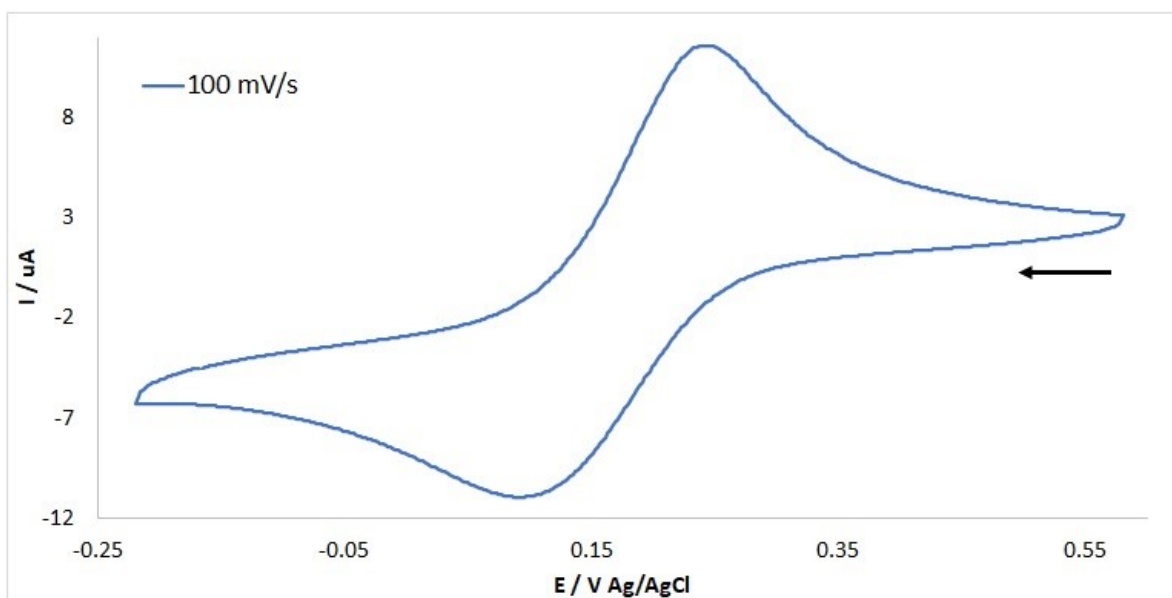


Figure S8.6d. Cyclic voltammogram of complex **Cu-CA2** (0.5 mM) with KCl as electrolyte solution (100 mM) in the presence of MOPS (pH 7.4, 5-fold excess). The arrow indicates the starting point and direction of the potential scanning (cathodic direction).

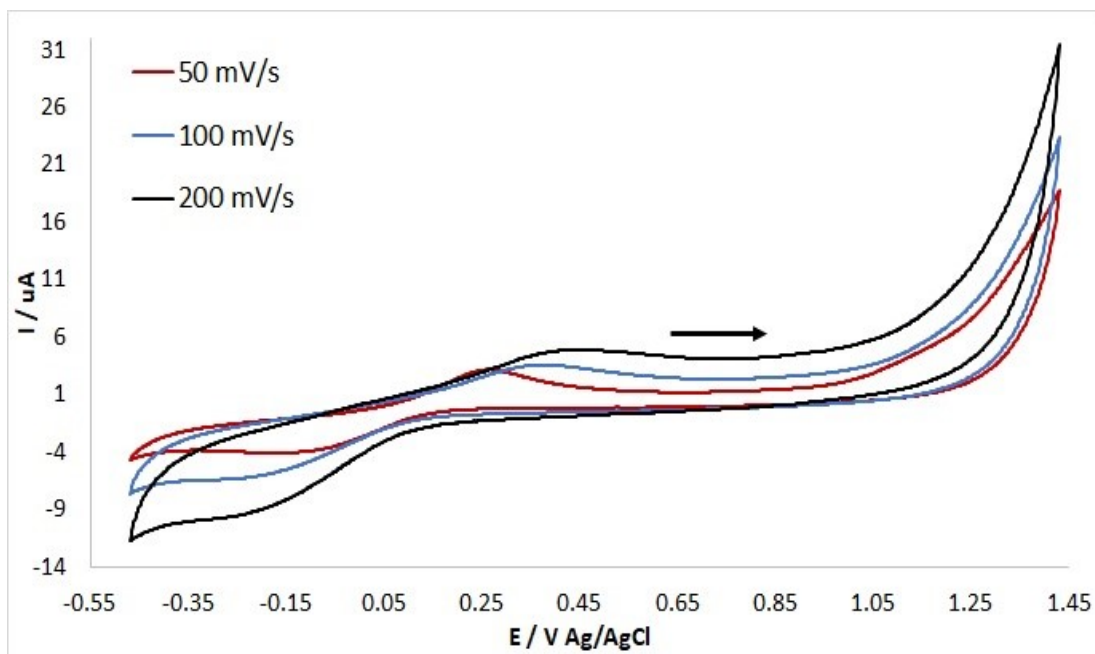


Figure S8.7a. Cyclic voltammogram of complex **Cu-CA3** (0.5 mM) with $\text{KNO}_3/\text{HNO}_3$ as electrolyte solution (96/4 mM) at pH 7.4. The arrow indicates the starting point and direction of the potential scanning (anodic direction).

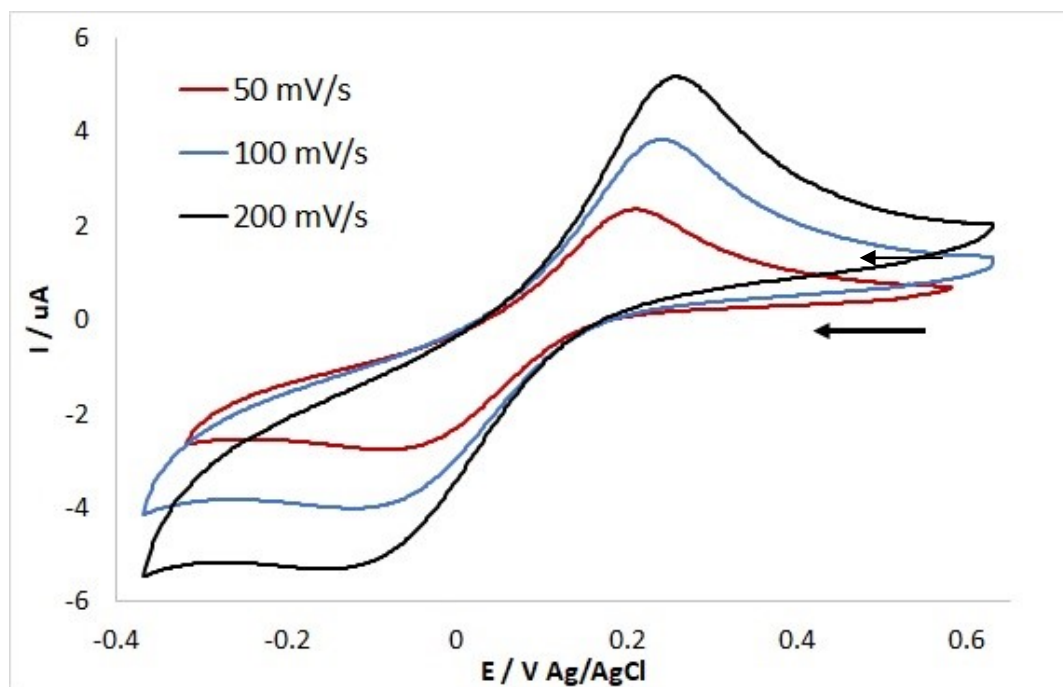


Figure S8.7b. Cyclic voltammogram of complex **Cu-CA3** (0.5 mM) with $\text{KNO}_3/\text{HNO}_3$ as electrolyte solution (96/4 mM) at pH 7.4. The arrow indicates the starting point and direction of the potential scanning (cathodic direction).

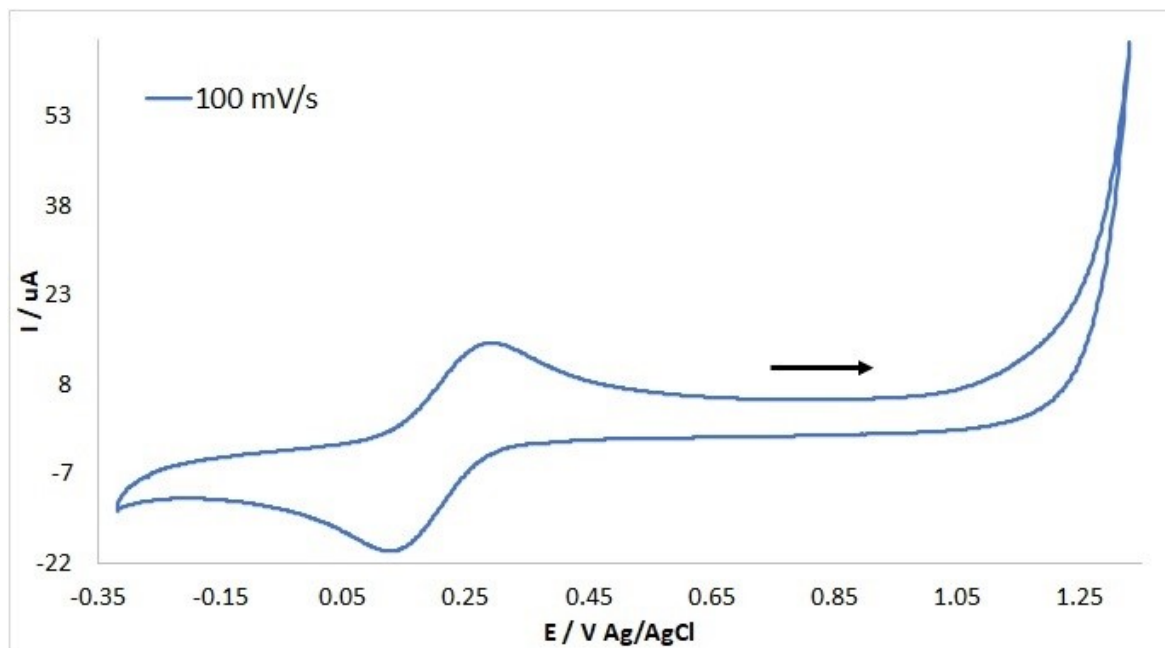


Figure S8.7c. Cyclic voltammogram of complex **Cu-CA3** (0.5 mM) with KCl as electrolyte solution (100 mM) in the presence of MOPS (pH 7.4, 5-fold excess). The arrow indicates the starting point and direction of the potential scanning (anodic direction).

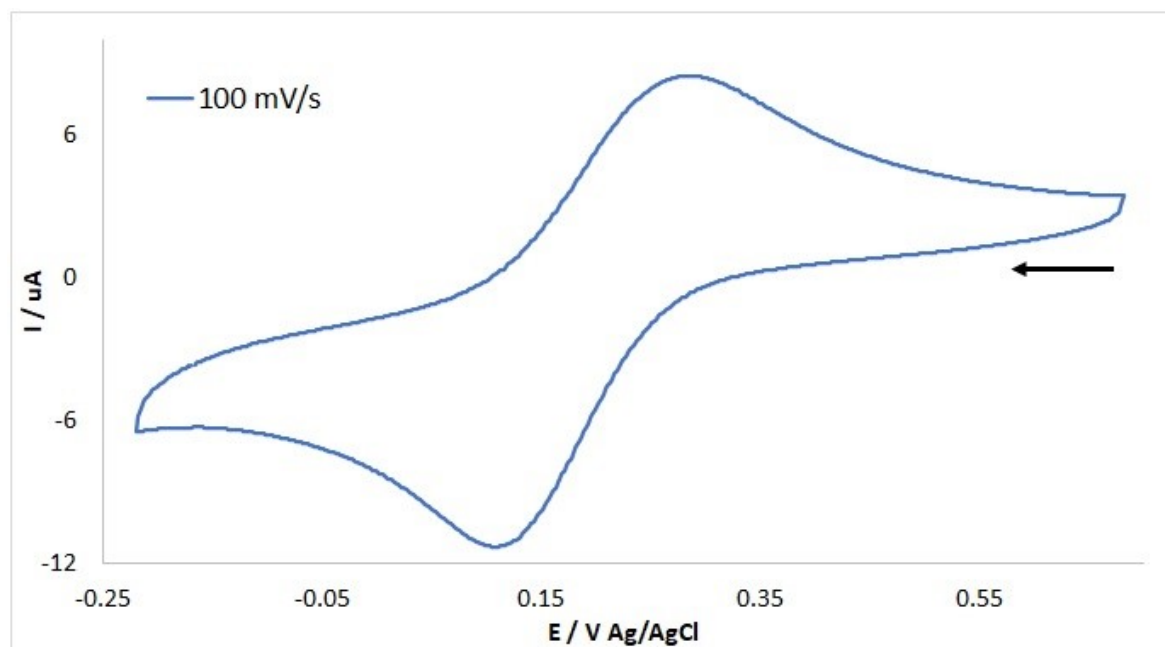


Figure S8.7d. Cyclic voltammogram of complex **Cu-CA3** (0.5 mM) with KCl as electrolyte solution (100 mM) in the presence of MOPS (pH 7.4, 5-fold excess). The arrow indicates the starting point and direction of the potential scanning (cathodic direction).

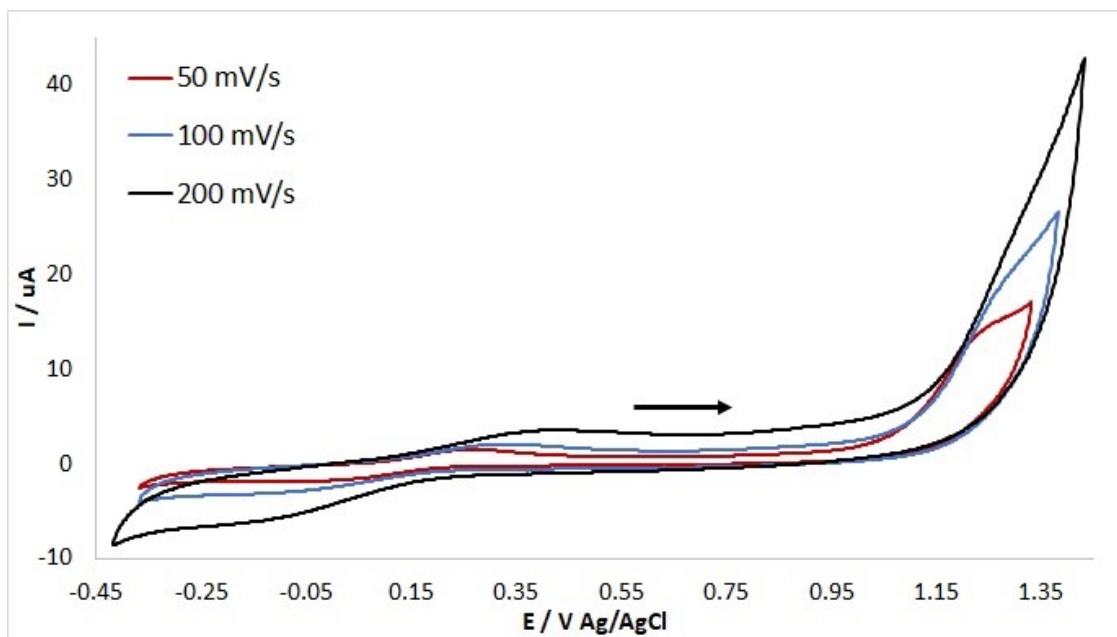


Figure S8.8a. Cyclic voltammogram of complex **Cu-CA4** (0.5 mM) with KNO₃/HNO₃ as electrolyte solution (96/4 mM) at pH 7.4. The arrow indicates the starting point and direction of the potential scanning (anodic direction).

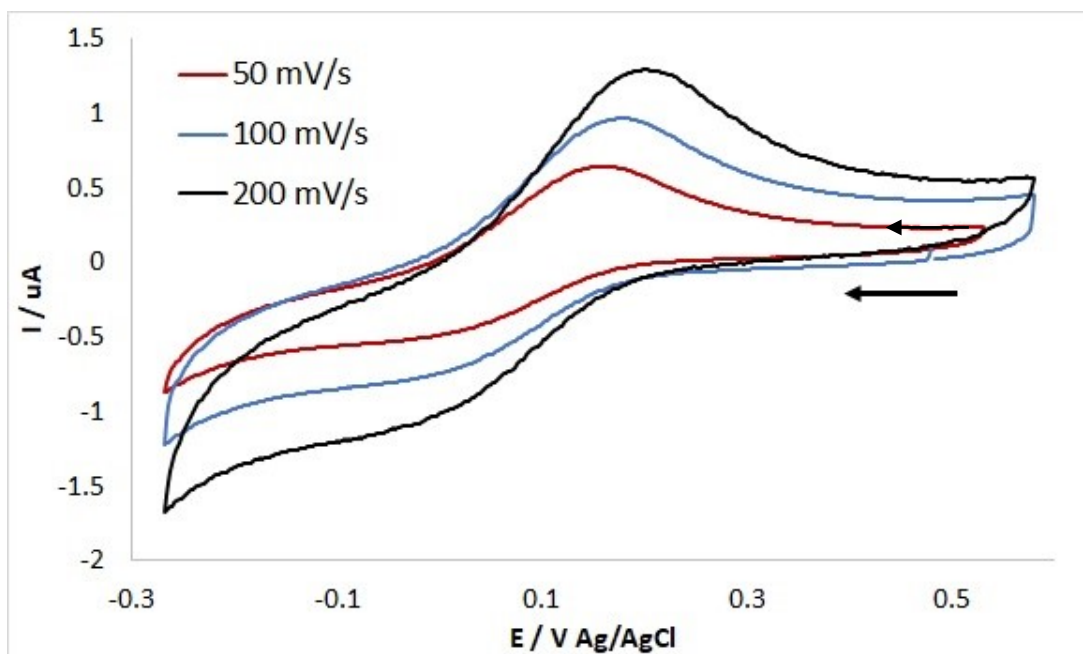


Figure S8.8b. Cyclic voltammogram of complex **Cu-CA4** (0.5 mM) with KNO₃/HNO₃ as electrolyte solution (96/4 mM) at pH 7.4. The arrow indicates the starting point and direction of the potential scanning (cathodic direction).

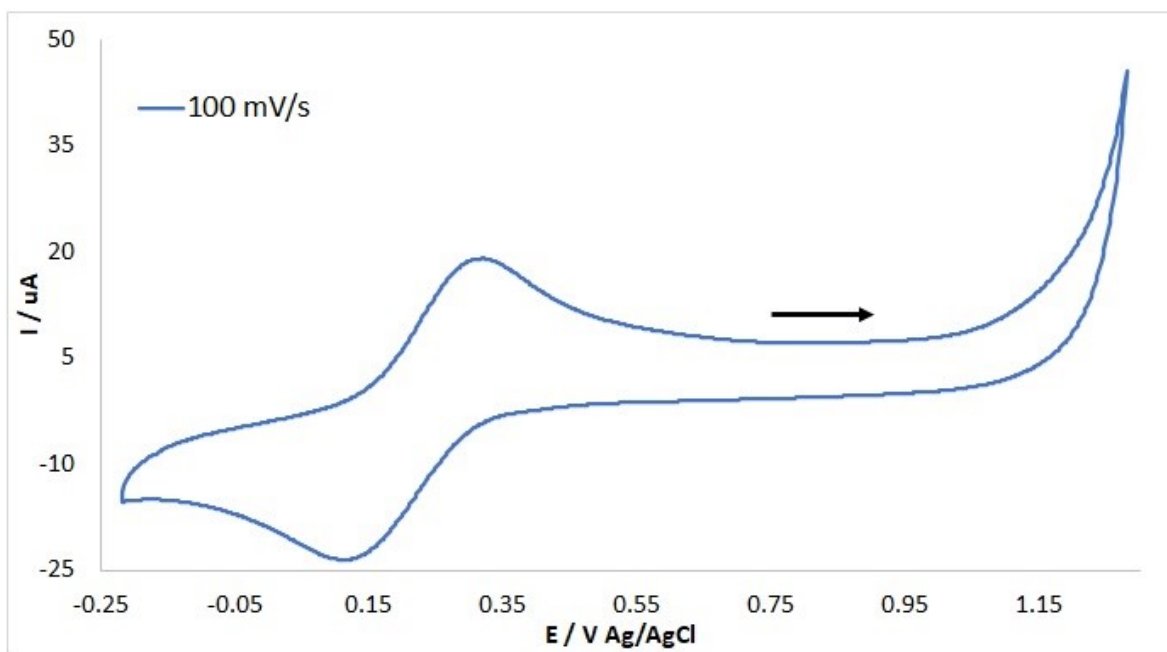


Figure S8.8c. Cyclic voltammogram of complex **Cu-CA4** (0.5 mM) with KCl as electrolyte solution (100 mM) in the presence of MOPS (pH 7.4, 5-fold excess). The arrow indicates the starting point and direction of the potential scanning (anodic direction).

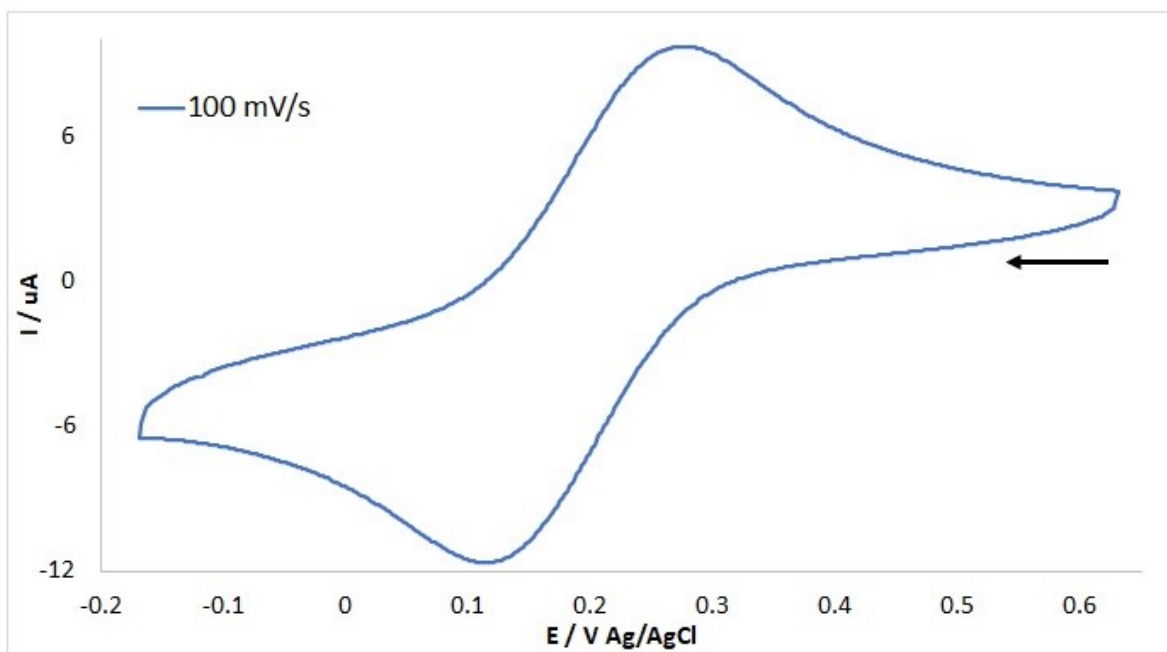


Figure S8.8d. Cyclic voltammogram of complex **Cu-CA4** (0.5 mM) with KCl as electrolyte solution (100 mM) in the presence of MOPS (pH 7.4, 5-fold excess). The arrow indicates the starting point and direction of the potential scanning (cathodic direction).

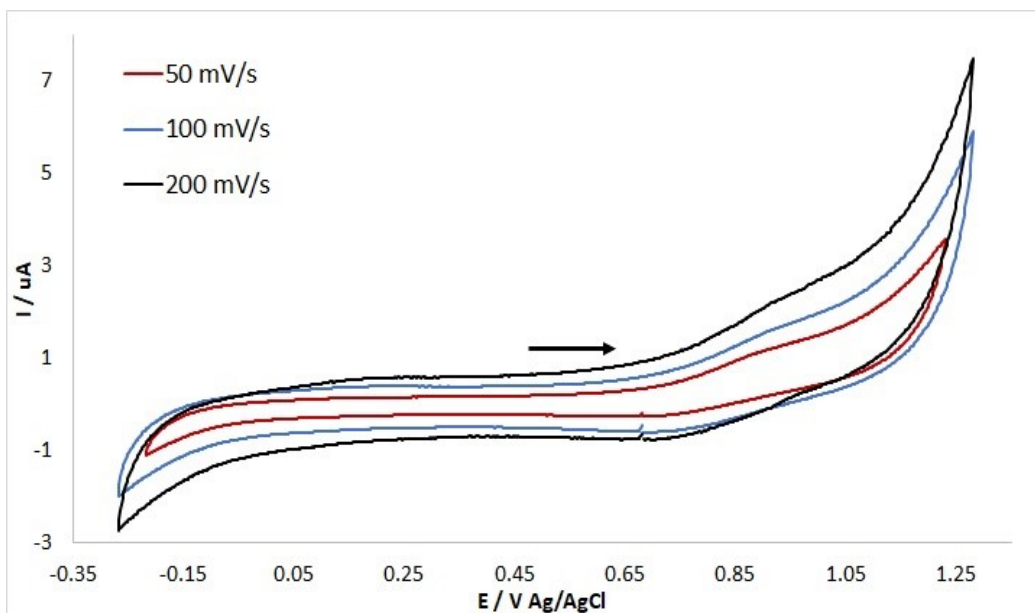


Figure S8.9a. Cyclic voltammogram of complex **Cu-CA5** (0.5 mM) with $\text{KNO}_3/\text{HNO}_3$ as electrolyte solution (96/4 mM) at pH 7.4. The arrow indicates the starting point and direction of the potential scanning (anodic direction).

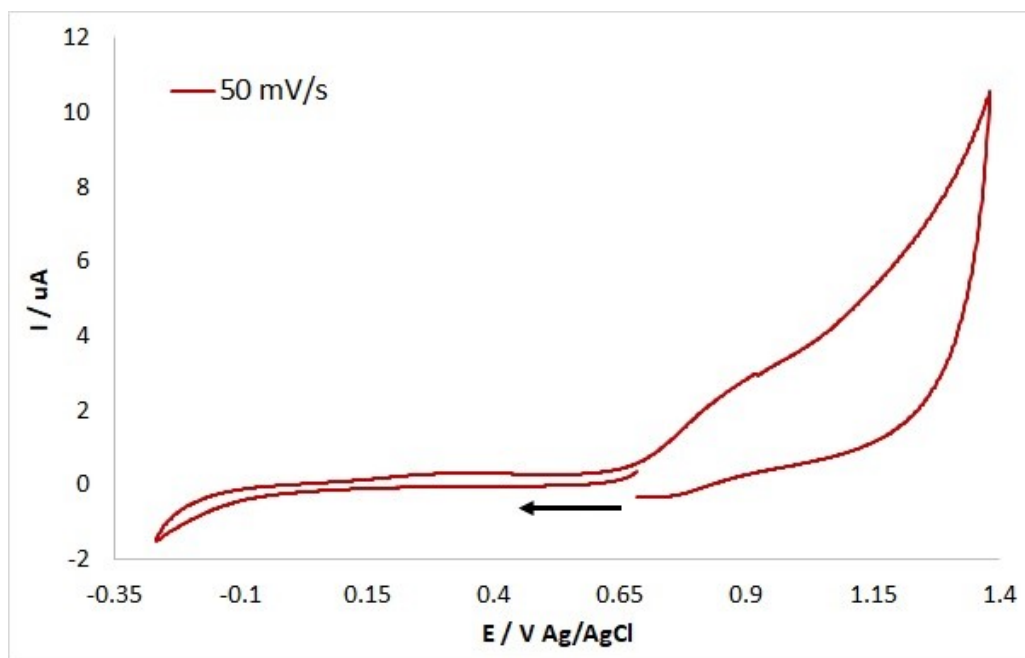


Figure S8.9b. Cyclic voltammogram of complex **Cu-CA5** (0.5 mM) with $\text{KNO}_3/\text{HNO}_3$ as electrolyte solution (96/4 mM) at pH 7.4. The arrow indicates the starting point and direction of the potential scanning (cathodic direction).

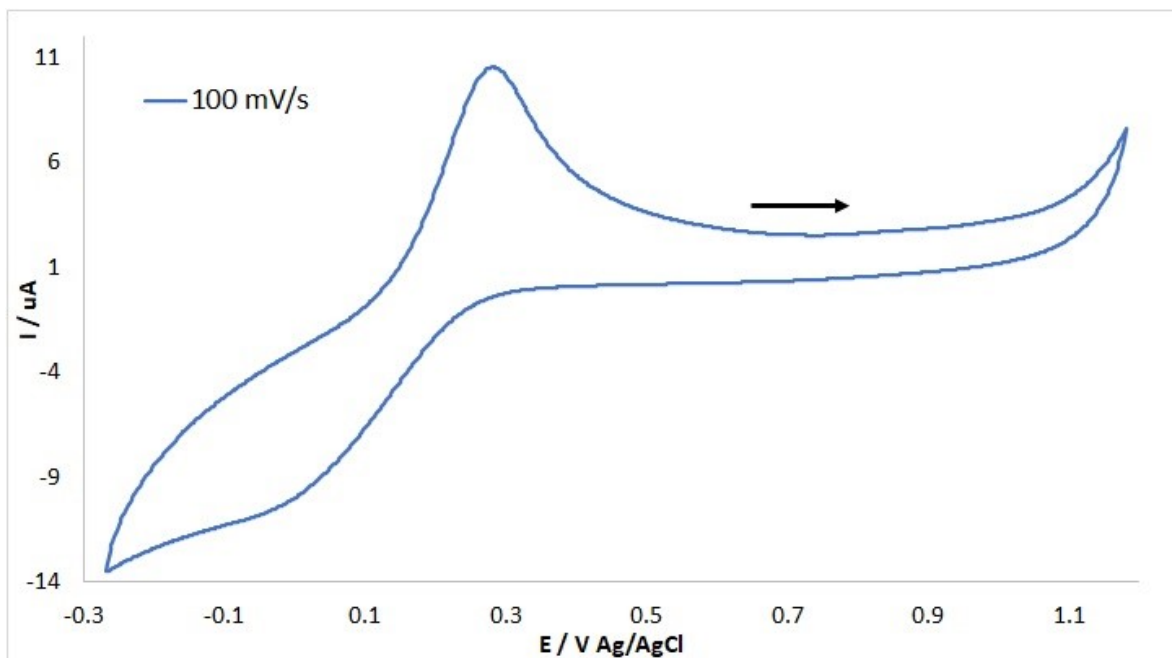


Figure S8.9c. Cyclic voltammogram of complex **Cu-CA5** (0.5 mM) with KCl as electrolyte solution (100 mM) in the presence of MOPS (pH 7.4, 5-fold excess). The arrow indicates the starting point and direction of the potential scanning (anodic direction).

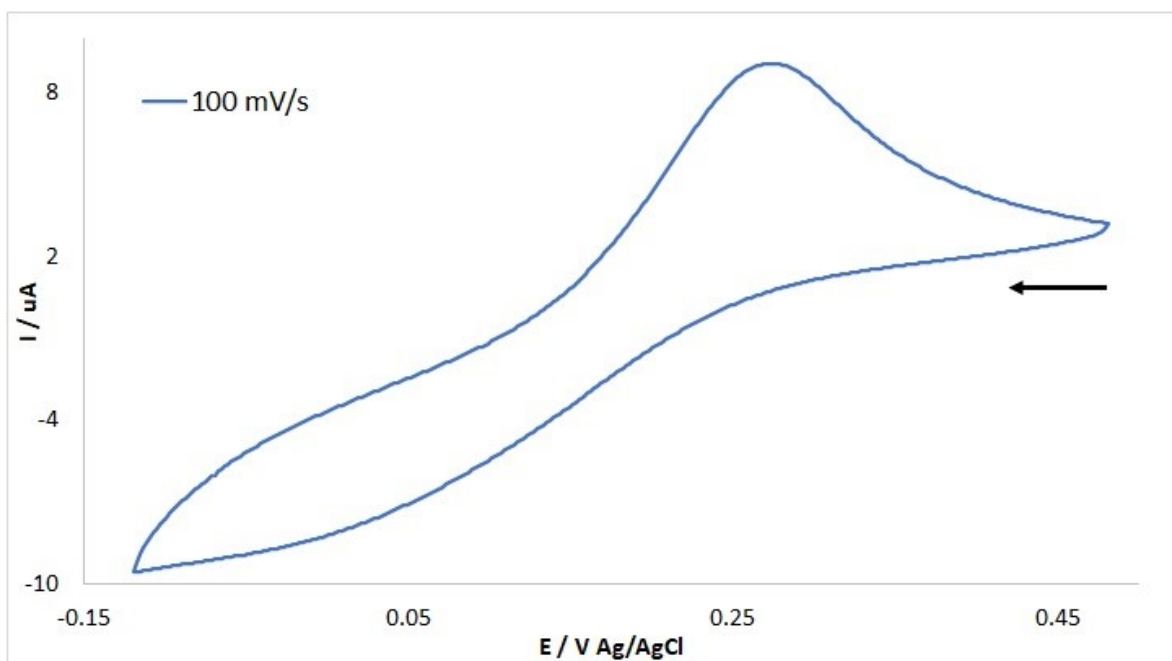


Figure S8.9d. Cyclic voltammogram of complex **Cu-CA5** (0.5 mM) with KCl as electrolyte solution (100 mM) in the presence of MOPS (pH 7.4, 5-fold excess). The arrow indicates the starting point and direction of the potential scanning (cathodic direction).

S9 Computational details and data

Starting structures were minimized with xTB-GFN2¹³ in a GBSA solvation model. Those were used as initial structures for an exhaustive CREST (Conformer Rotamer Ensemble Research Tool)¹⁴ exploration of the molecular chemical space with the same Hamiltonian, solvent model and the composite 'entropy' scheme search criteria for conformers and rotamers.¹⁵ The finally obtained unique entries in the CRE (Conformer Rotamer Ensemble) were subsequently re-optimized with tighter convergence criteria. After calculating second derivative Hessian matrices for all unique entries, those were sorted according to their relative Gibbs free energies. The lowest Gibbs free energy conformer was then used in Density Functional Theory (DFT) calculations with the BP86^{16,17} exchange-correlation functional, a def2-TZVP basis set^{18, 19} and a COSMO solvation model²⁰ with Turbomole 7.5. Thermodynamic corrections were calculated in the absence of solvent. Orca 4.0.1 local coupled-cluster DLPNO calculations²¹ with the same basis set in a CPCM solvent with the same basis set and 'TightPNO' settings were performed at the BP86/def2TZVP(COSMO) structures.²²

Table S9.1. Number of unique entries in CRE at different stages of refinement using CREST xTB-GFN2 (entropy/re-optimized/Hessian).

Complex	Oxidation State	
	Cu(II)	Cu(I)
AA1	1/1/1	10/10/10
AA2	26/25/24	87/84/84
AA3	10/10/10	31/31/31
AA4	6/6/6	35/35/34
CA1	8/8/8	76/76/76
CA2	9/9/9	4/4/4
CA3	7/7/7	7/7/7
CA4	11/11/10	11/11/11
CA5	9/9/9	50/50/50

Table S9.2. Lowest conformer structures after exhaustive CREST searches, BP86/def2TZVP(COSMO) refinement.


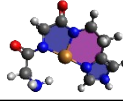
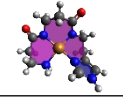
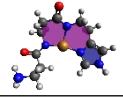
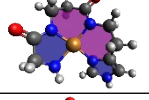
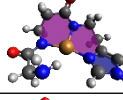
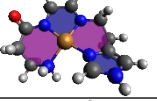
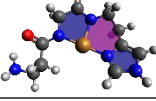
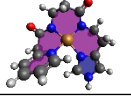
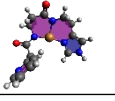
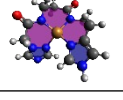
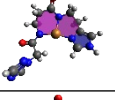
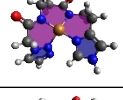
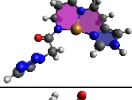
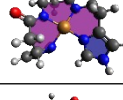
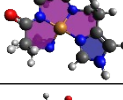
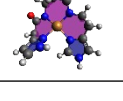
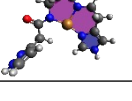
Ligand	ATCUN complexes	
	Cu(II)	Cu(I)
AA1		
AA2		
AA3		
AA4		
CA1		
CA2		
CA3		
CA4		
CA5		

Table S9.3. Calculated coupled-cluster Cu(II) complexation energies and calculated reduction potentials for Cu(II)/Cu(I) reduction relative to Fc⁺/Fc.

	Cu(II) complexation energy [kJ/mol]	Cu(II)/Cu(I) reduction potential [V] vs. Fc ⁺ /Fc		Cu(II)/Cu(I) reduction potential [V] vs. Ag/AgCl
		DFT	CC	Experimental values as determined from Figures S8.1b–S8.9b (+0.131 V shift with respect to Ag pseudoreference electrode, <i>cf.</i> S1)
AA1	-865	-1.59	-1.71	-
AA2	-856	-1.17	-1.33	-0.15
AA3	-860	-1.44	-1.54	-0.10
AA4	-865	-1.50	-1.70	-0.03
CA1	-839	-1.12	-1.21	-0.02
CA2	-797	-0.88	-0.97	-0.06
CA3	-793	-0.88	-0.97	-0.08
CA4	-827	-0.96	-1.07	-0.01
CA5	-835	-1.01	-1.14	-

S10 References

1. J. Hunold, J. Eisermann, M. Brehm and D. Hinderberger, *J. Phys. Chem. B*, 2020, **124**, 8601–8609.
2. S. Stoll and A. Schweiger, *J. Magn. Reson.*, 2006, **178**, 42–55.
3. J. Heinrich, K. Bossak-Ahmad, M. Riisom, H. H. Haeri, T. R. Steel, V. Hergl, A. Langhans, C. Schattschneider, J. Barrera, S. M. F. Jamieson, M. Stein, D. Hinderberger, C. G. Hartinger, W. Bal and N. Kulak, *Chem. Eur. J.*, 2021, **27**, 18093–18102.
4. H. L. Kohn, C. Salomé and E. Salomé-Grosjean, US20110021482A1, 2011.
5. A. N. Boa, J. D. Crane, R. M. Kowalczyk and N. H. Sultana, *Eur. J. Inorg. Chem.*, 2005, 872–878.
6. N. N. Smolyar and Y. M. Yutilov, *Russ. J. Org. Chem.*, 2008, **44**, 1205–1210.
7. R. B. Merrifield, *J. Am. Chem. Soc.*, 1963, **85**, 2149–2154.
8. M. Amblard, J.-A. Fehrentz, J. Martinez and G. Subra, *Mol. Biotechnol.*, 2006, **33**, 239–254.
9. A. Trapaidze, C. Hureau, W. Bal, M. Winterhalter and P. Faller, *J. Biol. Inorg. Chem.* 2012, **17**, 37–47.
10. B. Alies, B. Badej, P. Faller and C. Hureau, *Chem. Eur. J.*, 2012, **18**, 1161–1167.
11. R. P. Hertzberg and P. B. Dervan, *Biochem.* 1984, **23**, 3934–3945.
12. M. Z. Wiloch, I. Ufnalska, A. Bonna, W. Bal, W. Wróblewski and U. E. Wawrzyniak, *J. Electrochem. Soc.* 2017, **164**, G77–G81.
13. C. Bannwarth, S. Ehlert and S. Grimme, *J. Chem. Theory Comput.* 2019, **15**, 1652–1671.
14. P. Pracht, F. Bohle and S. Grimme, *Phys. Chem. Chem. Phys.* 2020, **22**, 7169–7192.
15. P. Pracht and S. Grimme, *Chem. Sci.* 2021, **12**, 6551–6568.
16. A. D. Becke, *Phys. Rev. A*, 1988, **38**, 3098–3100.
17. J. P. Perdew, *Phys. Rev. B*, 1986, **33**, 8822–8824.
18. F. Weigend, *Phys. Chem. Chem. Phys.* 2006, **8**, 1057–1065.
19. F. Weigend and R. Ahlrichs, *Phys. Chem. Chem. Phys.*, 2005, **7**, 3297–3305.
20. A. Klamt and G. Schüürmann, *J. Chem. Soc., Perkin Trans. 2*, 1993, 799–805.
21. Y. Guo, C. Riplinger, U. Becker, D. G. Liakos, Y. Minenkov, L. Cavallo and F. Neese, *J. Chem. Phys.* 2018, **148**, 011101.
22. F. Neese, WIREs Computational Molecular Science, 2018, **8**, e1327.